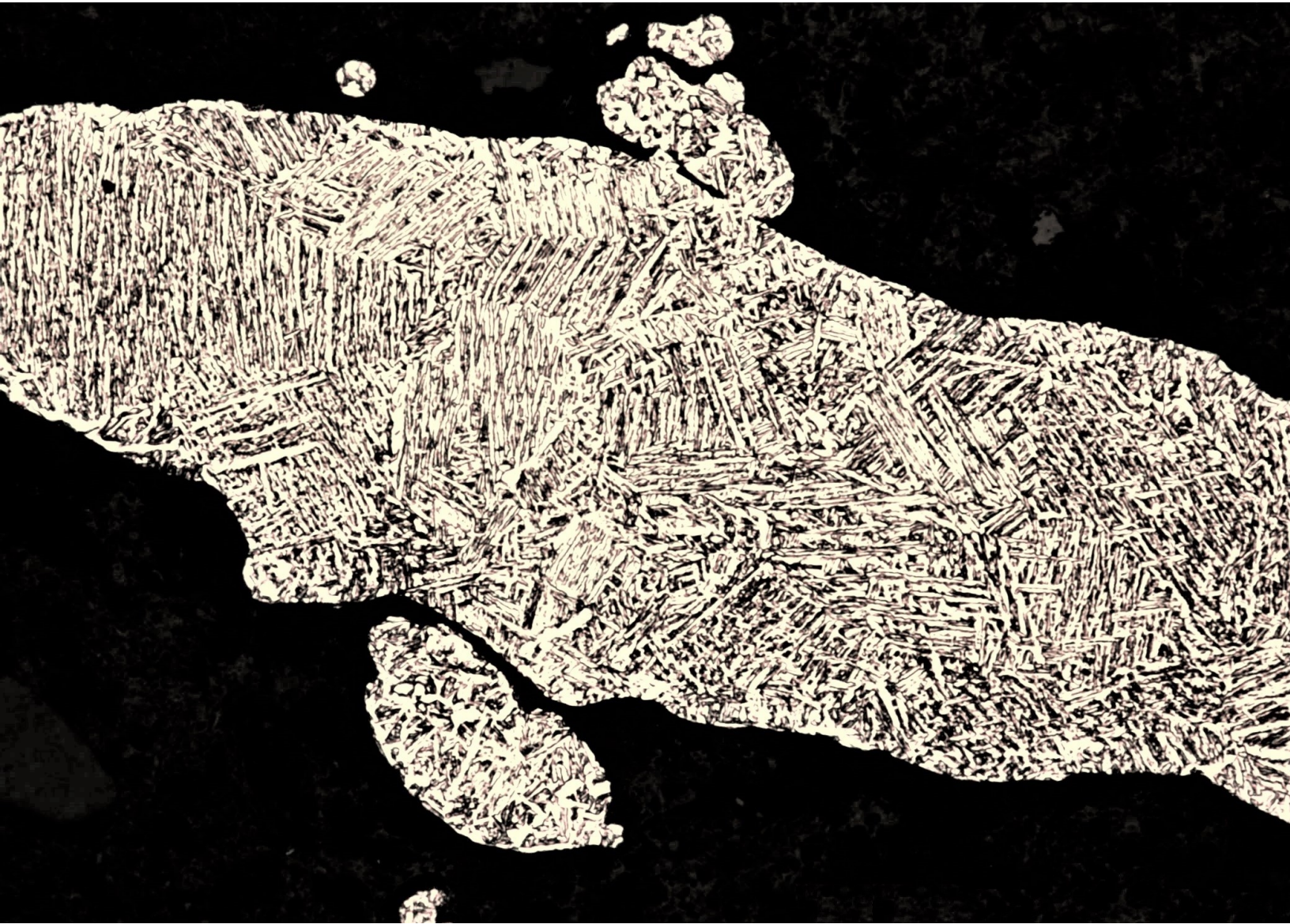


The effect of post process treatments on biomechanical properties of Ti6Al4V metamaterials and spinal cage implants manufactured by selective laser melting

Adriaan Blok



Student number: 4515323
Delft University of Technology
Faculty of Mechanical, Maritime
and Materials Engineering (3ME)

Supervisors:

Dr. V.A. Popovich
Dr. S. M. Ahmadi
Dr. C.D. Rans

Thesis comity:

Dr. J. Zhou
Dr. Y. Gonzalez-Garcia

TU Delft
Amber Implants
TU delft
TU delft
TU delft

Acknowledgements

This thesis would not have been possible without excellent supervision. Therefore I would like to thank Vera Popovich for providing guidance throughout the research as well as essential discussion and knowledge. The weekly meetings helped out immensely in decision making and analysing of results. Furthermore I would like to thank Mohammad Ahmadi for guidance throughout the project and in particular for arranging the Set-up for the ASTM F2077 testing and for providing the continuous SLM samples. I would like to thank Calvin Rans for providing guidance and discussion on the fatigue testing of the spinal cage implants. I want to thank Pim Pellikaan for the weekly discussions at Amber Implants.

During the project I have made use of various labs and equipments. I would not have been able to use these machines without the help of the lab technicians. Therefore I would like to thank Elise Reinton, Ton Riemslog for instructing me on working in the Mechanical behaviour lab and using the compression machine, fatigue machine and the Sand blasting equipment. They provided knowledge on how to operate the equipment as well as provided knowledge on how to accurately perform tests. I'd like to thank Sander van Asperen and Agnieszka Kooijman for instructing me on working in the microscopy lab and the corrosion lab, respectively. Furthermore I would like to thank Gert-jan Mulder and Berthil Grashof on instructing me on working in the Aerospace structures and materials lab. They provided insights regarding safety and knowledge on accuracy of testing.

I want to thank Roumen Petrov for support in EBSD measurements and analysis and I want to thank Sander Leeflang for the manufacturing of pulsed SLM samples.

Finally I want to thank my parents for supporting me and enabling me to do the Materials Science and Engineering master in the first place.

ABSTRACT

Selective laser melting (SLM) is an additive manufacturing technique, which is currently on the rise of being used for manufacturing bone implants. Spinal cage, dental and hip implants can for example be manufactured using SLM. Ti6Al4V lattice structures, categorised as metamaterials, can be printed by SLM with mechanical properties close to bone tissue. Due to the lattice structure the stiffness of the Ti6Al4V is decreased, by which stress shielding can be reduced. The lattice structures enhance bone ingrowth which in turn improves the implant's integration into bone tissue. In light of this potential, this research is focused on biomechanical properties of additively manufactured Ti6Al4V metamaterials.

The current research is aimed at improving the fatigue resistance and wettability of diamond lattice structured Ti6Al4V by applying different microstructural designs and surface engineering through hot isostatic pressing (HIP), sand blasting (SB) and chemical etching (CE). Furthermore a comparison is made between the two SLM processes in terms of continuous and pulsed laser scanning. In order to verify the developed herein post treatment procedures, the tests were also upscaled to actual spinal cage implants. Furthermore, surface modifications affect its wettability which can be linked to cell adhesion and ultimately healing time of the implant. Hence Sessile drop tests were performed to assess the wettability and compare the effect of the various surface modifications.

For both SLM methods it was found that HIP reduces porosity of Ti6Al4V metamaterials, which reduces crack initiation sites and it also serves as a heat treatment increasing the β -phase fraction and thus increasing ductility and fatigue resistance. SB and CE were found to reduce surface indiscrepancies, which decrease the effect of stress concentration and fatigue initiation sites. Finally SB induces compressive residual surface stresses which means the surface is work hardened, increasing the overall mechanical properties.

For continuous SLM samples an increase in yield strength from 89 MPa up to 115 MPa was found by applying HIP treatment. It should be noted, however, that static mechanical properties were not affected by SB and CE treatments. Fatigue resistance, both low cycle (LCF) and high cycle fatigue (HCF), was significantly improved by a combination of HIP, SB and CE. The observed trend was similar for both pulsed and continuous SLM samples. It is worth noting that SLM samples manufactured with pulsing laser were found in general to be inferior to the continuous laser SLM, both in terms of static and dynamic properties. The difference is likely attributed to the nature of the laser scanning process, where for pulsing laser method each bead interconnection serves as stress concentration, while for continues laser it is rather the strut interconnections that act as weakest points. Furthermore, for the continuous SLM a preferred grain growth direction was observed which indicates anisotropy. This was not observed for pulsed SLM samples.

For the wettability results it was observed that SB decreases and CE increases the contact angle. A decrease in contact angle means the surface has become more hydrophilic, hence the in this study developed SB modification could be considered as more favourable for osseointegration.

The upscaled spinal cage implants post treatment procedure showed a decrease in yield strength and an increase in fatigue resistance for the HIP+SB+CE as compared to as-processed implants. The rather limited post treatment improvement on implants was linked to the post process treatment method, which should be modified to account for the complex geometry of these structures.

Contents

1	Introduction	1
2	Literature review	2
2.1	Selective laser melting	2
2.1.1	Continuous and pulsed SLM	3
2.2	Additively manufactured Titanium alloy Ti6Al4V	4
2.2.1	Topology	4
2.2.2	Microstructure and heat treatments Difference in microstructures of continuous and pulsed SLM • Sub-transus and Super-transus heat treatment • Hot isostatic pressing	7
2.2.3	Surface treatments Sandblasting • Chemical etching • Electropolishing	10
2.3	Mechanical properties and mechanical testing	11
2.3.1	Static compression	11
2.3.2	Compression fatigue Low cycle fatigue (LCF) • High cycle fatigue (HCF)	15
2.4	Osseointegration	18
2.4.1	Mechanical properties of bone tissue	18
2.4.2	Wettability Wettability testing • Experimental results in literature on contact angle measurements Ti6Al4V • Cleaning protocols for Sessile drop testing	19
2.4.3	Permeability	24
2.5	Implant design	25
2.5.1	Spinal cage implant	25
2.5.2	Mechanical testing of spinal cage implants	25
2.6	Conclusions literature review	26
2.7	Research objectives of this study	27
3	Methods	29
3.1	Materials	29
3.1.1	Materials for mechanical testing of cylindrical samples	29
3.1.2	Materials for mechanical testing of implants	30
3.1.3	Materials wettability study	30
3.2	Post process treatments	31
3.2.1	Sandblasting	31
3.2.2	Chemical etching	31
3.2.3	Hot isostatic pressing	32
3.3	Microstructural characterisation	32
3.4	Mechanical testing of cylindrical samples	34
3.4.1	Static compression testing of cylindrical samples Normalisation of compression cylindrical samples	34
3.4.2	Fatigue testing of cylindrical samples Normalisation of compression fatigue cylindrical samples	36
3.5	Mechanical testing of spinal cage implants	37
3.5.1	Implant and fixture design	37
3.5.2	Static compression testing of implants	39
3.5.3	Fatigue testing of implants	40
3.6	Wettability study	40
3.6.1	Sessile drop test	40
3.6.2	Dip test	41

4	Results	42
4.1	Microstructural characterisation cylindrical samples	42
4.2	Microstructural characterisation of spinal cage implants	50
4.3	Mechanical testing of cylindrical samples	52
4.3.1	Static compression properties of cylindrical samples	52
	Normalisation of compression cylindrical samples	
4.3.2	Results of compression fatigue on cylindrical samples	57
	Normal fatigue • Fatigue normalised with respect to yield strength • Fatigue normalised with strut thickness	
4.4	Mechanical of testing implant	63
4.4.1	Static compression testing of implants	63
4.4.2	Fatigue testing of implants	64
4.5	Wettability study	66
4.5.1	Sessile drop test	66
4.5.2	Dip test	67
5	Discussion	69
5.1	Behaviour of cylindrical Ti6Al4V samples	69
5.1.1	Microstructural comparison between continuous and pulsed SLM	69
5.1.2	Comparison of mechanical behaviour between continuous and pulsed SLM	70
5.1.3	The effects of post process treatments	71
	Hot Isostatic Pressing (HIP) • Surface Treatments	
5.1.4	Normalisation methods of dynamic properties of lattice Ti6Al4V	72
5.2	Mechanical behaviour of spinal cage implants	73
5.2.1	Mechanical properties	73
5.2.2	Design assessment	74
5.2.3	Accuracy of testing	75
5.3	Wettability	76
5.3.1	General observations	76
5.3.2	Comparison dip with contact angle	77
6	Conclusions	78
7	Recommendations	80
	References	81
	Appendices	84
A	SB optimisation	84
B	EDS results of SB after CE	88
C	Statistics of Sessile drop results	89

List of Figures

1	Schematic of the SLM process [7]	2
3	Structural integrity of pulsed SLM samples with interchanging laser power and exposure time [1]	4
4	Different topological designs used for compression testing (a) Cubic (b) Diamond (c) Truncated cube (d) Truncated cuboctahedron (e) Rhombic dodecahedron (f) Rhombicuboctahedron [5]	5
5	Results various mechanical properties from compression tests on different topological designs: Cubic (C), Diamond (D), Truncated cube (TC), Truncated cuboctahedron (TCO), Rhombic dodecahedron (RD), and Rhombicuboctahedron (RCO) [5]	6
8	A comparison in grain growth preference of continuous SLM (a) continuous SLM (b) and continuous+pulsed SLM [16]	8
9	A set of four subfigures.	9
10	Example for compression testing porous structures [12]	12
11	Compression tests on various heat treated and surface treated samples included in the research on pulsed SLM samples. AP= as processed, SB = sand blasted, T800 = annealed at 800 °C, T1050 = annealed at 1050 °C, HIP = Hot isostatic pressing, CE = chemical etching [4]	13
12	S-N curves of the afore mentioned different treated Ti6Al4V samples. [4]	15
13	Example fatigue crack initiation location of lattice structured Ti2448 produced with electron beam melting (crack located at yellow arrow) [23]	16
14	Schematic representation of contact angle measurements for (a) Sessile drop test (b) Wilhelmy plate method [30]	20
15	Contact angle hysteresis [30]	20
16	Wetting behaviour with respect to surface tension using young's equation [30]	21
17	Flat surface contact angle determination of droplet on a sphere and a cylinder compared to a flat surface for carbon steel [35]	23
18	Contact angle measurements of SB +AE (Acid Etched) Ti6Al4V samples comparing various etching times and the effect of passivation [36]	24
19	The Correlation between the permeability coefficient and the amounts of DNA, which was measured 1 day after cell seeding and calculated by computational fluid dynamics analysis [38]	25
20	A set of two subfigures.	26
21	A set of three subfigures on (a) Implant samples; (b) lattice cylindrical samples and (c) solid cylindrical samples	29
22	Figures regarding : (a) and (b)	32
23	A set of three subfigures on the cuts made for (a) lattice cylindrical samples [8]; (b) lattice cylindrical samples 37.5 ° (c) and implant samples	32
24	Two figures regarding the (a) square unit cell Ti6Al4V samples to observe preferential grain growth; (b) location of EBSD observation continuous SLM sample (- -). (c) location of EBSD observation pulsed SLM sample (■)	33
25	Figures regarding ISO 13314:2011 compression set-up: (a) The Zwick Z100 compression machine ; (b) The sample in compression	34
26	Simplified stress situation at a strut of a diamond unit cell [22]	35
27	Figures regarding cylinder compression fatigue: (a) MTS 858 fatigue machine; (b) sample compression fatigue	36
29	A set of two subfigures.	37
30	A set of four subfigures on parts of the ASTM F2077 set-up : (a) Pushrod; (b) minimal friction sphere; (c) ball and socket joint; and, (d) steel block.	38
31	Example equation to show momentum is low due to length of the pushrod	39
32	Figures regarding implant compression: (a) ASTM F2077 compression set-up ; (b) sample in compression	39
33	Figures regarding implant compression fatigue: (a) ASTM F2077 fatigue set-up ; (b) sample in compression fatigue	40
34	Figures regarding (a) optical tensiometer set-up (b) 3D printed sample holder to keep sample aligned for drop test	41
35	Set-up Dip test	41
36	A set of four subfigures on the microstructure of: (a) AP Continuous SLM; (b) HIP Continuous SLM; (c) AP Pulsed SLM; and, (d) HIP Pulsed SLM.	42
37	Figures regarding samples cut in 37.5° showing: (a) the preferential grain growth of continuous SLM and (b) the more random grain growth of pulsed SLM samples	43
38	EBSD images of: (a) Continuous and (b) Pulsed SLM showing α' grain orientation (c) Colour coded map for Inverse Pole Figure (IPF) of Alpha Titanium	44
39	Reconstruction of Beta phase in [100] IPF representation for (a) continuous SLM (b) pulsed SLM (c) Color Coded Map for Inverse Pole Figure of [100] Beta Titanium	45

40	Effect HIP on Vickers hardness (continuous SLM (CON) vs pulsed SLM (PUL))	46
41	Effect HIP on porosity percentage for continuous SLM samples (CON) and pulsed SLM samples (PUL)	46
42	Comparison of the measured strut thickness for the AP continuous SLM samples and the pulsed SLM samples.	47
43	Comparison of measured strut thickness of the following samples: AP, AP SB, HIP CE1 and HIP SB+CE2 (For the x-axis the data points are all shifted slightly around the whole number)	47
44	SEM images on the effect of surface modifications for continuous SLM samples	48
45	A set of four subfigures on (a) roughness continuous SLM HIP (b) roughness continuous SLM HIP CE1 (c) roughness continuous SLM HIP SB (d) roughness continuous SLM HIP SB+CE2	49
46	Effect surface modifications on the relative density of Ti6Al4V samples and herein also comparing continuous SLM samples (CON) with pulsed SLM samples (PUL)	50
47	Figures regarding the microstructure of: (a) AP implant sample (b) HIP implant sample	50
48	Figures regarding : (a) SB at the surface (b) SB at the core	51
49	Figures regarding : (a) AP implant unpolished (b) HIP SBCE implant polished	51
50	Mean compression graphs with 95% confidence interval of (a) comparison AP with SB on pulsed laser based SLM (PUL) (b) effect of HIP treatment in combination with SB on the static mechanical properties of pulsed laser based SLM (c) comparison AP with SB on continuous laser based SLM (CON) (d) effect of HIP treatment in combination with SB on the static mechanical properties of continuous laser based SLM (e) effect of CE1 and SB+CE1 on the static mechanical properties on continuous laser based SLM (f) reference graph comparing showing the difference in mechanical properties of the pulsed laser based samples and the continuous laser based samples	53
51	Figures regarding cylinder mean compression graph of AP continuous SLM samples with different relative density's (a) regular compression graphs continuous SLM (CON) 0.37 and 0.26 relative density ; (b) normalised compression continuous SLM 0.37 and 0.26 relative density (c) regular compression graphs 0.37 continuous SLM and 0.14 pulsed SLM (PUL); (d) normalised compression 0.37 continuous SLM and 0.14 pulsed SLM (PUL)	54
52	A set of subfigures regarding (a) mean compression graph AP and AP SB (b) mean compression graph for the relative density normalised AP and SB (c) mean compression graph AP, HIP, HIP CE1 and HIP SB+CE2 (d) mean compression graph for the relative density normalised AP, HIP, HIP CE1 and HIP SB+CE2	56
53	a set of sub figures regarding (a) All regular S-N curves (b) LCF of the pulsed laser based samples (c) HCF of the pulsed laser based samples (d) LCF of the continuous laser based samples (e) HCF of the continuous laser based samples (f)	58
54	a set of sub figures regarding (a) all normalised fatigue results with respect to yield strength (b) HCF of all normalised fatigue results (c) 90 % confidence interval of AP and AP HIP samples. (d) 90 % confidence interval of HIP and HIP SB samples (e) 90 % confidence interval of HIP, HIP CE1 and HIP SB+CE2 samples	60
55	fatigue results normalised to local stress including PUL samples	61
56	a set of five sub figures regarding (a) All CON curves local stress at the strut (b) HCF detail of the fatigue graphs (c) 90 % confidence interval comparing the AP 0.37 density and the 0.26 density with the HIP sample (d) 90 % confidence interval showing the local effect of SB (e) 90 % confidence interval showing the local stress effect of CE1 and HIP SB+CE2	62
57	a set of sub figures regarding (a) Mean compression results implant testing with 95% CI (b) compression results AP lumbar implant samples (c) Results HIPSBCE lumbar implant samples	63
58	A set of four subfigures on the lumbar implant fatigue (a) F-N curve regular (b) F-N curve normalised to yield force (c) F-N curve regular 90 % CI (d) F-N curve normalised to yield force 90 % CI	64
59	Failure propagation of HIP SB+CE implant representative sample with cyclic loading of 3.89 kN	65
60	Contact angle measurement boxplot with mean (red line) SD (black lines), confidence interval (blue lines) and outliers (+)	66
61	visual representatives of contact angle measurements, as provided by the contact angle measurements	67
62	Results Dip test wettability	68
63	Schematic comparison of the continuous and pulsed SLM methods	69
64	Damaged surface due to removal from print bed	70
65	Figures regarding : (a) Crack location for continuous SLM at the node (b) Crack location pulsed SLM between built layers [8]	71
66	Comparison of the effectiveness of normalisation for : (a) yield strength normalisation (b) local stress normalisation	73
67	Representative HIP SB+CE implant sample for indication failure locations loaded at 4,7 kN	74
68	The compressed cage failing location	75
69	Figures regarding (a) implant to POM block interface before load is applied (b) implant to POM block interface after load is applied and subsidence occurred.	75

70	Strut thickness measurement of pulsed AP+SB 4.5 bars 90 seconds with 180 μm powder compared with pulsed AP	84
71	Struts thickness measurement of pulsed AP+SB 3 bars 90 seconds with 180 μm powder compared with pulsed AP	85
72	Struts thickness measurement of Pulsed AP+SB 4.5 bars and 3 bars 90 seconds with 50 μm powder compared with pulsed AP	85
73	Strut thickness measurement of continuous AP+SB 3 bars 90 seconds with 180 μm powder compared with continuous AP	86
74	Figures regarding (a) the core of continuous AP+SB sample (3 bars 90s 180 microns powder) (b) and the core of continuous AP+SB 4.5 bars 90s 12 microns	86
75	Figures regarding (a) Continuous AP (b) Continuous AP + SB 3 bars 90s 50 microns (c) Continuous AP + SB 4.5 bars 90s 50 microns	87
76	EDS results obtained for continuous HIP SB samples at the core of the cylinder	88
77	EDS results obtained for continuous HIP SB+CE samples at the core of the cylinder	88
78	Figures regarding Tukey's test (a) for AP SB CE2 (b) and for AP CE2	89

List of Tables

1	Table which shows the effect of sandblasting on residual stresses measured at the surface [4]	11
2	An overview of the mechanical properties recorded over various of experimental studies [4,5,21,22]	14
3	An overview of the compression fatigue results recorded over various of experimental studies [2,4,22,24,25]	17
4	Mechanical properties of femur bone tissue [29]	19
5	An overview of the samples used in the compression and compression fatigue experiments on cylindrical samples	30
6	Sample overview of the implants used for the compression and compression fatigue experiments.	31
7	Overview of the samples used for the wettability tests.	31
8	weight and relative density implant samples	52
9	An overview of the compression test results for the cylindrical samples tested according to the ISO 13314 standard (CON = continuous SLM and PUL = pulsed SLM)	52
10	Comparison of continuous SLM AP ($\rho_{rel} = 0.37$), continuous SLM ($\rho_{rel} = 0.26$) and pulsed SLM ($\rho_{rel} = 0.14$) samples both regular and normalised	55
11	Comparison normal static compression results with the normalised to 0.35 relative density compression results . .	55
12	Results of compression tests of AP and HIP SB+CE samples	63
13	Table of the sandblasting parameters used to optimise the SB procedure (all samples were subjected to a rotation speed 20 RPM)	84
14	ANOVA statics table Sessile drop results	89

Nomenclature

AM	Additive Manufacturing
SLM	Selective Laser Melting
STL	Standard Tessellation Language
CON	Continuous SLM
PUL	Pulsed SLM
BCC	Body Centred Cubic
HCP	Hexagonal Close Packed
LCF	Low Cycle Fatigue
HCF	High Cycle Fatigue
AP	As Processed
HIP	Hot Isostatic Pressing
SB	Sand Blasting
CE	Chemical Etching
SEM	Scanning Electron Microscope
EBS	Electron Backscatter Diffraction
CI	Confidence Interval
CA	Contact Angle
EDS	Energy-dispersive X-ray spectroscopy
ANOVA	Analysis of variance

1 Introduction

In recent years a research focus has been to create bone implants from the additively manufactured titanium alloy Ti6Al4V. Additive manufacturing of implants brings along the advantage that patient specific dimensions can be applied to an implant [1]. Another advantage is that an intended porous structure can be created with a repeating unit cell resulting in properties which are not found in natural materials [2]. This porous structure is referred to as the lattice structure. The lattice structure causes the bulk to have stiffness values close to the properties of bone. This is beneficial for the load distribution around the implant which prevents bone resorption. The now uneven surface of the lattice structured implant has the effect of creating a better connection to the bone, because the bone will grow into the implant. Furthermore the Ti6Al4V alloy is used, because it has excellent biocompatibility properties.

Among other manufacturing techniques the process of selective laser melting (SLM) is used to create the titanium lattice structured implants. With SLM a laser melts metal powder to fuse together a product layer by layer upon which will be elaborated in the literature review. The manufacturing technique of SLM was invented in the mid-1990s by the company Fraunhofer ILT. Since then it has been growing in popularity and has found its use in many industrial sectors including the medical, aerospace, automotive and defence sectors [3]. In the late 2000s the use of a lattice structure was introduced for the use of bone implants.

In the most recent studies, an effort is made to improve the mechanical properties of SLM produced Ti6Al4V metamaterials using optimisation of topological design and post processing in the form of heat treatments and surface treatments [1, 2, 4, 5].

The current research will focus on the post processes of sandblasting (SB), chemical etching (CE) and hot isostatic pressing (HIP) to improve the compression strength and compression-fatigue resistance. A concern arose about the effects that the surface treatments have on the wettability of the implant which in turn would influence the bone to implant connection. Therefore the study of surface wettability in terms of roughness is also included. Ultimately the surface modified and heat treated metamaterials need to be applied in the actual implant design. Therefore compression and compression fatigue will be performed on actual implants in order to assess the benefits of post processing on full scale products.

The literature review (section 2) provides an extended overview describing among others the microstructures, the effects of HIP, SB and CE and how the experiments are to be interpreted. The method section 3 describes how the experiments were conducted and the materials used for the experiment. In the results section 4 the findings from the experiments are described. In the discussion section 5 the results are assessed in terms of accuracy, validity and value. Finally the report finished by concluding upon the results and discussion (section 6).

2 Literature review

2.1 Selective laser melting

With the manufacturing technique of selective laser melting (SLM) a laser is used to selectively melt powder to form predefined structures according to a computed design (Figure 1) [6]. A plateau is covered in a layer of powder to which a laser is subjected. The type of powder used is the material of the to be created part. Once the first molten layer is solidified a new layer of powder is spread out on the previous layer as the plateau is moved downwards by the layer thickness. The second layer is again subjected to the laser whereby a new layer of the final product is created. Sequentially like this the part is formed layer by layer. In the case of Titanium parts, the whole process needs to take place in an Argon filled environment due to the highly reactive nature of Titanium at higher temperatures.

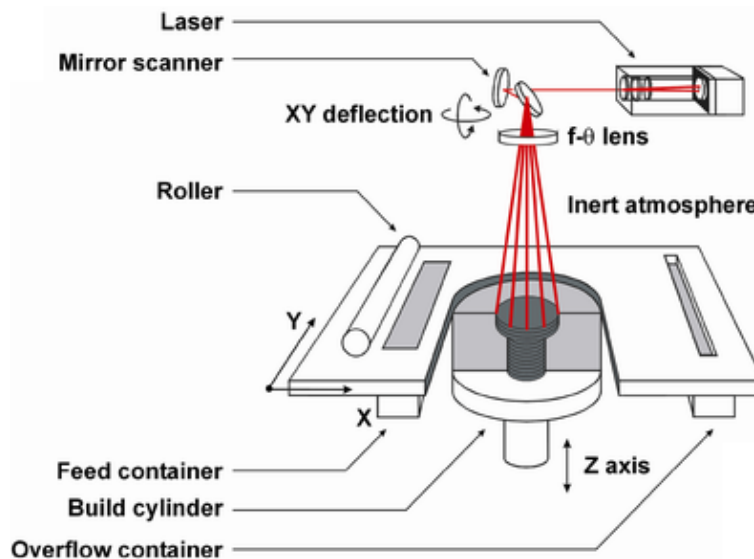


Figure 1. Schematic of the SLM process [7]

So-called as-processed (AP) parts created with SLM using the Ti6Al4V alloy do not have optimal mechanical properties. Due to the fast cooling rates the microstructure of the created parts consist of an α' martensite structure. This results in a high tensile strength but also a lack of ductility. The SLM parts also suffer from process induced defects like balling, unintended internal porosity, particles stuck at the surface and residual stresses.

- Balling is the phenomenon of insignificant wetting between the liquid and the solid layer resulting in an uneven interface with bulges. This uneven surface causes a lack of layer adhesion. By applying equation (1) the balling phenomenon can be optimised experimentally.
- Porosity is the formation of internal voids within the part due to either gas entrapment or balling. Gas entrapment leads to the more spherical shaped pores whereas balling causes a sharp thin pore. Internal pores have an influence on fatigue because fatigue crack growth can initiate within pores.
- Partially melted particles can be observed at the surface of the SLM produced parts. When the laser melts a certain area of the powder bed, the powder particles at the edge of the scanning area only partially melt, or they just get stuck within the melt pool. When a load is applied to the entire structure, these particles cause stress concentration areas, which act as fatigue crack initiation areas.
- Residual stresses are caused by thermal expansion and retraction in-between layers of material [8]. Due to solidification the new layer reduces in volume which, when simultaneously adhering and fusing together with the previous layer, causes internal stresses to remain within the part.

- Lack of fusion is the insignificant bonding between print layers due to insufficient reheating of the previous layer, which is caused by poor chosen print parameters. [9]

Despite all the present defects, a useful product can still be manufactured. However, improvements in the forms of post process heat treatment and surface modifications are often required to achieve sufficient reliability of the final product. The forthcoming chapter 2.2 will provide an overview regarding the various treatment and their effects.

It should be noted that the SLM process is influenced by a lot of process related factors. The controllable parameters regarding machine settings are the following: laser power P (W), powder bed temperature, scanning speed v (mm/s), hatch distance h (mm), focal offset distance and powder layer thickness t (mm). These parameters can be optimised according to the following formula:

$$E_v = \frac{P}{vht} \quad (1)$$

In which E_v (J/mm^3) is the to be optimised index called the energy density. By adjusting the parameters within equation (1) the extent to which the defects occur can be optimised. Besides the SLM machine settings two methods of scanning have been developed: the STL (Standard Tessellation Language) and vector based methods, which represent continuous and pulsed laser scanning respectively.

2.1.1 Continuous and pulsed SLM

As previously mentioned the additively manufactured titanium implants have a lattice structure which brings along many advantages. [1] The designing of these parts starts with creating a CAD drawing using specialised computer programs. These CAD drawings have to be converted to STL-files (Standard Tessellation Language-files) which then are converted to G-code by slicer programs. The G-code is what the 3D printer can read and will act on accordingly. During this process the slicer programs determine the way the layers are subjected to the laser. With the STL-based SLM technique, the laser scans the surface in a continuous manner (figure 2(a)). The dependency on the Slicer software, can design-wise be somewhat of a disadvantage because it is difficult to determine the exact way laser scanning occurs using these slicer software programs and it is inevitable that the struts are scanned in two separate paths.

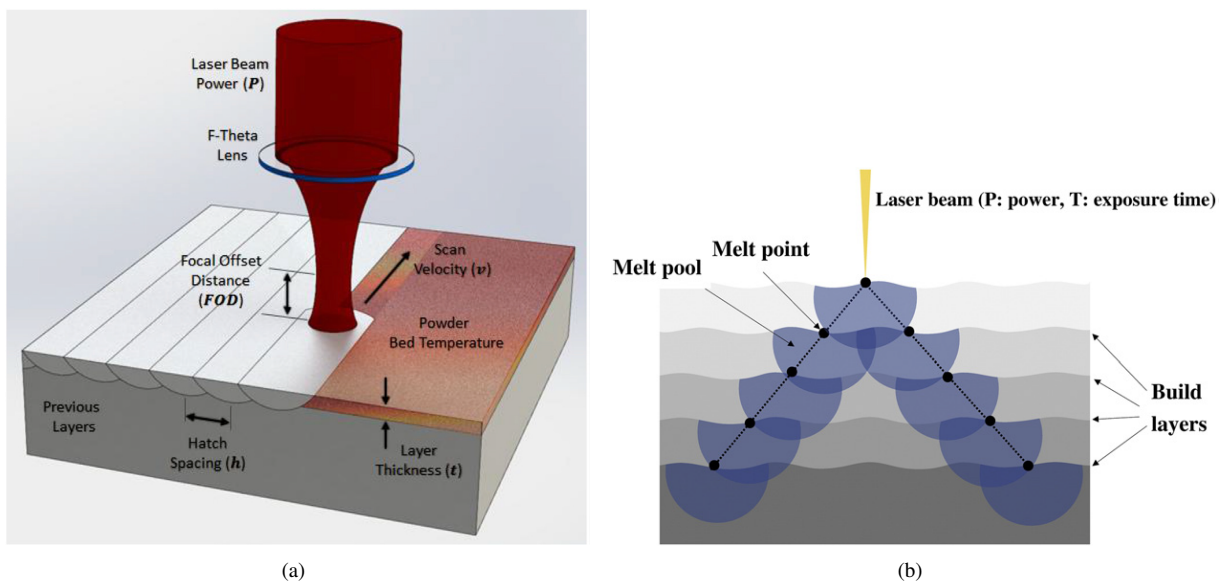


Figure 2. Figures regarding (a) schematic representation continuous SLM and [6] (b) schematic representation pulsed SLM [1]

For this reason a new method of vector based SLM was developed. In this method each strut of the lattice structure is programmed as a vector 2(b). The laser will scan the intersection point of the vector with the current layer in a single pulse. This way each layer within the strut is molten in one piece and the duration of the pulse essentially determines the strut thickness. This is then also the main advantage of the pulsed SLM, because the microstructure can be directly related to processing parameters, which is difficult for the continuous laser technique. Furthermore, the hassle of creating an STL and slicing it properly is not needed anymore.

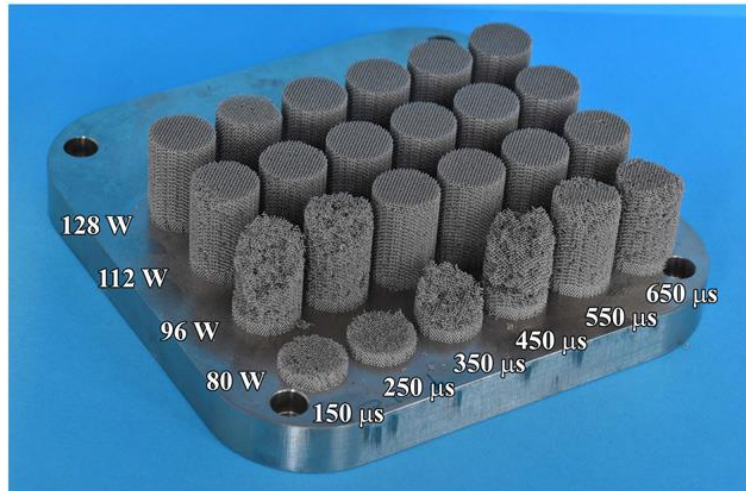


Figure 3. Structural integrity of pulsed SLM samples with interchanging laser power and exposure time [1]

Ahmadi *et al* [1] have worked on optimising the pulsed approach of SLM. In Figure 3 the physical result can be seen. The Vickers hardness is significantly increased with increasing exposure time and laser power. The surface roughness is not showing any significant effect with regards to the changing process parameters. An increase in laser power and or an increase in exposure time resulted in an increase in yield stress, relative density, first maximum stress, elastic modulus and plateau stress. As mentioned before with the continuous laser based approach the result of interchanging process parameters is always also dependent on the particular pattern of the STL file. The relation of laser power and the mechanical properties was found to be linear whereas the relation between exposure time and mechanical properties was found to be non-linear.

2.2 Additively manufactured Titanium alloy Ti6Al4V

Titanium alloys are extensively used as a material for biomedical applications. This is mainly because of their excellent biocompatibility followed by their corrosion resistance. Besides these properties, Titanium has great mechanical properties with respect to its density. As an example, Titanium alloys are used for hip implants, knee implants, dental implants and fixation bone screws. Ti6Al4V in particular is an alloy based on Titanium, which is vastly used within the medical field. Ti6Al4V consists of approximately 6%wt aluminium, 4%wt vanadium and the residual mass is covered by titanium. In addition Carbon, Iron, Nitrogen, Oxygen and Hydrogen can be present in small quantities depending on the grade of Ti6Al4V which is used. [10, 11]

2.2.1 Topology

The mechanical properties of additively manufactured parts can be improved by creating them with a mechanically beneficial topological design. Materials consisting of a repeating designed unit cell are categorised as metamaterials. Metamaterials are artificial materials which are designed so that they exceed the properties of their inherent ingredients. Figure 4 shows the different topological designs used by Ahmadi *et al* [5] for compression testing cylindrical samples consisting of the repeating unit cells. As can be seen all designs rely on a certain strut thickness, therefore for each design a set of samples was created varying in strut thickness. All samples were created using the Ti6Al4V material.

The different designs were tested and compared according to their relative densities. Results showed drastic differences

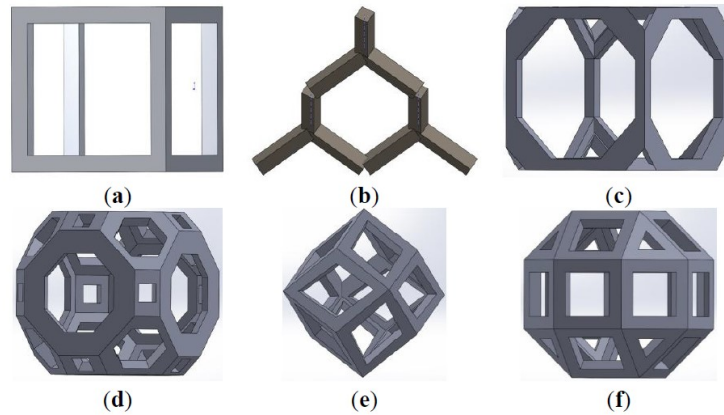


Figure 4. Different topological designs used for compression testing (a)Cubic (b) Diamond (c) Truncated cube (d) Truncated cuboctahedron (e) Rhombic dodecahedron (f) Rhombicuboctahedron [5]

in mechanical properties (Figure 5, table 2). The tests were performed according to ISO standard 13314:2011 [12]. All tests were performed on cylindrical samples with height 15 mm and a diameter of 10 mm. The diamond unit cell shows the weakest compressive performance. Truncated cuboctahedron, truncated cube, rhombicuboctahedron, and cube showed high stiffness properties and diamond and rhombic dodecahedron show a more ductile behaviour. As can be seen in figure 5 an increase in structural relative density results in an increase in elastic gradient, first max stress, plateau stress, yield stress and energy adsorption. The relative density is the density of the lattice structure divided by the density the structure would have as a solid.

Beside the static loading a more dynamic loading situation should also be taken into consideration when comparing the mechanical properties of the topological designs. A study performed by Ahmadi *et al* [2] compared the fatigue behaviour of Ti6Al4V additively manufactured parts consisting of diamond, rhombic dodecahedron and truncated cuboctahedron unit cells (table 3). The results implied that the material type is much more influential on the normalised S-N curve as compared to the topological design. This was observed because the same experiment was performed on a Co-Cr alloy. Another factor that is dominant in the normalised S-N curve is the surface quality as it is highly influential on the stress intensity. Phenomena such as surface imperfections and unintended pores effect the high cycle fatigue (HCF) much more as compared with the low cycle fatigue (LCF). So far topological design was primarily considered as the main method of effecting static and dynamic properties of lattice structures. However, lately a group at MSE (Materials Science and Engineering) department has been looking into the effects of microstructural design and surface engineering. Hence the follow up chapter will address these topics.

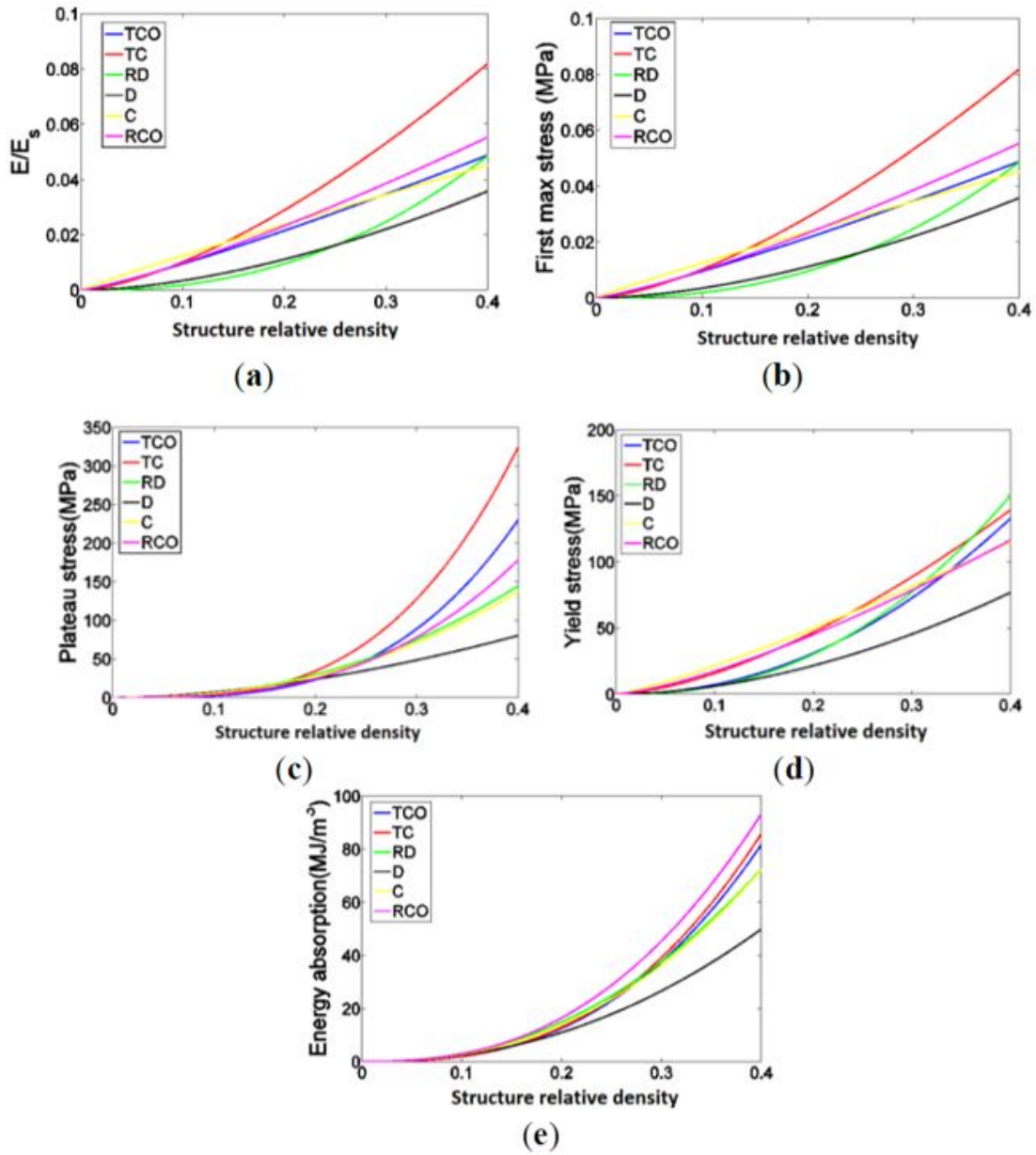


Figure 5. Results various mechanical properties from compression tests on different topological designs: Cubic (C), Diamond (D), Truncated cube (TC), Truncated cuboctahedron (TCO), Rhombic dodecahedron (RD), and Rhombicuboctahedron (RCO) [5]

2.2.2 Microstructure and heat treatments

At room temperature, when no heat treatment is applied, the microstructure of wrought Ti6Al4V consists of a mixture of α -phase and β -phase [8, 11, 13] (figure 6(b)). As shown in Figure 6(a) the α -phase has a hexagonal closed packed (HCP) structure which is stabilised by Aluminium and the β -phase has a body centred cubic (BCC) structure which is stabilised by Vanadium. The HCP structure is stronger though more brittle whereas the BCC structure provides more available slip planes, hence more ductility.

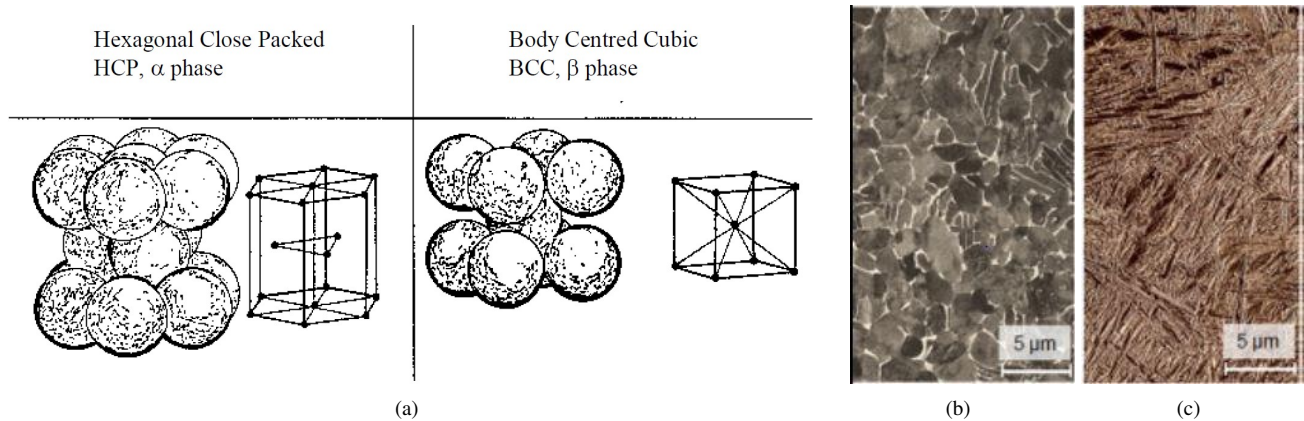


Figure 6. (a) Unit cell structures of Ti6Al4V [11] ; (b) wrought globular $\alpha+\beta$ -structure [14] (c) SLM as processed α' -structure [14]

When cooling an SLM processed sample from above the β transus temperature, a very slow cooling rate will result in an almost complete α -phase structure [8, 11, 13] (figure 7(b)). An increase in cooling rate results in an increase in α -phase nucleation rate at the grain boundaries of the β -phase grains. Hence instead of large regions of α -phase in the form of a grain the α -phase will nucleate as participates at the β -phase grain boundaries. When the cooling rate is increased even further the α -phase can even nucleate in the middle of the β -phase region. The shape of the α -phase participates is a platelet shape. At fast cooling rates the microstructure will form what is described as a basketweave structure. Finally when quenched the alloy will be fully transformed to a martensitic type of α' -phase (figure 6(c)). The martensite α' -phase consists of a metastable hexagonal structure.

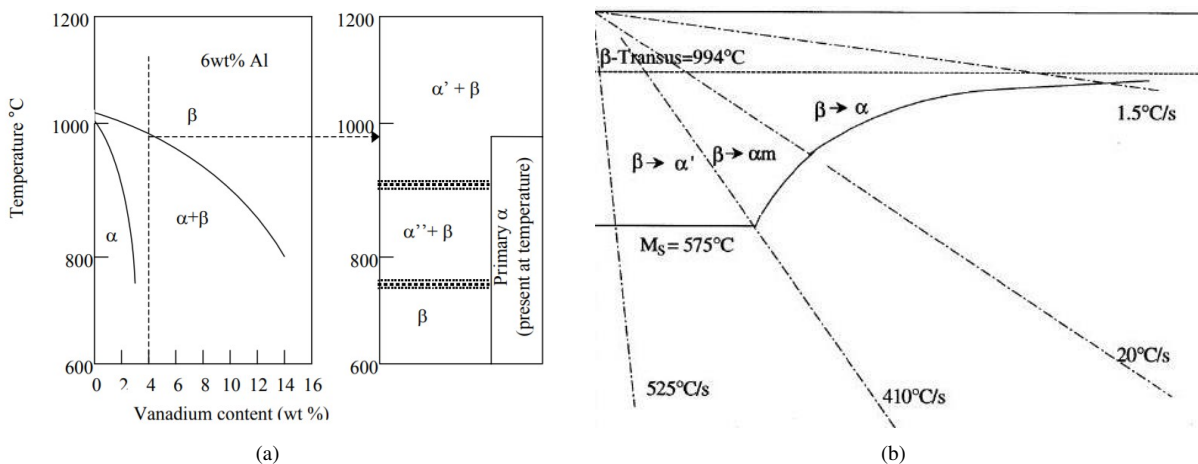


Figure 7. (a) Phase diagram Ti6Al4V [11] ; (b) schematic of cooling rates Ti6Al4V [8]

With additive manufacturing using the SLM technique the local melting followed by rapid cooling results mainly in a

α' -phase of acicular martensite [8, 9, 13]. However some studies also obtained an α -phase structure, likely due to the different printing parameters and in particular the laser power [15, 16]. For example Ravi *et al* [16] observed mostly α' -phase at 400 W laser power whereas at 1800 W the α -phase was mainly observed.

For SLM produced parts the formation of the martensite is within the β -phase and along the $\langle 001 \rangle$ build direction or sometime also along the strut direction depending on scanning method and print parameters. With this α' -phase present in the microstructure a certain brittleness is embedded into the structure. Therefore it is beneficial to subject the parts to heat treatments to assure a well needed combination of toughness and fatigue resistance.

2.2.2.1 Difference in microstructures of continuous and pulsed SLM

Nasser *et al* [15] performed a study wherein as-processed continuous and pulsed Ti6Al4V SLM were compared in terms of microstructure and Vickers hardness. In this study the obtained microstructure for both scanning methods was the α -laths composed in a Widmanstätten basket weave structure. The most significant difference in microstructure was observed to be the size of the α -laths which was wider for the continuous SLM samples. Furthermore it was observed that for pulsed SLM the width of the α -laths was also much more consistent throughout the sample whereas the continuous SLM grew wider when moving away from the surface. The difference in lath size can be contributed to the cooling rate which is reportedly higher for pulsed SLM. The increase in cooling rate provides the grains with less time to grow hence they are smaller. The Vickers hardness test showed that overall the finer α laths resulted in an increased hardness for the pulsed SLM samples compared to the continuous SLM samples.

Ravi *et al* [16] performed a study wherein AP continuous and AP continuous+pulsed Ti6Al4V SLM samples were compared in microstructure. The continuous+pulsed SLM samples were basically subjected to a block wave in laser power fluctuating between two levels of laser power. It was observed that continuous SLM resulted in a preferential grain growth direction of the prior β -grains where the combination continuous+pulsed SLM eliminated this preferential grain growth (figure 8).

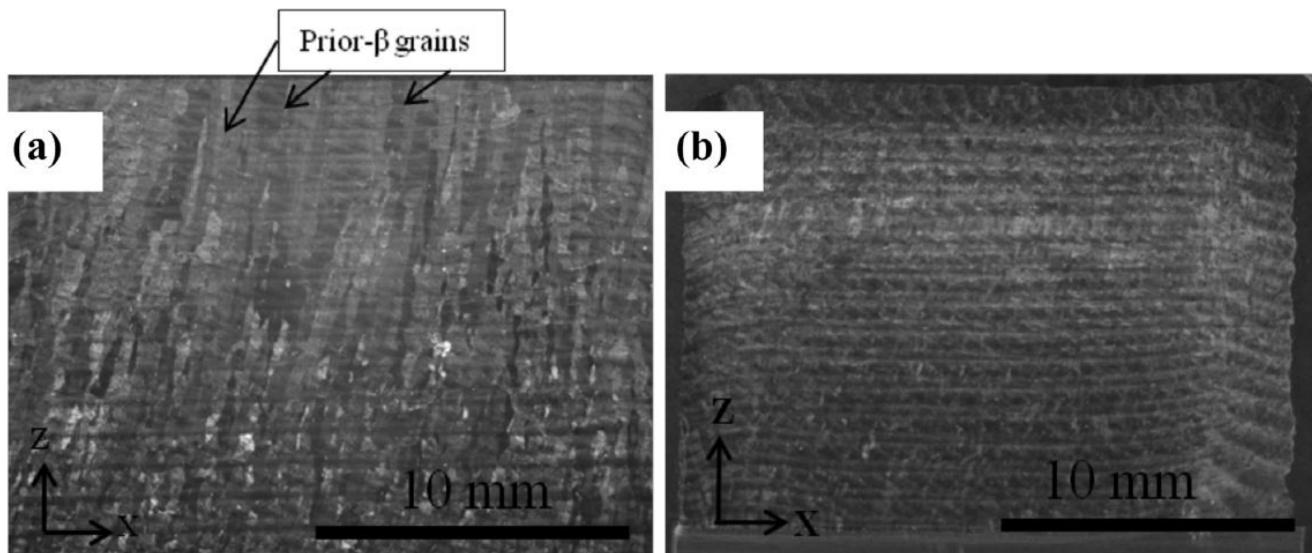


Figure 8. A comparison in grain growth preference of continuous SLM (a) continuous SLM (b) and continuous+pulsed SLM [16]

Li *et al* [17] performed a comparative experimental and computational study on the differences between continuous and pulsed SLM in terms of melt-pool motion, temperature and microstructure for Inconel 718. Regarding the melt-pool it was observed experimentally and in simulation that the pulsed SLM resulted in a pulsating melt-pool contracting when the laser was off and expanding when the laser was on. The continuous SLM melt-pool was a quasi-static in shape and size. The simulated

results show the pulsed SLM had a steep decrease and increase of temperature in sync with the pulse. Furthermore the pulsed SLM resulted in an almost doubled cooling rate compared with continuous SLM.

To the extent of the authors knowledge there is no study comparing the microstructural characteristics in α' -phase structure Ti6Al4V samples.

2.2.2.2 Sub-transus and Super-transus heat treatment

As shown in figure 7(a) in the range of 980-1000°C an equilibrium transformation from $\alpha+\beta$ -phase will occur to complete β -phase [4, 8]. A heat treatment starting at a temperature just below this transformation is referred to as a *sub-transus* heat treatment and a treatment starting just above the transformation temperature is referred to as a *super-transus* heat treatment.

By applying a *sub-transus* heat treatment the microstructure will transform from a martensitic α' phase (the as-processed condition figure 9(a)) to an α -phase and then to an $\alpha+\beta$ -phase. When heating up the α -phase nucleates at the grain boundaries of the α' phase and then the β -phase nucleates at the just created α -phase. The result when cooling down is a mixture of α and β -phase in lamellar structure whereby, when cooling was slow, the brittle α' -phase was eliminated.

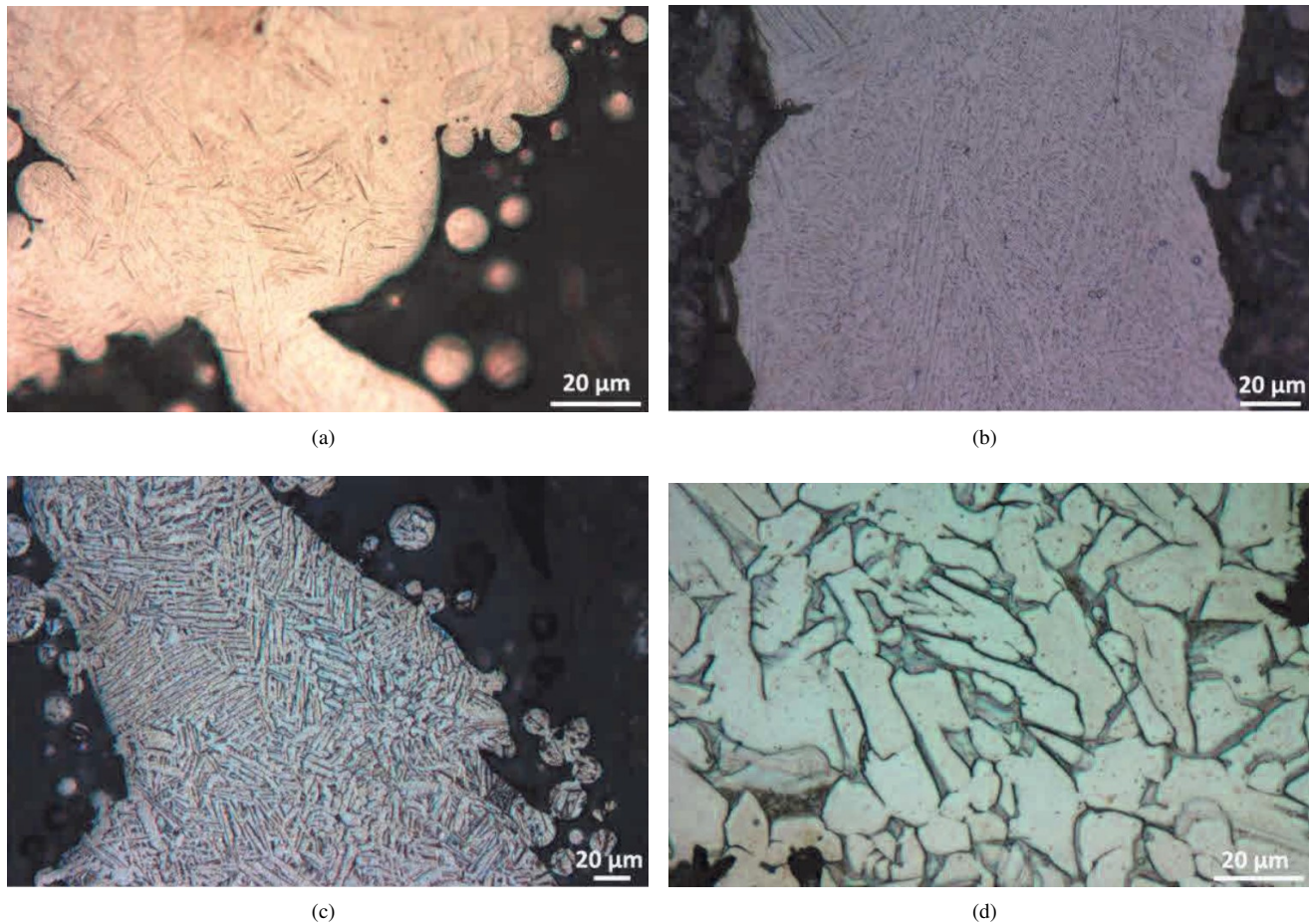


Figure 9. A set of four subfigures on the microstructure of: (a) AP treatment; (b) T800 treatment; (c) HIP treatment; and, (d) T1050 treatment. [4]

The *super-transus* method transforms the α -phase to a complete β -phase and then to an $\alpha+\beta$ -phase which will have a lamellar structure. In the *super-transus* heat treatment the SLM induced microstructure is completely altered due to the transition over the transformation temperature. Regarding the microstructure the difference in sub and super transus treatments is mainly the portion of formed β -phase and the shape of the grains which is more columnar with *super-transus* (figure 9(b),

9(d)). Ahmadi *et al* [4] used a *sub-transus* (T800) treatment at 800°C and a *super-transus* (T1050) treatment at 1050°C for pulsed SLM samples. The T800 treatment was heated for 150 min and the T1050 was heated for 120 min. Ahmadi *et al* [13] determined the β fraction to be $9.6\pm 0.6\%$ for T800 heat treatment and 20.4 ± 0.5 for the T1050 heat treatment. Both groups were heated in argon atmosphere and were also cooled with a constant cooling rate of 10 °C/min. The mechanical effects of these treatments will be discussed in the forthcoming chapters.

2.2.2.3 Hot isostatic pressing

Hot Isostatic Pressing (HIP) is another heat treatment used to improve the properties of SLM manufactured parts [18]. This heat treatment is generally used for ceramics to reduce unintended porosity. Hence when used for Ti6Al4V the technique will reduce the unintended porosity and transform the microstructure of the material to an $\alpha+\beta$ -phase. In the HIP process, a part is placed in an oven in which a pressurised gas is present, usually the chemically inert Argon is present. In the research by Ahmadi *et al* [4] the HIP treatment was applied at 920°C and with a pressure of 100 MPa for 120 minutes in an argon atmosphere. This means that the effect of the heat treatment on the microstructure can be considered as the *sub-transus* described in the previous chapter.

The effect of the reduction in pores size results in an increase in effective cross-sectional area which in turn causes a reduction of critical stress at the crack tip when considering fatigue loading. Kasperovich *et al* [14] reported that the thin pores exist due to the balling phenomenon at the layer interface, whereas the spherical pores exist due to gas entrapment.

2.2.3 Surface treatments

The goal of surface treatments on Ti6Al4V SLM produced parts would mostly be to improve surface quality which results in an improvement in fatigue resistance. Partly molten particles stuck to the surface act as crack initiation areas. Essentially, the insignificant bonding between the partially melted particles and the meltpool results in particle imprints on the surface which acts as notches [19]. However when comparing a notch with a partially melted particle the crack initiation behaviour is not completely identical because some bonding is still present between the particle and the surface. Furthermore the crack closing behaviour in a fatigue cycle is different as well, because the particle is bridging the crack mouth. This means that the size and depth of the particle stuck to the surface have effect on the crack initiation and thus also on the fatigue resistance.

2.2.3.1 Sandblasting

Sandblasting is a surface optimisation technique whereby abrasive particles are shot at a surface to create a smoother finish. The main objective of sandblasting the SLM surface is to remove the aforementioned partially melted particles stuck to the surface. Another important effect of the sandblasting is that it induces compressive stresses at the surface. Essentially the surface is plastically deformed inwards increasing the dislocation density at the surface.

In previous research by the MSE department *et al* [4] sandblasting is applied to the SLM parts in a sandblasting cabinet. Alumina (Al_2O_3) particles of the size 180 - 220 μm were shot at the SLM part which is rotating with a constant speed. This procedure is done for a period of 150 seconds. It is reported that using this procedure with a distance between struts of 300 - 400 μm , the abrasive effect had a good impact on the outer strut surfaces of the part. However the alumina particles were not able to fully penetrate into the structure leaving the inner struts unprocessed. Hence the SB procedure should still be optimised. In Table 1 the residual stresses are shown of the sandblasting procedure at the surface.

2.2.3.2 Chemical etching

With the surface treatment of chemical etching a chemical solution referred to as the etchant is subjected in this case to a Ti6Al4V surface. Chemical etching is used to dissolve the particles on the surface of the struts and it can also be used to clean the previously sandblasted surface from abrasive particles (figure 44). The abrasive particles need to be removed because they prohibit adhesion of cells to the implant surface. The etchant, which is usually a strong acid, reacts with the metal surface and forms bonds with Ti-atoms floating them away from the metal bulk. Essentially the top layer of the metal surface gets dissolves

Table 1. Table which shows the effect of sandblasting on residual stresses measured at the surface [4]

Specimen type	Peak width (FWHM, 2θ)	Crystallite size (nm)	Residual stress along the building direction (MPa)	Residual stress perpendicular to the building direction (MPa)
HIP (before SB)	0.14	108 ± 32	20 ± 13	7 ± 0.4
HIP (after SB)	1.40	14 ± 2	-245 ± 83	-132 ± 74

into the etchant. The type of etchant used will determine the chemical reaction that occurs, hence the type needs to be chosen carefully.

In previous research by Ahmadi *et al* [4] chemical etching was used as a surface treatment for the SLM printed Ti6Al4V structures. Here the parts were immersed in a 50 ml H_2O , 25 ml HNO_3 and 5 ml HF solution for 150 seconds. Limited penetration was observed, however for a different reason as compared with the sandblasting. The limited effect at the centre of the part most likely happened due to remainder of air bubbles in the structure prohibiting the etchant from treating certain areas. It is reported that the chemical etching surface treatment did not improve compression and fatigue properties due to the significant strut thickness reduction. Hence a study could be performed on the optimisation of the etching process.

2.2.3.3 Electropolishing

Electropolishing (ECP) has also been applied to Ti6Al4V lattice structures [20, 21]. Electropolishing is essentially the opposite process of electroplating. With electropolishing the sample placed in an electrolyte with a relative anodic material, where the sample functions as a cathode. The anode and cathode are connected to a power supply which increases the process speed. Atoms at the surface of sample will be ionised, float through the electrolyte and attach to the anode. In the previous research performed by Pyka *et al* [21], electropolishing in combination with chemical etching was applied with the focus on reducing surface roughness where also the mechanical properties were measured. As the material was removed the mechanical properties seemed to roughly be reduced by 50%, which is probably due to the strut thickness reduction of 22%. Electropolishing could potentially also be used to improve fatigue resistance as it improves the surface quality significantly, however it makes the surface smooth which could be a disadvantage for wettability behaviour. Upon wettability will be elaborated in the coming chapters.

2.3 Mechanical properties and mechanical testing

Ahmadi *et al* [4] performed static and dynamic mechanical tests on SLM printed Ti6Al4V cylindrical samples. The topology of the cylindrical samples was created as the diamond-based structure with repeating unit cells of the size 1 mm. The cylindrical samples were subjected to the various previously discussed treatments in order to see their individual and combined effects on the mechanical properties.

2.3.1 Static compression

Static compression tests were performed by Ahmadi *et al* [4] where conducted according to ISO:13314:2011 [12] which is a standard intended specifically for porous structures. The main difference between a compression test on a porous sample as compared on a solid sample, arises with the plateau stress involved in the compression test on the porous structure. What happens with the plateau stress is that the plastic limit of the struts is reached, however each layer of struts is allowed to fully deform before reaching a point where all struts are deformed, and the structure is pressed to an almost solid structure. This process is called densification and involves a huge amount of strain before all struts have deformed. With solid materials these struts are not present, and the material has to deform as a whole. Figure 10 shows an example of a porous structure compression curve Where σ_{pl} , the plateau stress, is defined as the mean of the stresses at 0.1 % or even less strain intervals between 20 % and 30 % or 20 % and 40 % compressive strain. The elastic gradient is measured in between the points of 20 % (σ_{20}) and 70 % (σ_{70}) of the determined plateau stress. The elastic gradient is not a material property but a function of the porosity type of the

structure. The end of the plateau is measured at σ_{130} , which is defined as the stress level at 130 % of the measured plateau stress. The compression yield stress is defined as the onset of plastic deformation and the first maximum stress is defined as the peak of the first wave in the compression test. With the compression test a compression speed is used to obtain a strain rate of between $10^{-3}s^{-1}$ and $10^{-2}s^{-1}$. For the test to be valid a minimum of 3 tested samples is required.

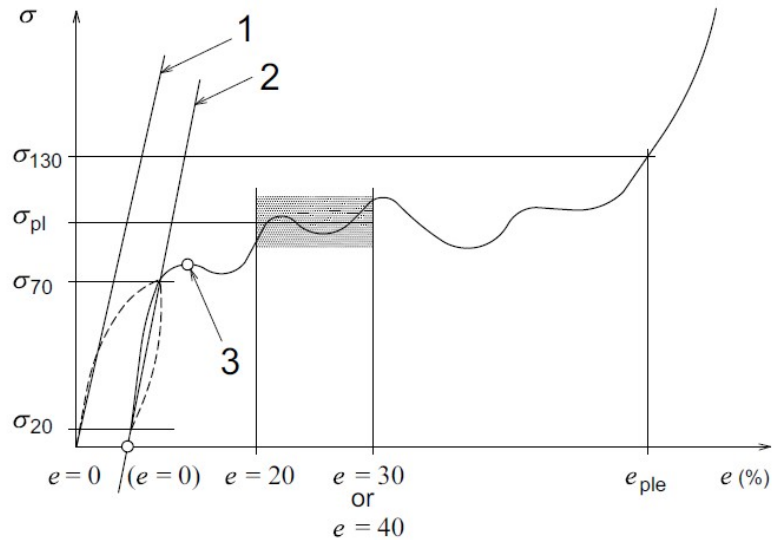


Figure 10. Example for compression testing porous structures [12]

Figure 11 shows the results of the compression tests on the various heat treated and surface treated specimens performed by Ahmadi *et al* [4] on pulsed SLM samples. All the specimens included in this compression test were produced using the pulsed method of SLM and had dimensions of 15 mm in diameter and 20 mm in height [4].

As can be seen in Figure 11, the first elastic region is in very similar when comparing the tested groups. The plateau region and the densification region differences can be observed. For example in the AP and the T800 samples, waves can be observed in the curve. This is probably due to the brittle nature of the AP samples due to the martensitic α' -phase present in the sample. Furthermore no densification was observed with the SB and T800 samples. The T1050 and HIP samples showed much less wavering and densification was observed. There were no significant differences observed in yield stress and first maximum stress with the exception of HIP treated samples. The HIP treated samples and the T1050 samples showed the best plateau stress. Table 2 gives an overview of the results from several papers regarding compression testing of Ti6Al4V samples.

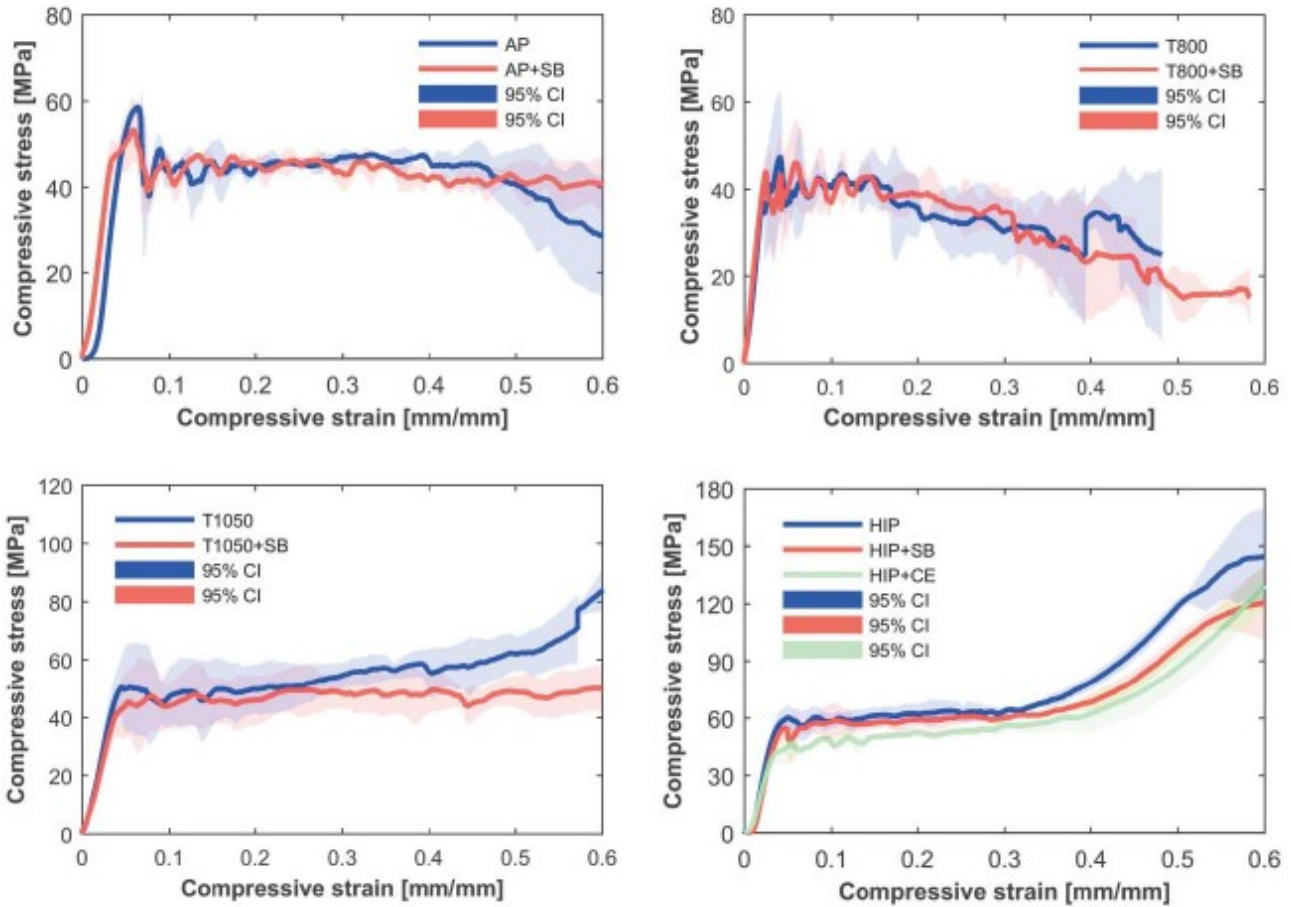


Figure 11. Compression tests on various heat treated and surface treated samples included in the research on pulsed SLM samples. AP= as processed, SB = sand blasted, T800 = annealed at 800 °C, T1050 = annealed at 1050 °C, HIP = Hot isostatic pressing, CE = chemical etching [4]

Table 2. An overview of the mechanical properties recorded over various of experimental studies [4, 5, 21, 22]

Source	Dimensions cylinder (mm)	Type of SLM	Type of unit cell	Type of treatment	Relative Density	Strut thickness (μm)	Pore cell size (μm)	Compressive yield stress (MPa)	First max stress (MPa)	Plateau stress (MPa)	Elastic gradient (GPa)
[5]	10 \emptyset - 15 h	continuous	Cubic	AP	34	823	1020	110	180	130	-
			Diamond		34	564	641	70	110	70	-
			Truncated Cube		20	620	1426	40	60	20	-
			Truncated Cubeoctahedron		34	564	1049	100	150	120	-
			Rhombicdodecahron		33	506	1058	90	120	90	-
			Rhombic Cubeoctahedron		32	438	794	90	130	90	-
			[4]	15 \emptyset - 20 h	pulsed	diamond	AP	32	-	-	46
	AP+SB	26				-	-	51	-	45	1.6
	T800	31				-	-	42	-	33	1.9
	T800+SB	27				-	-	43	-	33	2.1
	HIP	32				-	-	55	-	65	2.2
	HIP+CE	26				-	-	44	-	55	1.7
	HIP+SB	30				-	-	50	-	60	1.8
	T1050	30				-	-	50	-	55	1.4
	T1050+SB	29				-	-	47	-	49	1.3
[22]	10 \emptyset - 15 h	continuous	diamond	AP	34	-	-	90	119	72	4.3
				AP	37	303	-	102	128	74	4.9
				SR	34	288	-	104	118	80	4.9
				HIP2	40	325	-	119	147	134	6.6
				HIP2+CE	31	-	-	79	89	98	4.2
[21]	6 \emptyset - 12 h	continuous		AP	-	220	653	-	8	-	0.28
				CE	-	191	709	-	4	-	0.14
				ECP	-	170	724	-	4	-	0.14

2.3.2 Compression fatigue

Ahmadi *et al* [4] performed compression fatigue tests on several pulsed SLM samples with dimensions of 15 mm in diameter and 20 mm in height. In the range of 20 to 80 % of the yield strength, stresses were used as the amplitude for a fatigue test. At each amplitude the three samples were tested. The obtained fatigue data points were then plotted with a fitted power law to display an S-N curve. To compare the results, the different S-N curves were normalised according to their yield strength as can be seen in figure 12. This way a materials fatigue resistance can be compared with a materials initial static strength. When you select a material for a certain application the minimal thickness of the part will initially be determined by the yield strength of the material. The fatigue resistance does however not scale with yield strength, because it is not solely dependent on yield strength. Therefore some materials might have relatively suitable static strength properties, but in dynamic loading they might not be sufficient.

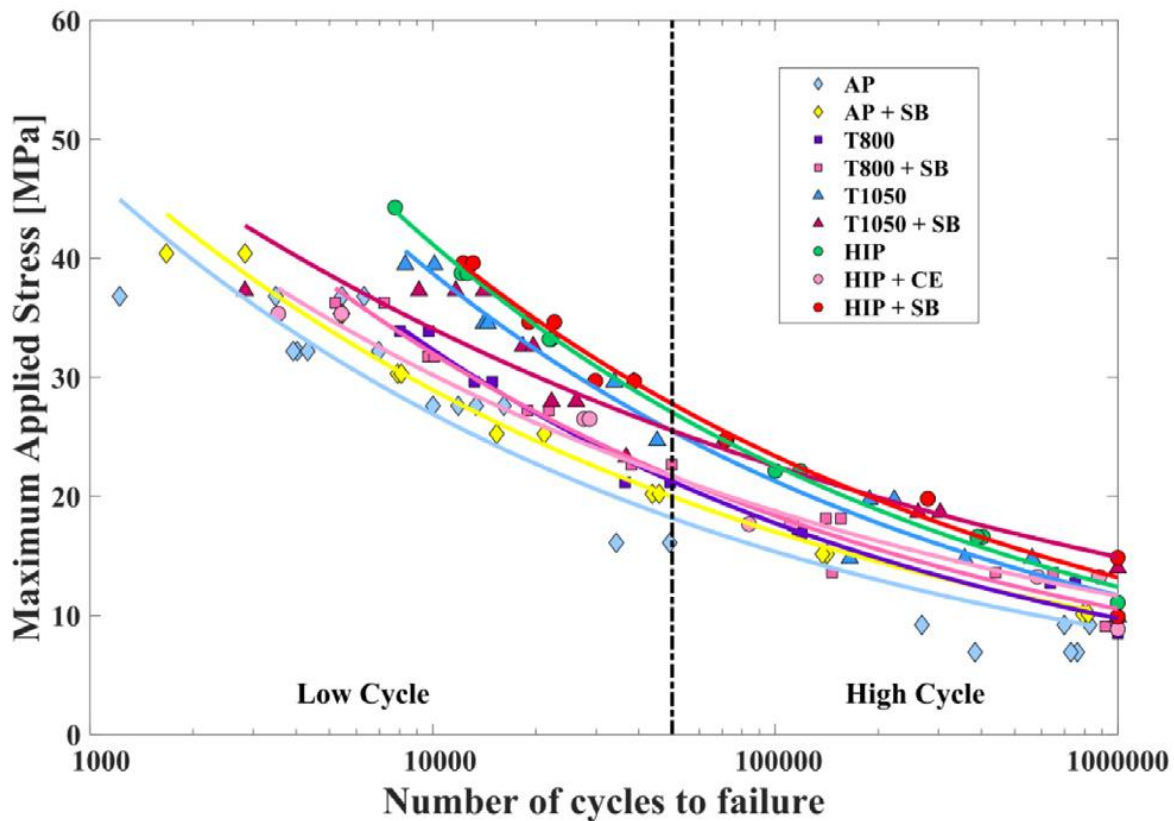


Figure 12. S-N curves of the afore mentioned different treated Ti6Al4V samples. [4]

When reaching a million cycles for fatigue life, the material was considered to be fatigue resistant for the corresponding stress. Figure 12 shows the fatigue life of the different heat-treated pulsed SLM cylindrical samples. Table 3 also shows an overview of all obtained fatigue results of various researches. These results will be discussed in the forthcoming chapters where the results are divided into low cycle fatigue (LCF) and high cycle fatigue (HCF). This division was made because LCF and HCF have different mechanisms of failure and thus different factors are influencing them.

The fatigue crack propagation in compression on lattice samples can generally be characterised in three phases [23]. The first stage is governed by the ratcheting effect which is small plastic deformation due to cyclic applied stress. The actual fatigue will initiate in the second stage. Here crack propagation has started but still some plastic deformation is occurring as well. In the third stage fatigue crack propagation speed increases dramatically and ultimately fatigue crack coalescence will occur which makes the material fail. For the continuous SLM samples the crack initiation area is expected to be on the nodes which is

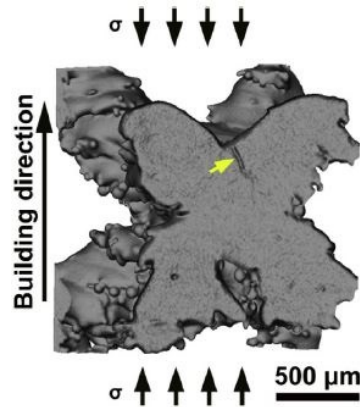


Figure 13. Example fatigue crack initiation location of lattice structured Ti2448 produced with electron beam melting (crack located at yellow arrow) [23]

where two struts meet and which is perpendicular to the loading direction. This is because, due to compression of the sample as a whole, tension is generated in this area (As is analytically shown in section 3.4.1.1). In figure 13 this crack initiation location is shown as an example for a similar compression fatigue sample as compared with the ones that will be used in the current research. For pulsed SLM samples the crack initiation is proven to be in between built layers [8]. This means that the critical stress concentrations are located differently for pulsed SLM compared with continuous SLM.

2.3.2.1 Low cycle fatigue (LCF)

Low cycle fatigue is the fatigue behaviour towards the 80 % of the yield strength, where a relatively low amount of cycles is needed for the sample to fail [4]. Most likely these levels of stresses will never occur when the implant is placed in the human body.

For the pulsed SLM samples shown in figure 12 the AP-group showed the lowest amount of cycles to failure and the largest scatter in results in the LCF regime. This is most likely caused by the surface indiscrepancies and the unintended pores still present in the structure. Both T800 and T1050 samples showed improved fatigue life which is likely due to the β -phase presence which increased the ductility. The effect of sandblasting is mostly reducing the scatter in results but does not significantly improve the LCF life of the T800 and T1050 groups. The HIP treated groups show the most promising results in LCF life which is probably due to the reduced unintended porosity which seems to be the dominant defect governing LCF failure. Chemical etching decreases the fatigue life in LCF when compared to samples where no chemical etching was applied, this is most likely due to thickness reduction.

Table 3. An overview of the compression fatigue results recorded over various of experimental studies [2, 4, 22, 24, 25]

Source	Dimensions cylinder (mm)	Type of SLM	Type of unit cell	Type of treatment	Relative Density	Strut thickness (μm)	Pore cell size (μm)	low cycle fatigue		high cycle fatigue	
								<i>At 0,8 normalised stress</i>	<i>At 0,7 normalised stress</i>	<i>At 0,3 normalised stress</i>	<i>At 0,2 normalised stress</i>
								(N cycles at failure)			
[2, 24, 25]	10 \emptyset - 15 h	continuous	Truncated cuboctahedron	AP	17 - 36	350 - 564	862 - 1049	6875	11173	243369	1063155
			Rhombic dodecahedron		16 - 34	140 - 251	486 - 608	2126	3313	55298	212683
			diamond		11 - 36	240 - 536	641 - 958	14244	22165	366543	1403488
[4]	15 \emptyset - 20 h	pulsed	diamond	AP	32			2755	4762	153439	808390
				AP+SB	26			2335	4162	163023	943080
				T800	31			8497	14200	369473	1757343
				T800+SB	27			6028	10491	352931	1898272
				HIP	32			7614	12700	326344	1542961
				HIP+CE	26			4755	9064	543248	3851946
				HIP+SB	30			11834	20231	607900	3097603
				T1050	30			9422	15746	409702	1948687
T1050+SB	29			5968	12533	1387886	13201969				
[22]	10 \emptyset - 15 h	continuous	diamond	AP	34			10^4	$2 \cdot 10^4$	$4 \cdot 10^5$	$> 10^6$
				AP	37	303		10^4	$2 \cdot 10^4$	$6 \cdot 10^5$	$> 10^6$

2.3.2.2 High cycle fatigue (HCF)

High cycle fatigue is the fatigue behaviour at lower stress levels compared with the yield strength, where a high amount of cycles is needed for the sample to fail [4]. The lower stresses used at HCF are reaching compatibility to the stresses subjected on the implant when it is placed within the human body.

For the pulsed SLM samples shown in figure 12 the results were similar compared with LCF, however there was one large exception. Sandblasting has a significant effect on the HCF life, which is most likely due to the decrease in particles stuck at the surface. The removal of the surface particles makes crack initiation more difficult. HIP+SB and T1050+SB are showing the best HCF life results. Apparently the crack initiation is favourable to occur at the surface instead of in the bulk when lower stress levels are applied. An overview of the performed compression fatigue tests is given in table 3.

In the current study a comparison will be made between the continuous and pulsed scanning method in terms of compression fatigue.

2.4 Osseointegration

Titanium is well suited for osseointegration because of its biocompatibility, corrosion resistance and mechanical properties. Bone is constantly changing its structure with regards to its biomechanical needs [26,27]. When an implant is embedded into the bone, the bone is naturally programmed to grow to the most efficient shape. Titanium integrated in bone tends to form a strong connection. The surface of the titanium implant is said to have a stable oxide layer with a high dielectric constant which enables proteins such as fibronectin to adhere to the surface. This will occur in the first few minutes of osseointegration. Once a stable protein layer is established cells are able to adhere to the surface, with in particular osteoblasts. Osteoblasts are cells associated with bone tissue growth. In the same time that cells adhere to the surface, bacteria start to attach as well. The bacteria attachment can prohibit cell growth and endanger the titanium to bone connection. If bacteria succeed in covering a larger area of the connection appose to cells it can lead to a condition called: periprosthetic infection (PI). This is an infection of the near implant tissue, which when not treated results in bone loss, soft tissue loss, reduced muscular function and ultimately implant failure and patient disability [28]. The acute case (detectable infection within 1 to 3 months) of this infection occurs about 1%-2% of all cases. The primary treatment for this infection is a combination of antibiotic intake and surgical removal of dead tissue which has a 60 to 80% success rate. Another strategy of handling PI is preventing it in the first place with surface engineering. The major challenge with treating PI using surface modifications is to create a surface which rejects bacteria growth and promotes cell adhesion and tissue growth. One hypothetical method is to create a surface with spikes in the 130–380 nm scale which cause stress across the bacteria cell membrane. The surface treatment of glancing angle sputter deposition (GASD) can achieve a structure like this. Another potential method is to embed Gallium ions in the titanium surface which can substitute iron in the metabolism of bacteria, which essentially plugs these processes.

An important parameter influencing osseointegration is wettability in terms of surface roughness. Essentially a smoother surface makes it difficult for cells to adhere to the titanium surface. Yet a too rough surface causes the cell layer to become uneven and have weak spots. Better wettability properties would improve time it takes for a strong titanium implant to bone connection. When cells have adhered, bone growth will occur over time.

2.4.1 Mechanical properties of bone tissue

As a Ti6Al4V implant is supposed to mimic bone it is important to understand the mechanical properties of bone [29]. It is difficult to mechanically characterise bone tissue because of its anisotropy and its non-homogeneity. It should be noted that roughly 65–70 % of a bone's dry weight is composed of Phosphate and Calcium. Collagen fibres account for approximately 25-30 % of the bone's dry weight. The residual percentages are consisting of a variety of proteins, polysaccharides and glycosaminoglycans. In which glycosaminoglycans serve as a connecting element in the collagen fibres. Another reason to address the mechanical properties of bone the effect of stress shielding [8]. With the stress shielding effect the bone to implant connection loosens due to mismatch in elastic modulus. Hence the lattice structure of the Ti6Al4V metamaterials provides a stiffness matching the ones of bones.

Within the bone two main macrostructures can be identified in the form of cancellous and cortical structure. The basic composition of material of the two types is identical, however the cancellous bone is much less dense because the internal pores size reaches millimetre scale. The cancellous type is then also observed as the core material whereas the surface layer is build up as the cortical structure. The cortical phase is actually approximately isotropic, linearly elastic and homogeneous, but this only accounts for a small portion of the bone. Table 4 shows a table where some mechanical properties of the Femur bone are shown.

Table 4. Mechanical properties of femur bone tissue [29]

Property	Femur, Human (20–39 years)
Ultimate tensile stress (MPa)	124 ± 1.1
Modulus of elasticity in tension (GPa)	17.6
Ultimate compressive stress (MPa)	107 ± 4.3
Ultimate percentage contraction	1.85 ± 0.04

The bones tested in Table 4 were in the wet condition, which is very important because dried out bones show different properties. It needs to be mentioned that bone properties are also greatly affected by mineral content which follows a person's lifestyle. Hence when creating an implant, it is not possible to have something with the exact same properties and a range of properties has to be offered instead.

2.4.2 Wettability

As mentioned before wettability is a materials affinity to a liquid in terms of surface contact [30]. Wettability is often quantified through the contact angle. When a droplet is placed on a surface, the angle it forms between the droplet and the material surface is the contact angle. The contact angle is a function of the surface energies of the involved solid liquid and gas in combination with the surface roughness. The wettability is said to influence the cascade of events that occurs when the implant is placed within the bone.

There are multiple ways of measuring the contact angle of which the Sessile drop test is probably the most used. With this test a droplet is placed on a surface of which the contact angle is measured visually. This is shown in Figure 14. Measured contact angles between 0° and 90° are considered hydrophilic and angles reaching close to 0° considered superhydrophilic. Measured contact angles between 90° and 180° are considered hydrophobic with angles reaching 180° being referred to as superhydrophobic. Gravitational forces and surface tension forces are acting on a droplet laying on the surface. When performing a Sessile drop test it is important that the gravitation forces acting on the droplet are negligible which is accomplished by creating droplets which are very small. This is needed because gravity flattens the droplet and distorts the contact angle measurement. For the gravity to be negligible the diameter of the droplet needs to not exceed the following relation:

$$L_c = \sqrt{\frac{\gamma_v}{\rho g}} \quad (2)$$

In which L_c is the capillary length (m), γ_v liquid vapour surface tension ($\frac{kgm}{s^2}$), ρ is the liquid density ($\frac{kg}{m^3}$) and g is the gravitational acceleration ($\frac{m}{s^2}$). For water this maximum diameter cannot exceed the capillary length of 2,7 mm which in practice amounts to the usage of 1-5 μ l droplets.

When considering the roughness with the droplet diameter it is important the diameter of the droplet is as large as possible compared with the scale of roughness. It can hereby be concluded that the most accurate Sessile droplet test using water requires a droplet of 2,7 mm.

Another method for doing contact angle measurements is the Wilhelmy plate method. In this method a plate is submerged into the liquid and the contact is measured indirectly at the plate to liquid to vapour interface (Figure 14). This is done using the

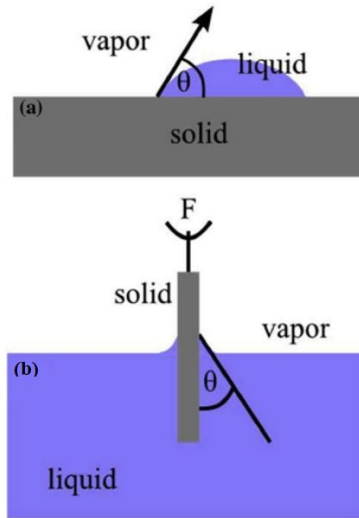


Figure 14. Schematic representation of contact angle measurements for (a) Sessile drop test (b) Wilhelmy plate method [30]

following formula:

$$\cos\theta = \frac{F_w}{L\gamma_{lv}} \quad (3)$$

where θ is the incremental contact angle, F_w is the measured force (N) at the end of the plate, L is the perimeter of the plate and γ_{lv} is the liquid vapour surface tension. One advantage of the Wilhelmy plate method is that the dynamic contact angle can easily be determined by measuring the force and calculating the contact angle. Another advantage is that the test is not hindered by evaporation of the volumetrically small Sessile droplets. Dynamic contact angle is a phenomenon where the contact angle of the drop changes with movement. Hence by immersing the sample with a defined speed the dynamic contact angle can be measured. Dynamic contact angle measurements give rise to contact angle hysteresis which is shown in Figure 15. The contact angle changes as the wilhelmy plate is receding or advancing. It is concluded that this occurs because of the surface indiscrepancies such as roughness, entrapped air and inhomogeneous in terms of hydrophobicity.

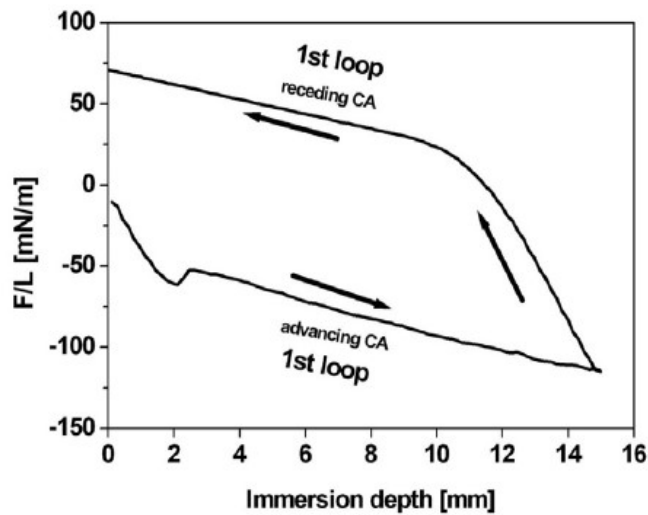


Figure 15. Contact angle hysteresis [30]

The contact angle measured with dynamic contact angle measurement is therefore more accurate because it accounts for more of an average contact angle over the entire area as opposed to a single measurement [31]. The most stable contact angle can be estimated according to:

$$\theta_{most\ stable} = \frac{\theta_{adv} + \theta_{rec}}{2} \quad (4)$$

Where the θ_{rec} , θ_{adv} and $\theta_{most\ stable}$ are the average receding, average advancing and most stable contact angle, respectively.

As mentioned before wetting is a function of surface energies of the liquid, solid and vapour involved in combination with the surface roughness of the solid. One can imagine the bulk of a solid is all structured atoms in an energy efficient structure. Ergo all atoms have a certain amount of bonds with atoms around them. When the structure ends at the surface some atoms must have fewer bonds than the atoms at the bulk resulting in the surface energy. When the surface is perfectly flat the contact angle is only affected by the surface energy and the following relation is valid:

$$\cos\theta_{young}\gamma_{lv} = \gamma_{sv} - \gamma_{sl} \quad (5)$$

Which is referred to as Young's equation. In the equation θ_{young} is Young's contact angle, γ_{lv} is the surface tension at the liquid vapour interface, γ_{sv} is the surface tension of the solid vapour interface and γ_{sl} is the surface tension at the solid liquid interface. When only considering contact angle wetting is favoured by combining a high energetic solid surface with a liquid with low surface tension. Hence γ_{lv} needs to be minimised and $\gamma_{sv} - \gamma_{sl}$ needs to be maximised. Figure 16 shows the wetting behaviour with respect to the surface tensions and the resulting contact angle.





Energetic relationship	CA relationship	Optical representation	Macroscopic result
$\gamma_{sv} - \gamma_{sl} > 0$	$0^\circ \leq \theta \leq 90^\circ$		High wettability
$\gamma_{sv} - \gamma_{sl} > \gamma_{lv}$	$\theta = 0^\circ$		Complete wetting (spreading)
$\gamma_{sv} - \gamma_{sl} < 0$	$90^\circ \leq \theta \leq 180^\circ$		Low wettability
$\gamma_{sl} - \gamma_{sv} > \gamma_{lv}$	$\theta = 180^\circ$		Non-wetting

Figure 16. Wetting behaviour with respect to surface tension using Young's equation [30]

Surface roughness also influences the contact angle. The first influence of roughness is simply an increase in surface area of the solid due to the relief. Hence the following relation is determining the Wenzel contact angle (θ_w) where an increase in

surface area is accounted for by the roughness factor

$$\cos\theta_w = R_w \cos\theta_{young} \quad (6)$$

Where the roughness factor (R_w) is the ratio in real surface area and projected surface area. An important feature of the wenzel contact angle is that it shows that inherently hydrophilic materials become more hydrophilic and inherently hydrophobic materials become more hydrophobic.

Other phenomena observed at for example the leaves of a lotus flower, is the entrapment of air within the surface structure allowing the water droplet to only contact the microscopical mountain tops of the rough surface. This then in fact reduces the surface area instead of increasing it. When this is the case the Cassie-Baxter equation is valid:

$$\cos\theta_{CB} = f \cos\theta_{young} + f - 1 \quad (7)$$

Here f is the surface fraction in contact with the liquid. This relation is however only really valid for structures where the roughness is induced by a pillar like structure which assures air entrapment (This is the case for the lotus flower). For a lot of materials, the air will probably get trapped in some parts of the surface whereas in others it will not. This causes an impossibility to measure the surface fraction in contact with the liquid for such materials. Frank Rupp *et al* [30] determined the contact angle of as processed Titanium to be 50° where a roughness factor of 1.7 was used. For acid-etched and sandblasted titanium surfaces a contact angle of 67° was measured. If an inherently hydrophilic material is measured to have a contact angle higher than 90° There must be an air entrapment. equation (7) can also be used to estimate the wettability of a lattice material [32], however the effects of liquid entering the lattice structure are not accounted for.

The phenomenon of the Petal effects has also been observed on titanium implants. Here essentially large groves at the surface roughness do allow the liquid to fully adhere whereas the smaller groves still have air entrapped. This way the surface can be strongly hydrophobic whereas the droplet is still attracted to the surface.

Frank Rupp *et al* [30] reports that titanium surfaces with a mean 3D height of roughness peaks between approximately 1 and 2 μm shows the best osseointegration properties.

2.4.2.1 Wettability testing

As is mentioned in the previous chapter the most common methods of measuring contact angle are Sessile drop test and Wilhelmy plate method. When considering that the to be measured contact angle is for a lattice structure, the wilhelmy plate method would not be sufficient. This is because when the lattice structure is hydrophilic it will act like a sponge and intake all the liquid which highly increases the measured force on the plate due to the weight. This will give a distorted measurement. When considering the Sessile drop test the problem arises that the liquid will be partially immersed in the lattice structure and therefore decreasing the contact angle. Few studies have done Sessile drop tests on porous structures [33, 34]. Zhang *et al* [34] reported that the contact angle increased with increase in pore size up to a certain point where it decreased again. This makes sense as first the air trapped in the voids increases the contact angle as more air comes in contact with the droplet. As the pore increases in size at a certain point the droplet will partially immerse in the pore which again decreases the measured contact angle. Cassie *et al* [32] developed an equation converting porous surface contact angle to intrinsic surface tension contact angle, which is namely equation (7). So this time, again the assumption is made to only include the surface in contact with the liquid and no inclination of the drop is accounted for. With the pore size used to create the Ti6Al4V metamaterials a droplet will most definitely be distorted by pore inclination, thus a Sessile drop test on a lattice structured titanium surface would not be useful.

Guilizzoni [35] developed a mathematical method to convert a contact angle measurement on a curved surface to the value of the equilibrium contact angle on a flat surface. The main difference in contact angle of a curved surface with a flat surface contact angle is that the base line of the angle is not a straight line but a tangent line of the curved surface. Hence if the surface is curved in a constant spline a measurement would not give a different result as compared with a flat surface. However, when

the surface is not curved in a constant manner it results in an asymmetric droplet. When this is the case the contact angle can be measured at different points on the contact line and the measurements can be plotted against their angle between tangent and normal (referred to as the base angle). An example of this plot is shown in figure 17. This way a theoretical stable angle can be obtained of the irregularly curved material.

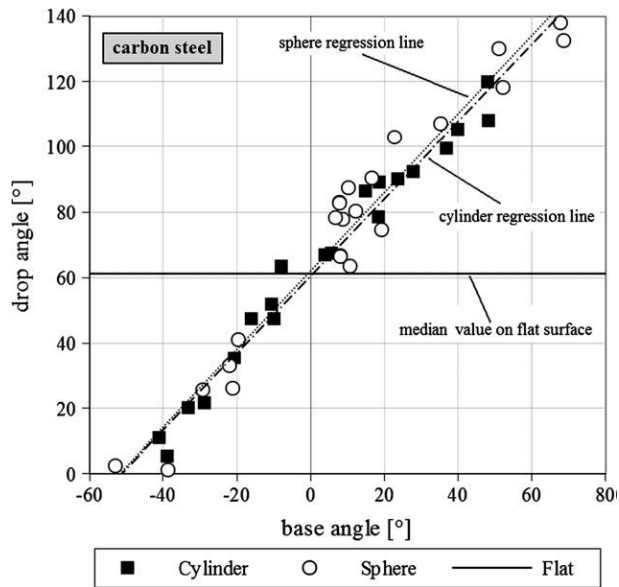


Figure 17. Flat surface contact angle determination of droplet on a sphere and a cylinder compared to a flat surface for carbon steel [35]

The Sessile drop test could be applied to the titanium metamaterials in several ways. A flat surface of additively manufactured titanium is used to mimic the structure of the actual metamaterial. A challenge here would be to apply sandblasting in an equal fashion to how it is applied on the circular samples used for mechanical testing. A second option would be to print a solid cylinder which would simulate a single strut but at a larger scale. The cylinder would need to be the same size as the cylindrical samples used for the fatigue and compression tests because this way the heat treatments and surface modifications can be applied in an almost identical manner.

In a certain way soils can be considered as a porous media as well [31]. For the contact angle measurement of soils the capillary rise method is used. In this method a table is pressed of the soil and this is placed in a tube opened on both ends. The soil at the bottom of the tube is introduced to liquid which will react by moving upwards the tube. The following relation is valid in the capillary rise method:

$$l^2 = \frac{rt\gamma_v \cos\theta}{2\mu} \quad (8)$$

in which l is the liquid penetration height, γ_v is the surface tension at the liquid vapour interface, θ is the contact angle, r is the pore radius, t is the time required and μ is the liquid viscosity ($Pa \cdot s$). With this formula the contact angle can be estimated of the soil if the soil were to be a flat surface. Theoretically this test could be applied on the titanium metamaterials, however this has not yet been done before.

2.4.2.2 Experimental results in literature on contact angle measurements Ti6Al4V

Strnad *et al* [36] performed Sessile drop tests on flat SB and CE wrought Ti6Al4V samples. SB was performed using 250 - 300 μm SiO_2 particles for 10 min and CE was performed using a 1:1 ratio of H_2SO_4 and HCL . CE was applied at various temperatures (60°C 80°C and 100°C) and for various time frames (1, 3h, 6h, 12h and 24h). Passivation was performed in 30%

HNO_3 at room temperature. It was found that SB prior to CE was beneficial for wettability behaviour at increase acid time lengths which is shown in figure 18. It was shown in this study that the effect of solely SB was devastating for the contact angle increasing it from 60° up to 82° . The effect of SB on the roughness was reported to increase the roughness from $1.2 \mu\text{m}$ to $3.3 \mu\text{m}$. Furthermore it was found that increasing the CE time resulted in a decrease in contact angle. Increasing the temperature of the CE bath was disadvantage for wettability behaviour as it increased the contact angle. Finally it was found that the passivation treatment only had an effect after SB where it increased the contact angle. The overall best results of a 46° contact angle were obtained using SB and CE for 24 h at 60°C .

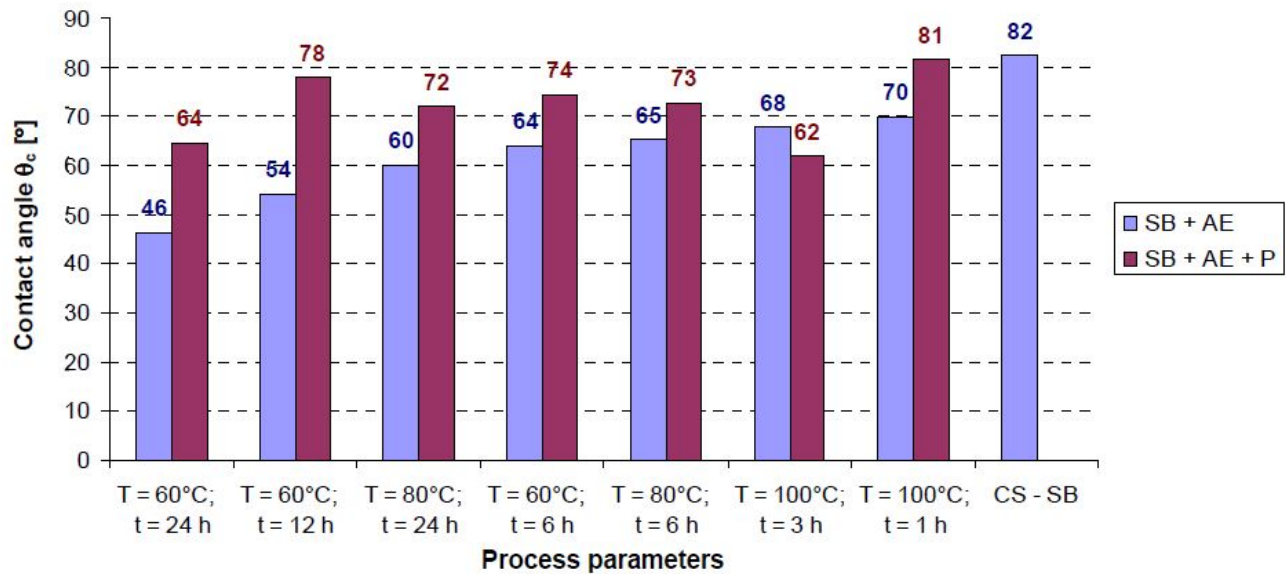


Figure 18. Contact angle measurements of SB +AE (Acid Etched) Ti6Al4V samples comparing various etching times and the effect of passivation [36]

2.4.2.3 Cleaning protocols for Sessile drop testing

The wettability behaviour of surfaces is influenced by the cleaning procedure subjected upon the material [37]. It is most likely that due to this phenomenon the reported contact angles in literature vary from 40° to 80° for Ti6Al4V. Hierro-Oliva *et al* [37] performed contact angle measurements on solid wrought Ti6Al4V using a variety of cleaning protocols. The study concluded that controlled passivation growth in water conditions in combination with 10 minutes ultrasonic cleaning using antiseptic liquid, acetone and ethanol followed by 1h drying at 120° oven and desiccator gives the best results in terms of reproducibility, scatter and accuracy. Passivation is the process of the Ti6Al4V reacting with oxygen to form a stable passive oxide layer. If passivation is controlled and equal for all specimens it reduces the scatter in results.

2.4.3 Permeability

Permeability is the ability of a porous structure to allow for fluids to flow through the medium [38]. There is a correlation between permeability and osseointegration. When a fluid travels through a porous medium with a certain pressure behind it, the size, shape and density of the pores determines the speed at which the fluid can flow through the medium. The speed at which a fluid travels through a medium has an effect on the degree to which cells are able to adhere to the surface of the medium. A medium with small barely connected pores will have a much slower flow and therefore cells will be able to adhere better as compared to a medium with large pores (figure 19). Regarding the shape, a trend can be seen where designs with more corners improve cell adhesion because cells can bridge the corners here. For the growth of cells larger pores tend to be beneficial because there simply is more space to grow towards and because the oxygen supply is higher due to the higher fluid

flow velocity.

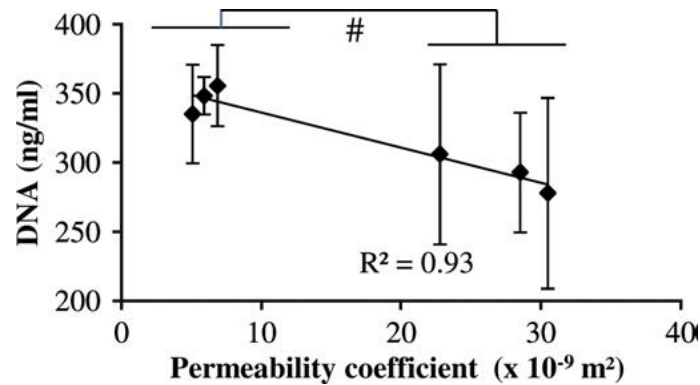


Figure 19. The Correlation between the permeability coefficient and the amounts of DNA, which was measured 1 day after cell seeding and calculated by computational fluid dynamics analysis [38]

When applying these results to implants it would be beneficial for an implant to have larger pores on the outside and smaller pores on the inside. this way the larger pores allow for fluid flow whereas the smaller pores allow for initial cell attachment.

2.5 Implant design

The goal of the research is to contribute to the development of SLM produced implants. Therefore one must know about the final use of the material. The current study focuses on the application of the Ti6Al4V lattice metamaterials on spinal cage implants.

2.5.1 Spinal cage implant

Spinal fusion is used to relieve pain and pressure on the spine by fusing two vertebra together [39]. The pain is often caused by the wearing out of the cartilage bone vertebra disc (degenerative disc disease). Among other methods a spinal cage is used to serve as a replacement of the vertebra disc. Over time the vertebra bone will fuse with the spinal cage and the adjacent vertebra bone. The human spine consists of five major sections: the slightly lordotic cervical (neck), the kyphotic thoracic (mid back), the lordotic lumbar (lower back), the sacral region and the coccyx region (tailbone). As the shape of every section is different they require different size and shapes of implants. The current study will focus on implants for the lumbar region. In figure 21(a) the Amber Implant design is shown. This design can be inserted into the spinal via the PLIF (Posterior Lumbar Interbody Fusion) method. The implant is specifically designed for the worst case scenario of the vertebra having an above average intra-vertebral height.

2.5.2 Mechanical testing of spinal cage implants

Mechanical tests on irregularly shaped object bring along some difficulties. ASTM F2077 - 18 [40] was developed to regulate the mechanical testing of spinal implants. This standard testing method can be used to compare different spinal cage designs and give an indication on the mechanical properties. The standard does not serve as a performance standard because of the significant differences in implant design over the various manufacturers.

For the compression and fatigue tests a specially designed fixtures and set up are needed. Figure 20 illustrates the required set-up design.

The set up consist of two test blocks shown in figure 20.b. In the case of compression tests these blocks need to be constructed out of stainless steel with a minimum ultimate tensile strength of 1310 MPa. When considering fatigue testing the same shape of test blocks is required but this time the material polyacetal needs to be used with an ultimate tensile strength with a minimum of 61 MPa. This eliminates the range of different bone properties a vertebra can have when for example considering the age of a person. This is achieved by reducing wear on the blocks as polyacetal is very wear resistant. The surfaces of the blocks need to simulate the vertebra and therefore need to have a shape following the contour of the spinal cage. It should

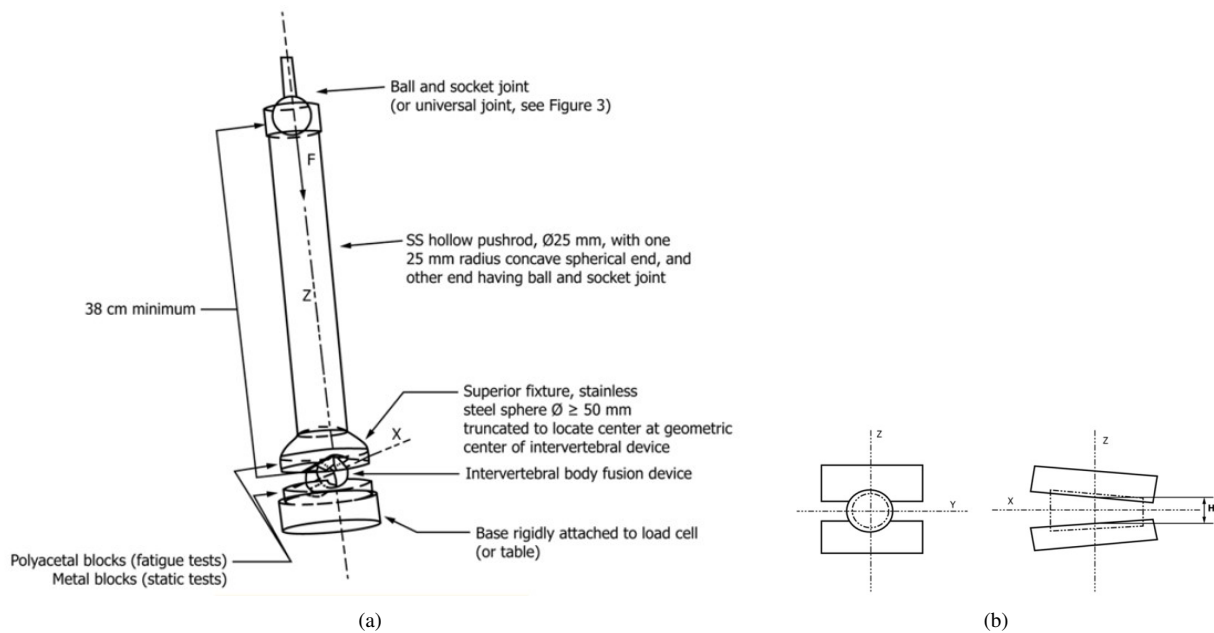


Figure 20. Figures regarding ASTM F2077: (a) test set-up ; (b) test blocks [40]

be noted that this is different for every specific design. Note here that this is different for every design. If a pocket is needed in the surface of the blocks this may not be deeper than 3 mm. The polyacetal blocks can only be used once for a test, the stainless steel blocks can be reused. The height H in figure 20.b needs to be between 4 and 8 mm. The blocks need to be rigidly attached to the rest of the set-up. The rest of the set-up consist of a pushrod attached to a superior fixture with a minimal friction sphere joint. This type of connection allows the surface of the pushrod to follow the deformation of the sample. The pushrod is attached to the compression or fatigue machine via a ball and socket joint (or another joint that allows for alignment in the xy -plane of the pushrod). The pushrod needs to have a 25 mm diameter. The superior fixture must be a concave spherical shape with the centre of its radius aimed at the centre of the to be tested spinal cage. It is important that the length of the pushrod is longer than 380 mm. This will increase the flatness of the blocks surface when aligning the pushrod.

With the compression test a compression speed is to be maintained of not faster than 25 mm/min. Pre-loads of 100 and 500 N are to be used for cervical and lumbar spinal cages respectively. A minimum of 5 samples is to be used for a single valid measurement of properties.

For the fatigue test a fatigue limit of 5.000.000 cycles is to be reached by the specimen for the test to be satisfactory. An S-N curve needs to be established over a minimum of 6 samples. The force amplitude used for the test is to be at 25 % 50 % or 75 % of the materials ultimate static force. With fatigue testing it is important to note any defects like crack propagation on the specimen after 5.000.000 cycles or failure.

2.6 Conclusions literature review

SLM manufactured Ti6Al4V lattice structured metamaterials show many benefits to be used for bone implants. Among the two methods of SLM the continuous SLM shows better mechanical properties whereas the pulsed SLM process is easier to control in terms of machine parameters.

Among the several heat treatments applied to the titanium, the HIP treatments showed the most promising results, because it has a dual effect of reducing the martensitic α' -phase and reducing internal porosity. Which in turn improve the static compression properties and the compression fatigue properties. Due to the reduction in pore size they are less likely to result in becoming crack initiation sites.

Sandblasting is shown to mainly improve the fatigue behaviour in high cycle fatigue because of the reduction in particles

stuck at the surface and the introduction of residual compressive stresses on the surface. Chemical etching has the effect of removing the surface particles, however it is hypothesised that the reduction in strut thickness is too much and therefore counters the positive effects. Chemical etching does have the effect of removing sandblasting particles when applied after sandblasting, but by removal of the top layer may result in removal of the induced residual stresses.

Potentially a study could be done on the effects of electropolishing on the mechanical properties of Ti6Al4V metamaterials.

When reviewing the applied tests it can be noted that the order in which heat treatments, sandblasting and chemical etching were applied has not yet been looked at.

Topology has great effect on the static mechanical properties however not so much on the fatigue behaviour. The diamond structure which is used in most research is said to have a more ductile mechanical behaviour.

Regarding the normalisation of the fatigue tests an indicative normalisation can be made on by normalising to the yield strength. However one could also plot the yield strength to the analytic max stress at the strut. In this parameter the difference in strut thickness is accounted for. One should however apply the mathematic model carefully as for example the crack initiation site on pulsed SLM samples have a different location.

An inherently hydrophobic surface can only get more hydrophobic by roughening the surface. A hydrophilic surface can when considering the Wenzel state become more hydrophilic because more hydrophilic surface is created. However when the induced roughness causes the hydrophilic system to be in Cassie-Baxter state, where air is entrapped in the roughness the system can actually become more hydrophobic. The air reduces the hydrophilic surface area and air itself is hydrophobic.

To perform a Sessile drop test on a lattice structure is impossible due to the effect of liquid infiltration into the lattice surface. Therefore a simulated solid surface subjected to the same treatments could be produced to be used for the Sessile drop. A test needs to be designed to check if the reaction of water to the lattice samples is similar to the solid samples. Another method could be to use a capillary rise method to measure the contact angle, however this has never been done before making it difficult to validate the results.

For the mechanical testing of spinal cage implants a specialised fixture needs to be realised and machined according to ASTM F2077 [40] standard.

2.7 Research objectives of this study

The primary objective of this research is to investigate biomechanical properties of additively manufactured Ti6Al4V metamaterials and implants as a function of various post-processing treatments and additive manufacturing parameters.

In order to achieve the primary objective the following research questions are set:

1. What is the microstructural and mechanical difference between continuous and pulsed SLM Ti6Al4V metamaterial?
2. How does the hot isostatic pressing (HIP) effect the properties of Ti6Al4V lattice structures?
3. Can surface modifications in terms of sand blasting and chemical etching be optimized and what is their effect of the mechanical properties of SLMed lattice Ti6Al4V?
4. Can static and dynamic mechanical data of various groups of Ti6Al4V metamaterials be normalised with respect to the yield strength and the local stress?
5. Can the developed herein post processing be upscaled to the actual implants and what would the mechanical response of such implants be?
6. What is the effect of the surface modifications on the wettability behaviour?

In order to answer the above questions the current research is divided into 4 experimental categories:

- **Multiscale characterisation:** various characterization methods will be performed on the microstructural and structural effect to assess the effect of heat treatments and surface modifications. Characterisation is performed in order to gain a better understanding of obtained mechanical testing results and its relation to the microstructure and surface properties.
- **Mechanical testing of SLM lattice Ti6Al4V:** A mechanical comparison (both static and dynamic) between AM cylindrical metamaterials produced with continuous and pulsed SLM samples will be performed. The goal is to determine the differences between the two techniques and the effects of post process modifications on the static and dynamic mechanical properties. Furthermore, two different ways of normalisation of mechanical data for various metamaterials will be performed and compared.
- **Mechanical testing of spinal cage implants:** The post processing procedure producing best results on sub-scale metamaterials (see previous category) will be applied on full scale spinal cage implant in order to establish validation for an actual implant's application. The ASTM F2077 standard will be used to show the mechanical behaviour and in particular the limits of the lattice metamaterial within the implant design.
- **Wettability testing of cylindrical samples:** a sessile drop and dip tests will be performed on solid and lattice cylindrical Ti6Al4V samples featuring various post process surface treatments. Based on the measured contact angle and qualitative assessment of dipping test an estimate can be made on the effect of surface treatments on the implant's adhesion to the bone.

3 Methods

In this chapter the methods will be discussed by which the experiments were prepared and conducted.

3.1 Materials

In this section the materials used for the mechanical testing and wettability testing will be discussed. The sample design described in section 3.1.1, which will be used for the mechanical testing of the Ti6Al4V metamaterial, is shown in figure 21(b). The samples used for the implant testing, described in section 3.1.2, are shown in figure 21(a). The samples used for the wettability testing, described in section 3.1.3, are shown in figure 21(b) and figure 21(c).

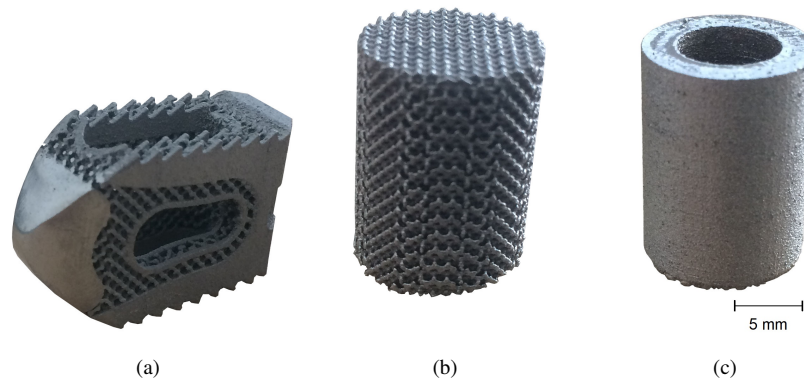


Figure 21. A set of three subfigures on (a) Implant samples; (b) lattice cylindrical samples and (c) solid cylindrical samples

3.1.1 Materials for mechanical testing of cylindrical samples

All cylindrical samples involved in this section were created with a height of 20 mm and a diameter of 15 mm. All the cylindrical samples were manufactured using the diamond structure.

The pulsed SLM samples were manufactured using plasma atomized, spherical Ti6Al4V extra low interstitial (ELI) powder with a particle size of 10 - 45 μm (produced by: AP&C Advanced Powders and Coatings Inc., Boisbriand, Canada). The SLM machine used to process the powder is equipped with a single fibre laser (produced by: IPG Photonics Corporation, Oxford, USA) with a wavelength range of $1070 \pm 10 \text{ nm}$. The laser power was set to 128 W and the exposure time was set to 550 μs .

The continuous SLM samples were manufactured with Ti6Al4V ELI powder with a particle size of 20-63 μm (grade 23) from SLM Solution Group AG, Lubeck, Germany. The SLM machine is equipped with Twin (2x 400 W) IPG fibre lasers (IPG Photonics Corporation, Oxford, USA) with a wavelength range of $1070 \pm 10 \text{ nm}$. The samples were manufactured using a Layer thickness of 30 μm and scan speed of 10 m/s.

As can be seen in table 5 the cylindrical samples were divided into three main sample groups. The first group was manufactured using pulsed SLM with an apparent relative density of $14.4 \pm 0.3 \%$. The second group was manufactured using the continuous SLM with an apparent relative density of $37.2 \pm 1.9 \%$. The third group was again manufactured with the continuous SLM, but with an apparent relative density of $26 \pm 0.4 \%$. The three groups were then subjected to the following heat treatments and surface modifications (In section 3.2 the treatments are explained further):

- AP : As-processed
- HIP : processed at 920 °C for 2 hours with application of pressure at 100 MPa in an inert atmosphere where-after the samples were furnace cooled at 10°C/min.
- SB : Sandblasted for 90 seconds at 4.5 bar with a rotation speed of 20 RPM. Dental powder Schuler's S-U-Alustral aluminium oxide with an average particle size of 50 μm was used for this surface modification.

- CE1 : 50 mL H_2O , 25 mL HNO_3 , 5 mL HF , 2 minutes in ultrasonic bath.
- CE2 : 50 mL H_2O , 25 mL H_2SO_4 , 25 mL HCl , 60 minutes in ultrasonic bath.

Table 5. An overview of the samples used in the compression and compression fatigue experiments on cylindrical samples

Type of SLM	Sample groups	Number of samples compression	Number of samples fatigue	Average relative density %	SD %	Average measured strut thickness μm	SD μm	Average calculated strut thickness (equation 10) μm
Pulsed laser based	AP	3	15	14.37	0.27	226	14	274
	AP SB	2	17	11.97	0.16	184	17	247
	HIP	3	14	14.43	0.11			274
	HIP SB	3	14	13.71	0.18			267
Continuous laser based	AP	3	14	37.29	0.71	377	68	476
	AP SB	2	14	34.59	0.53	403	56	454
	HIP	3	15	36.90	0.93			473
	HIP SB	3	13	36.04	0.64			466
	HIP CE1	3	12	34.83	1.4	376	27	456
	HIP SB+CE2	3	13	31.80	0.98	369	34	432
Continuous laser based	AP	3	15	26.36	0.44	353	22	383

the AP, AP SB, HIP and HIP SB groups were selected to check the effect of post process treatment and to compare herein the two scanning methods. The surface treatment of CE was selected to further improve the lattice cylindrical samples and to remove the SB particles. Hence it was only applied to the HIP group. The 0.26 relative density continuous laser AP sample was selected to verify normalisation methods, upon which will be elaborated in section 3.4.1.1.

The relative density was measured using the technique described in section 4.1. Though at parts inaccurate, the average strut thickness was measured using SEM (JOEL, JSM-6500F, Japan) as described in section 4.1. The calculated strut thickness was determined using equation 10.

3.1.2 Materials for mechanical testing of implants

All implants were created using the Ti6Al4V ELI (grade 23) powder size 20-63 μm . The machine used to produce the implants as the SLM 280 HL (SLM Solutions Group AG), Twin (2x 400 W) IPG fibre lasers (IPG Photonics Corporation, Oxford, USA) with a wavelength range of 1070 ± 10 nm. All implants were created with a layer thickness of 50 μm and a scan speed of 10 m/s.

All implants were manufactured using the continuous SLM method of SLM using an apparent density for the lattice structure part of 20 %. The samples were subjected to the same treatments as described in section 3.1.1 with the exception of the SB and CE treatment duration. Here SB was applied for 150 seconds. The CE treatment was only applied for 60 seconds to remove the residual SB particles from the structure, hence the effect of CE on the structure is negligible. Table 6 shows the sample types used for the compression and compression fatigue experiments of implants.

3.1.3 Materials wettability study

The surface modifications which were applied to improve the mechanical strength also have an effect on the wettability behaviour of the material. Therefore all the types of surface modifications were applied on the samples used for the wettability tests. In table 7 an overview is given of these samples. The lattice samples are used for the Dip test and the solid samples are used for the Sessile drop test (to be discussion in section 3.6). The treatments applied are identical to those used in section 3.1.1.

Table 6. Sample overview of the implants used for the compression and compression fatigue experiments.

Sample type	Number of samples for compression	Number of samples for fatigue	Average weight	SD
			g	g
AP	5	6	3.974	0.028
HIP SB+CE	5	6	3.735	0.060

The porous and the solid samples were manufactured with Ti6Al4V ELI powder with a particle size of 20-63 μm (grade 23) from SLM Solution Group AG, Lubeck, Germany. The SLM machine was using a Twin IPG fibre lasers (IPG Photonics Corporation, Oxford, USA) with a wavelength range of 1070 ± 10 nm and each laser has power of 400W. The samples were produced using a layer thickness of 30 μm and scan speed of 10 m/s. The lattice structured samples were created with a relative density of 37.2 ± 1.9 %.

Table 7. Overview of the samples used for the wettability tests.

Surface treatment type	Number of lattice structured samples	Number of solid samples	Number of measurements solid samples
AP	2	1	8
AP+SB	2	1	8
AP+CE1	3	1	8
AP+CE2	3	1	8
AP+SB+CE1	3	1	8
AP+SB+CE2	2	1	8

3.2 Post process treatments

Sandblasting (SB), Chemical etching-1 (CE1), CE2 and hot isostatic pressing (HIP) were applied on the samples described in section 3.1. In this chapter the set-up for applying these modifications and treatments are described.

3.2.1 Sandblasting

The process parameters for sandblasting were optimised in terms of SB particle size, blast pressure (appendix A). particles of the size 180 μm , were not able to penetrate into the core of the sample, whereas particles of the size 12 μm did not have a significant effect. For both pulsed and continuous SLM samples, 50 μm powder for 90 s with a pressure of 4.5 bars and a rotation speed of 20 RPM turned out to be the best parameter combination, where the core of the sample was reached, but the outer struts were not heavily damaged. As can be seen in figure 22(a) the SB chamber (Micropeen) provides a safe environment as it prohibits the particles from contaminating the air. Within the SB chamber the sample is clamped between two rotatable plates as can be seen in figure 22(b). One of the rotating plates is attached to an electromotor. The SB beam is aimed at the rotating cylinder at a distance of approximately 0.15 m.

3.2.2 Chemical etching

As mentioned before, the following etchants are used:

- CE1 : 50 mL H_2O , 25 mL HNO_3 , 5 mL HF , 2 minutes in ultrasonic bath.
- CE2 : 50 mL H_2O , 25 mL H_2SO_4 , 25 mL HCl , 60 minutes in ultrasonic bath.

Note here that CE1 is a relatively strong etchant used for a short period of time, whereas CE2 is a weaker etchant used for a longer period of time. The hypothesis of using CE2 for a longer time period is that it has more time to properly reach the core of the samples. It was observed by Ahmadi *et al* [4] that CE1 had limited effect on the core of the sample.

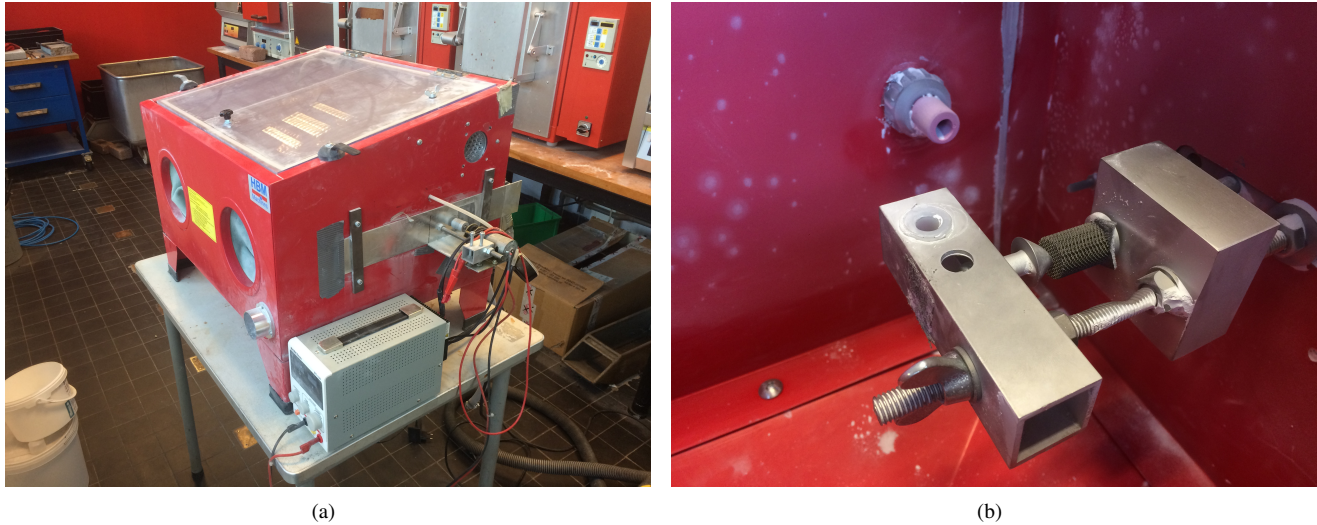


Figure 22. Figures regarding : (a) and (b)

The etching was performed in a fume hood whereby the samples were placed in a beaker with the etchant solution. This beaker was placed in an ultrasonic cleaner. The ultrasonic cleaner was used because it removes the air bubble stuck in the centre of the lattice samples.

3.2.3 Hot isostatic pressing

HIP was performed by the company 'Bodycote' whereby the titanium samples were placed in a 100 MPa pressurised inert gas environment at 920 °C for 2 hours. The samples were cooled at 10 °C/min.

3.3 Microstructural characterisation

To view the microstructure of the cylindrical samples a Keyence VHX5000 and an Olympus BX60M microscope were used. microscopy samples were cut with a Struers - Secotom-10 and then polished with SiC as ground, and with MD largo 9µm (MD Chem with OPS solution 0.04 µm) for 10 minutes as the finer stage. To reveal the microstructure the sample surfaces were immersed in a 50 ml distilled water, 25 ml HNO₃ and 5 ml HF solution for 12 seconds. The samples shown in figure 36 were cut parallel to the top surface and through the geometric centre of the sample (figure 23(a)). The samples shown in figure 37 were cut in an 37.5° angle to show the microstructure in the build direction (figure 23(b)).

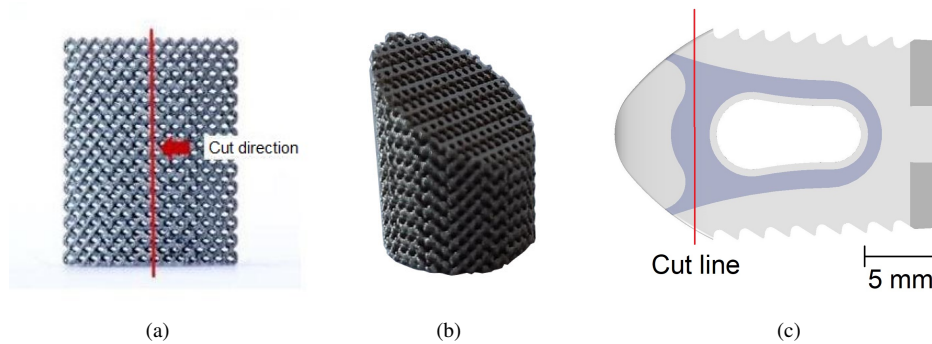


Figure 23. A set of three subfigures on the cuts made for (a) lattice cylindrical samples [8]; (b) lattice cylindrical samples 37.5 ° (c) and implant samples

An analyses of the strut thickness was performed on several sample groups mentioned in table 5. For the measurement a

JOEL, JSM-6500F (Japan) SEM was used. The same microscope was used to visualise the effect of the surface modifications on the surface roughness.

For obtaining the strut thickness the samples were cut parallel to the top surface through the geometric centre of the sample using the Struers - Secotom-10 cutting device as is shown in figure 23(a). The exposed struts, when looking in the opposite direction of the build direction, were covered in partially molten particles to the surface. When looking in the build direction this phenomenon was observed to be substantially less. Due to gravity the partially molten surface particle on top of the strut attach to the melt, whereas the surface particles on the bottom of a strut fall down. For improved visibility the choice was made to measure the strut thickness looking from the build direction on the bottom of the strut.

To view the microstructure of the implants an identical sample preparation was performed as for the cylindrical samples. The cuts were made as is shown in figure 23(c). The microstructure was observed using the Olympus BX60M microscope. To view the effect of the surface modifications the JSM-6500F (Japan) SEM was used.

To observe the grain growth direction of continuous and pulsed SLM samples, electron backscatter diffraction (EBSD) images were created. A square sample was used so that the strut aligned with the build direction (figure 24(a)). The sample was observed in the build direction. the grains were observed in the area as indicated in figure 24(b) for the continuous SLM and in figure 24(c) for the pulsed SLM.

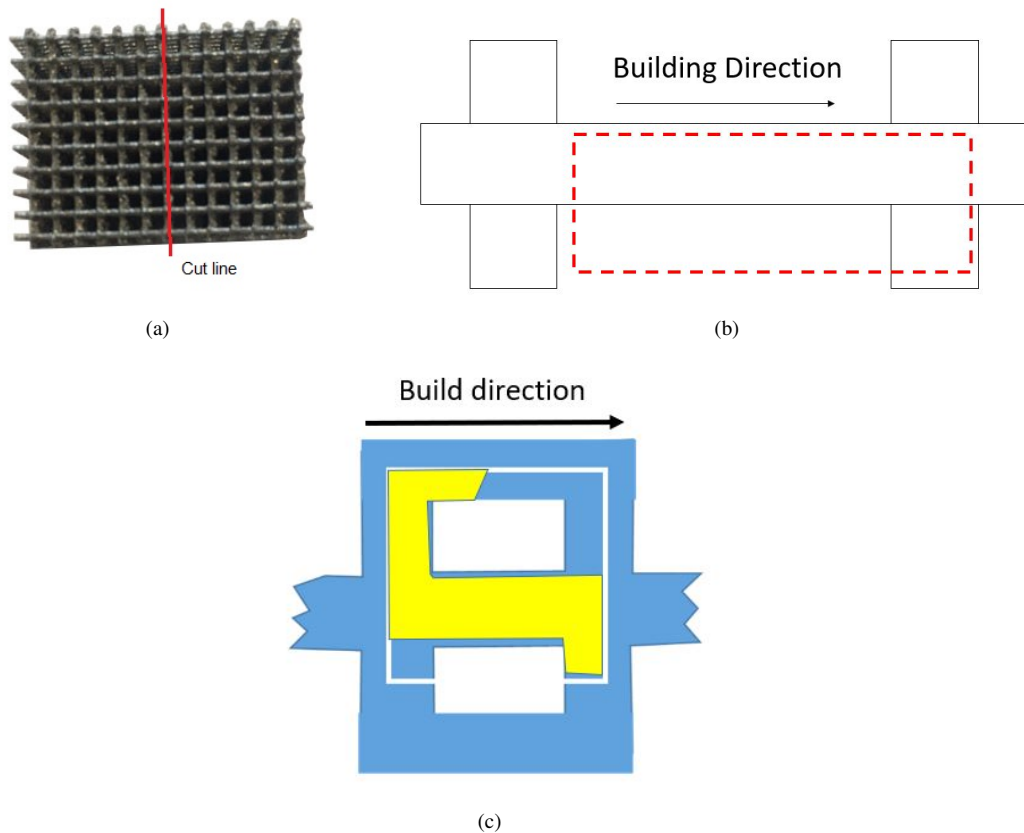


Figure 24. Two figures regarding the (a) square unit cell Ti6Al4V samples to observe preferential grain growth; (b) location of EBSD observation continuous SLM sample (- -). (c) location of EBSD observation pulsed SLM sample (■)

3.4 Mechanical testing of cylindrical samples

Mechanical compression testing was performed on Ti6Al4V SLM cylindrical samples according to ISO 13314. The goal was to determine the mechanical properties of the Ti6Al4V lattice structured metamaterials and the effect of heat treatments and surface modifications on the mechanical properties.

3.4.1 Static compression testing of cylindrical samples

All compression tests were performed on the Zwick Z100 tensile tester (figure 25(a)) using a 80 kN load cell. The compression tests were performed according to the ISO 13314:2011 [12] standard. A strain rate of 1.8 mm/min was applied to the cylindrical samples. The end of test criteria was either 60 % deformation or 50 kN maximum load. The used set-up is shown in figure 25. The compression fixture plates were placed horizontally and were prohibited from tilting. Furthermore no lubricant was applied on the sample to machine plate interface.

The mean static compression graphs are constructed by dividing the sum of each samples stress level by the amount of samples. This was done for every strain level with a strain increment of 10^{-4} (mm/mm). The 95 % confidence interval was determined at each strain point using the following formula:

$$CI = 1.96 \pm \frac{s}{\sqrt{n}} \quad (9)$$

In which s is the standard deviation and n is the amount of samples used. This formula gives an upper and a lower boundary for each data point.

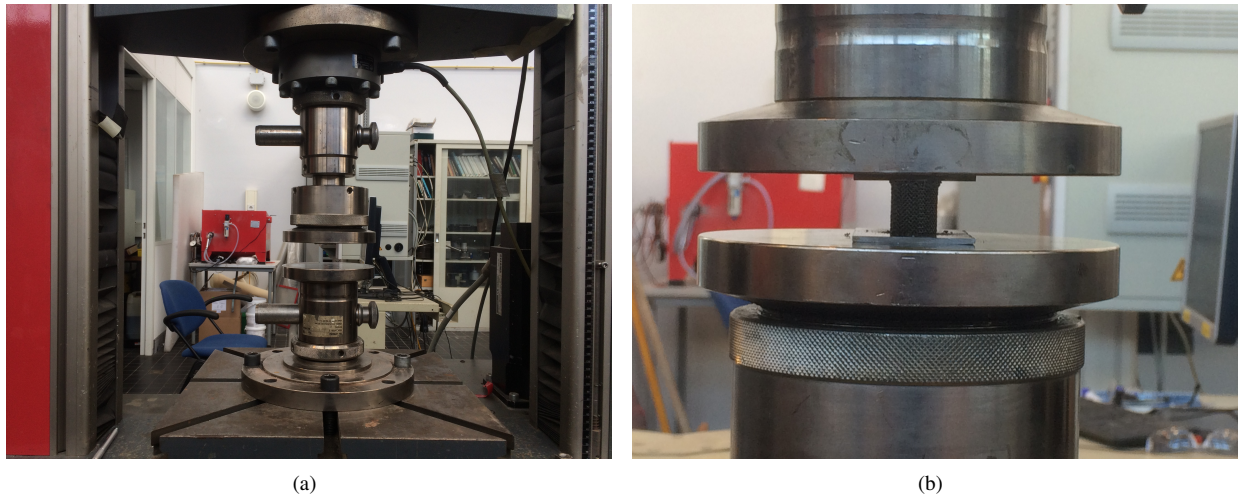


Figure 25. Figures regarding ISO 13314:2011 compression set-up: (a) The Zwick Z100 compression machine ; (b) The sample in compression

3.4.1.1 Normalisation of compression cylindrical samples

The static compression tests on lattice structured cylindrical samples performed by Hooreweder *et al* [22] were normalised by calculating the stress that would be felt if all the samples would have the same relative density of 35 %.

This normalisation is started by measuring the relative density of the actual samples. Then the strut thickness of the samples and the strut thickness of the hypothetical $\rho_{rel} = 35 \%$ was estimated using the following formula:

$$\rho_{rel} = C_1 \left(\frac{r}{L}\right)^2 - C_2 \left(\frac{r}{L}\right)^3 \quad (10)$$

in which C_1 and C_2 are structure type related constants which, in the research by Hooreweder *et al* [22] regarding the diamond

unit cell structure, have been identified as 4.08 and 3.21, respectively. ρ_{rel} is the measured relative density, r is the strut radius and L is the length of the strut.

The effect of strut diameter needs to be related to the stress of the bulk. This is started by looking at the force which is applied on a single strut. This can be calculated by dividing the force on the bulk over the amount of nodes in the cross section. This is done by the following equation:

$$F_{strut} = \frac{F_{tot}}{n \cdot 2} \quad (11)$$

in which F_{tot} is the total force, F_{strut} is the force applied on one strut and n is the number of nodes. Note here that the number of nodes is multiplied by two as the node is connected to two struts, which is only valid for the diamond structure. This F_{strut} is then applied to the strut as is shown in figure 26.

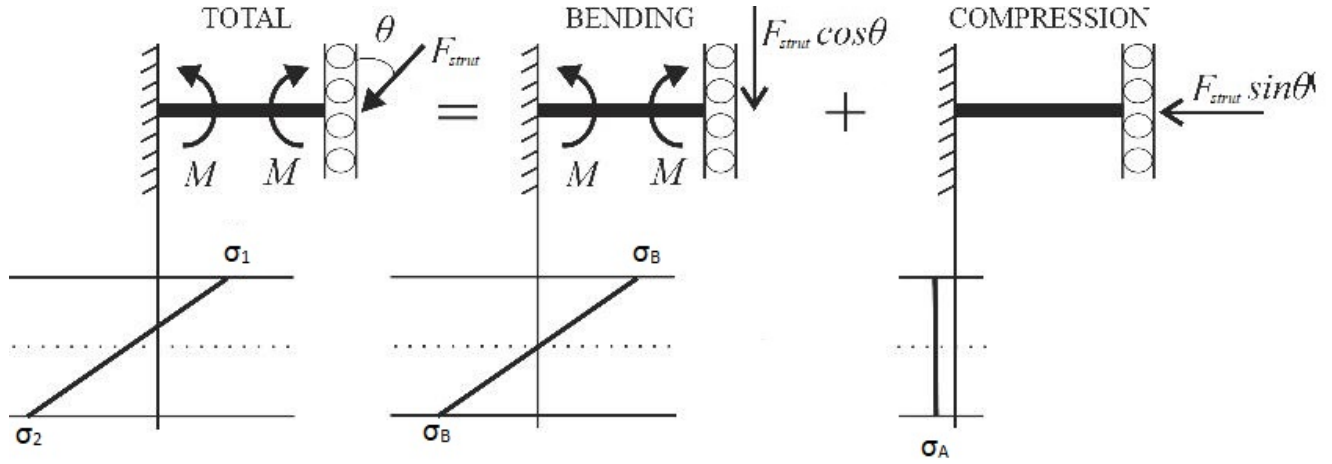


Figure 26. Simplified stress situation at a strut of a diamond unit cell [22]

As can be seen in the figure a local tensile stress σ_1 arises which is the function of the bending moment applied by the vertical element $F \cos(\theta)$ of F_{strut} and the compression of the horizontal element $F \sin(\theta)$ of F_{strut} . This local tensile stress σ_1 is the root cause of failure in compression and compression fatigue. σ_1 can be calculated by the following formula:

$$\sigma_1 = \sigma_B - \sigma_A = F \left(\frac{16L \cos(\theta)}{\pi d^3} - \frac{4 \sin(\theta)}{\pi d^2} \right) = F \cdot C_{sample} \quad (12)$$

where L is the length of a strut, θ is the angle of the strut force (in the case of diamond structure: $\theta = 37.5^\circ$) and d is the strut diameter. Equation (12) is formulated by σ_B and σ_A which are the stresses composed by the bending and compression forces on the strut.

$$\sigma_B = \frac{My}{I} = \frac{FLd \cos(\theta)}{4I}, \text{ where } : I = \frac{\pi d^4}{64} \quad (13)$$

$$\sigma_A = \frac{F \sin(\theta)}{A}, \text{ where } : A = \frac{\pi d^2}{4} \quad (14)$$

Essentially the parameter C_{sample} in equation (12) accounts for the variation in relative density due to difference in strut thickness and structure. For example, as is shown in table 2, the properties of two identically processed AP samples with different relative densities, gives rise to different compression properties. The C_{sample} can be calculated for the actual sample and for the 35 % hypothetical reference $C_{35\%}$ using equation (10) and (12). C_{sample} is used to calculate σ_1 which is the failure

stress. Then σ_1 is used with $C_{35\%}$ in equation (12) to calculate the hypothetical F_{strut} . This is then again used to calculate the stress at which the sample would fail if it were to have a 35% relative density using equation (11). This model however does not account for geometric discrepancies, internal material porosity, non-uniform cross sections of the struts, surface roughness, residual stress and stress concentrations in nodes. Theoretically the effect of heat treatments can be seen accurately using this normalisation model, as it enables the ability to compare samples as if they had the same relative densities. This model will be applied to normalise the current research compression tests.

3.4.2 Fatigue testing of cylindrical samples

The compression fatigue tests were conducted using the MTS 858 machine (Figure 27) with a 100 kN load cell. The loads were applied at a rate of 15 Hz with an R ratio of 0.1. The compression fatigue experiments were conducted on 8 different stress levels for each sample group to create an S-N curve. An end of test criteria was applied of either 4 mm crosshead displacement or a run out fatigue life of 1,000,000 cycles.

The S-N curve powerlaws were determined using the 'nlnfit' function in Matlab. Furthermore the 90 % confidence interval was calculated using the 'nlpredci' function. The 90 % confidence interval was determined using simultaneous bounds. This means the function accounts for scatter variation throughout the curve.

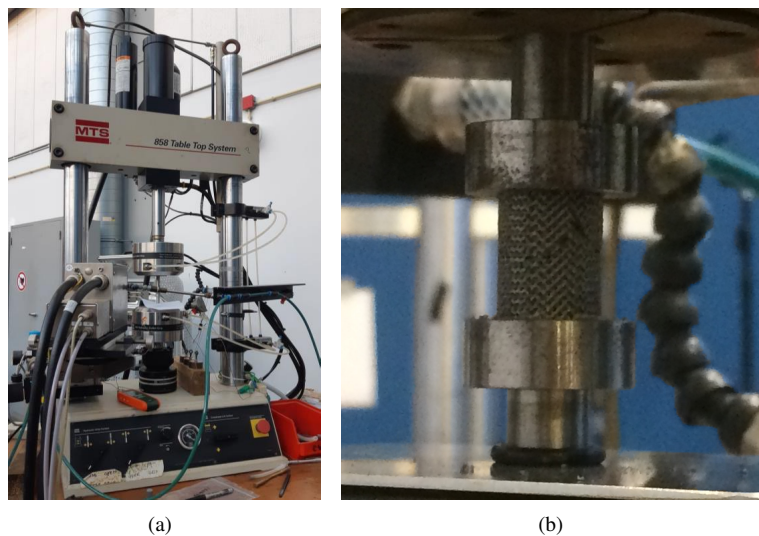


Figure 27. Figures regarding cylinder compression fatigue: (a) MTS 858 fatigue machine; (b) sample compression fatigue

3.4.2.1 Normalisation of compression fatigue cylindrical samples

As is mentioned before the usual way of normalisation is to normalise against the yield strength. Hooreweder *et al* [22] performed compression fatigue tests on continuous SLM samples, where a new method of S-N curve normalisation was presented. As is shown in section 3.4.1.1 the stress felt by a single strut represented by σ_1 can be calculated by using equations (10) and (12). By plotting the S-N curve to this σ_1 value instead of to the stress on the bulk, the effect of strut thickness can be eliminated. Note here that this comparison can then only be made for two samples with the same unit cell. Figure 28(a) shows the S-N curve plotted for the calculated local maximum stress at the strut and the fatigue resistance in terms of number of cycles. The two AP samples with different strut thicknesses have almost identical curve fitting when they are plotted to maximum local stress σ_1 , whereas when they are plotted against the global stress they differ significantly (figure 28(b)). Furthermore when comparing the HIP and HIP+CE groups a clear increase in fatigue resistance can now be seen when the chemical etching was applied. This model will be applied to normalise compression fatigue tests of the current research.

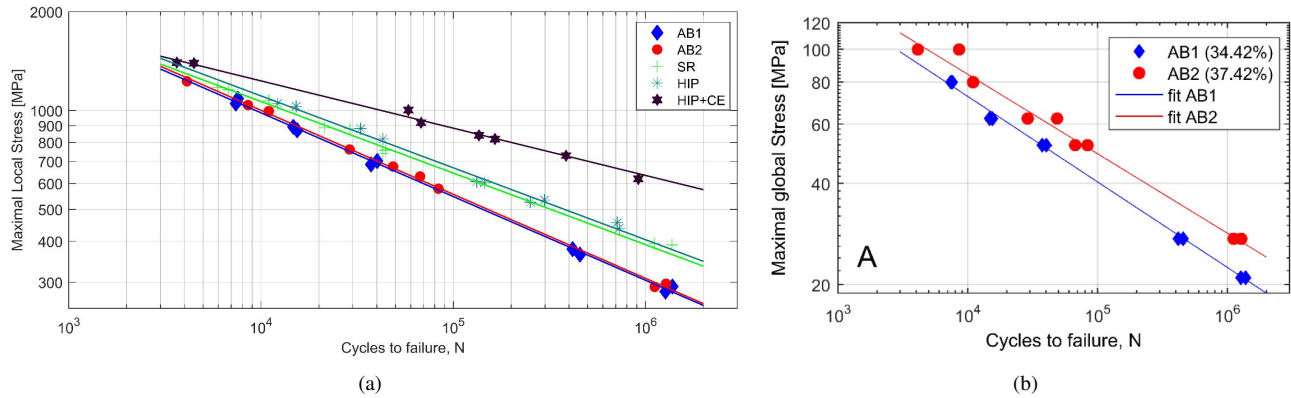


Figure 28. A set of two subfigures on fatigue : (a) S-N curve on the maximal local stress; (b) S-N curve on the maximal global stress [22]

3.5 Mechanical testing of spinal cage implants

Mechanical tests were performed on spinal cage implants to assess the mechanical behaviour of the Ti6Al4V lattice structures in its intended application. The tests were performed and designed according to ASTM F2077.

3.5.1 Implant and fixture design

The implant used for mechanical testing is shown in figure 21(a). The spinal cage is a stand-alone cage to be applied for the lumbar section of the spine. The cage in its current shape is designed for the human body situation where the gap between vertebra is unusually large. Figure 29(a) displays the basic dimensions of the lumbar spinal cage implant.

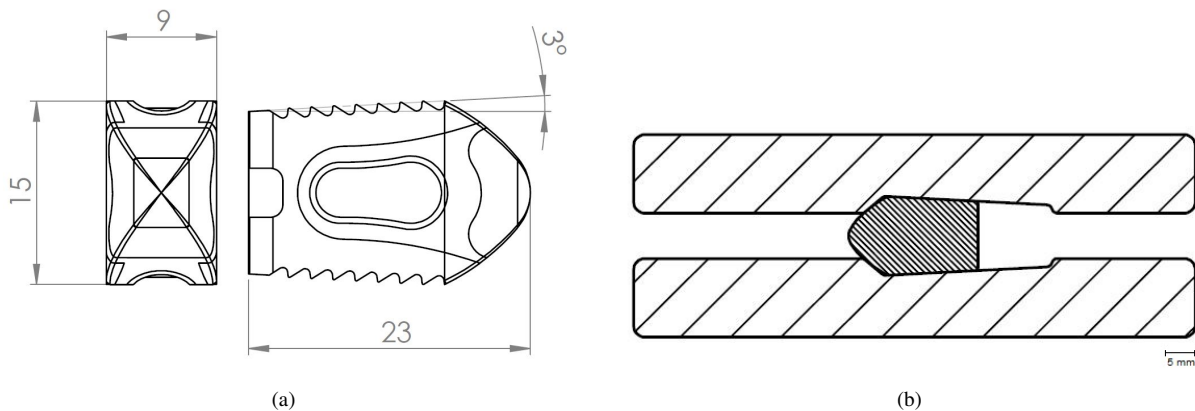


Figure 29. Figures regarding the spinal cage implant: (a) Dimensions Spinal cage implant (mm) ; (b) Schematic of the interface between implant and blocks

For testing according to ASTM F2077 a specific type of fixture needed to be created. Figure 30 displays the fixture in parts and figure 32(a) displays the assembled fixture in the static compression testing mode. The parts were created according to the requirements discussed in section 2.5.2. The pushrod (figure 30(a)) and the minimal friction sphere (figure 30(b)) were manufactured using a lathe, whereby the holes were drilled afterwards. The steel blocks (figure 30(d)) were manufactured using CNC milling and the ball and socket joint (figure 30(c)) was a standard part. The pushrod, minimal friction sphere and the steel blocks were post processed using heat treatment to supply these parts with the required ultimate tensile strength of at least 1310 MPa. The steel blocks as well as the Polyoxymethylene (POM) blocks were manufactured so that they matched the outer contour of the implant (figure 29(b)). Furthermore the centre of the implant can be placed exactly in the centre of

the plate due to the shape match. Therefore the force will be aimed at the geometrical centre of the implant. As can be seen in figure 29(b), the sample is caged in. This was done to avoid the sample from gradually moving out of place due to cyclic loading during the fatigue test.

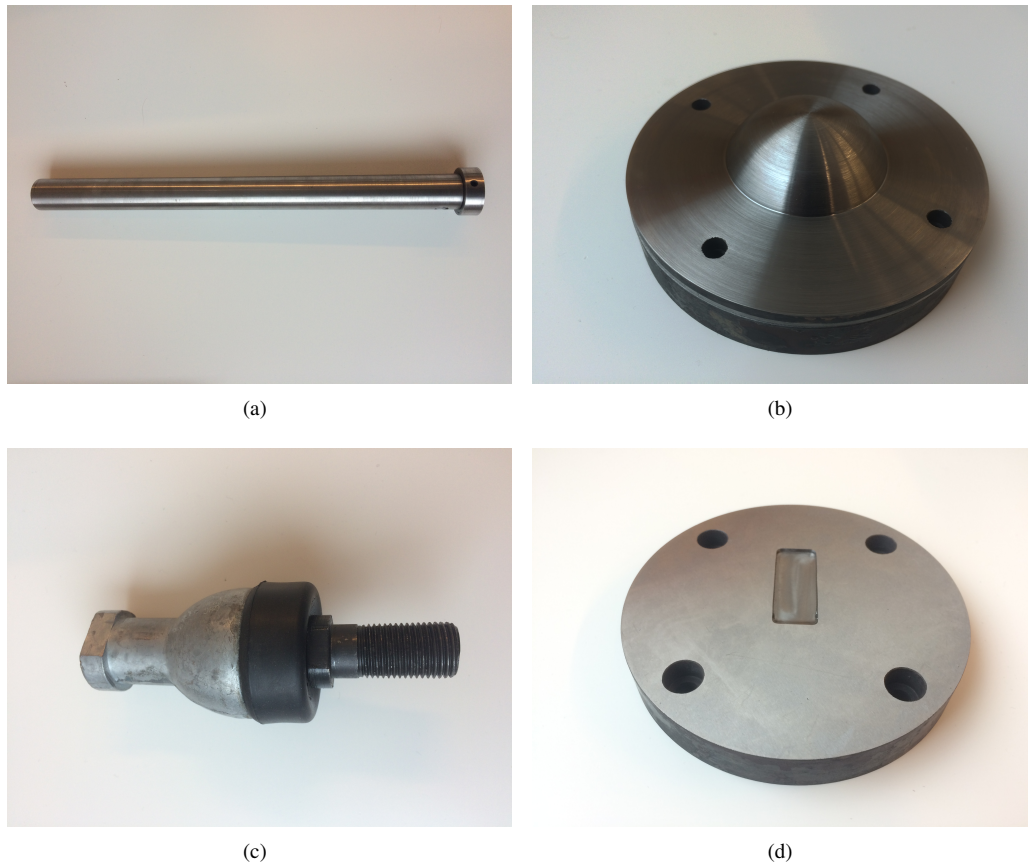


Figure 30. A set of four subfigures on parts of the ASTM F2077 set-up : (a) Pushrod; (b) minimal friction sphere; (c) ball and socket joint; and, (d) steel block.

Because the set-up was never tested before a polycarbonate (PC) tube was used to assure safety (figure 32(a)). Another issue regarding the set-up was that a possible momentum was induced on the load cell if the pushrod were to move out of centre due to out of axis deformation of the implant. If a large enough moment is induced on the load cell the results will be distorted and furthermore the loadcell can break. Therefore the calculation was performed in figure 31.

Here it is shown that if a force of 20kN is induced in combination with an out of axis deformation of 5mm, the horizontal force component at the ball and socket joint will be a mere 0.297 kN and the moment on the loadcell will be 29.7 Nm. This was found to be insignificant and testing could initiate.

When measuring the deformation and stiffness of the sample during a static compression test using the crosshead displacement, the machine output values are not the real displacement occurring locally at the implant. The machine output values will be the deformation of the entire fixture in addition to the sample. Therefore the stiffness of the fixture without a sample was measured and the values obtained could be subtracted from the machine output values whereby the difference is the displacement occurring at the sample. Furthermore extensometers were added to the set-up (figure 32(b)) to reduce section size of the measured deformation which in turn reduced the amount of deformation and increases the accuracy. Using these measures an accurate representation of the stiffness and the deformation could be obtained of the implant. A stiffness of $355 \cdot 10^3 \pm 47 \cdot 10^3$ N/mm needs to be subtracted from the implant stiffness results to provide an accurate measurement.

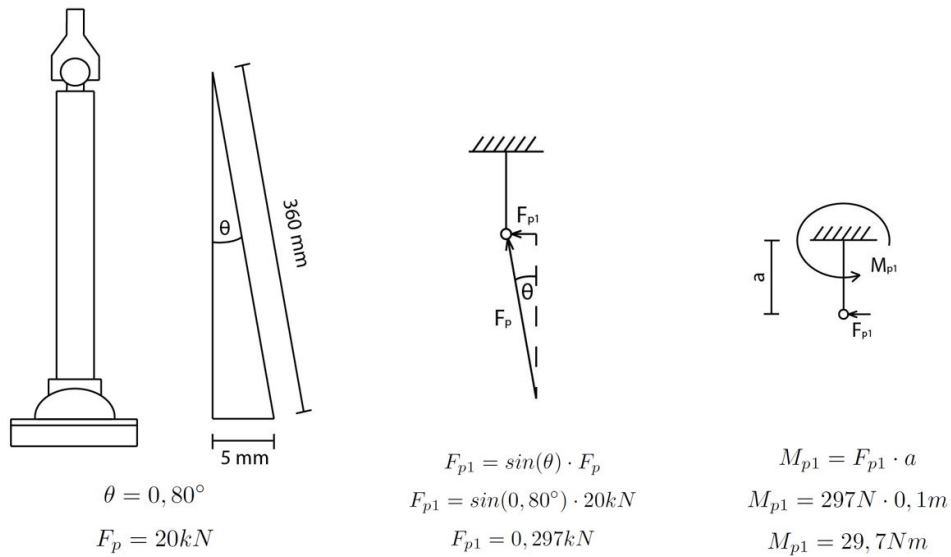


Figure 31. Example equation to show momentum is low due to length of the pushrod

3.5.2 Static compression testing of implants

Static compression tests were performed according to ASTM F2077 on implants described in section 3.5.1. The set-up described in section 3.5.1 was used for the static compression test (figure 32). Compression was displacement controlled with a speed of 1.8 mm/min. The end of test criterias were set to either 2 mm displacement, 25 kN force or a rapid reduction in force of 30 % within a time frame. in reality the latter was always the critical factor, meaning the test stopped after the first collapse of the structure. For these compression tests the Zwick Z250 machine was used with a load cell of 250 kN

The 95 % confidence interval for the mean static compression graphs was determined the same way as described in section 3.4.1 using equation 9.

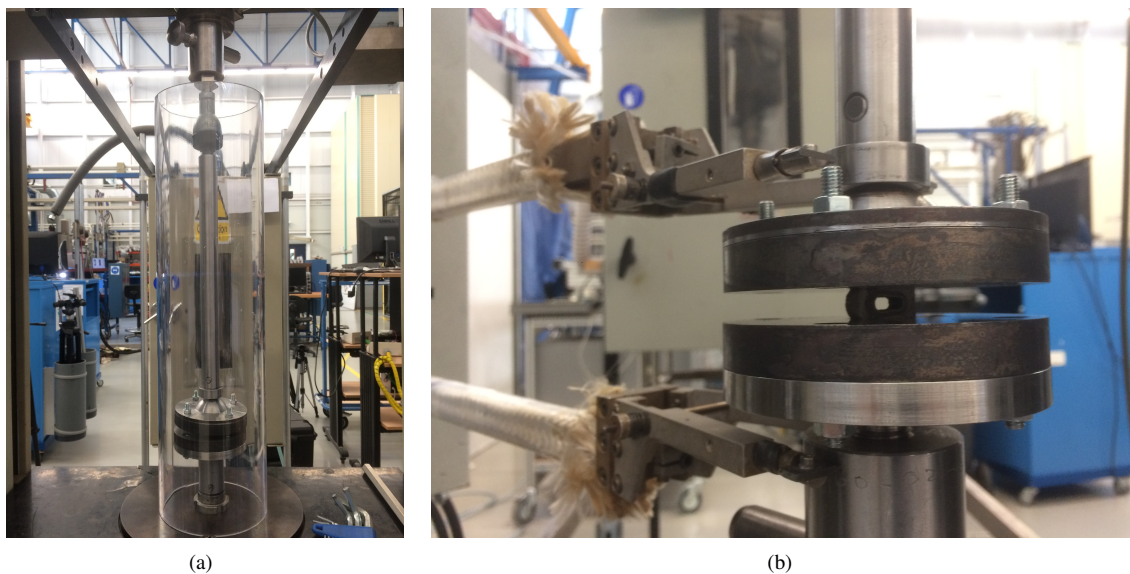


Figure 32. Figures regarding implant compression: (a) ASTM F2077 compression set-up ; (b) sample in compression

3.5.3 Fatigue testing of implants

Compression fatigue tests were performed according to ASTM F2077 on implants described in section 3.5.1. The tests were conducted with a frequency of 10 Hz to prevent potential heating effects at higher frequencies. An R-ratio of 0.1 was used for the all tests. In total 8 samples were tested divided over 3 force levels to create an F-N curve. End of test criteria were 2 mm displacement or 5.000.000 cycle run-out. The set-up used for testing is described in section 3.5.1 and can be seen in figure 33. The difference in set-up compared with the static compression test is that in this case the blocks are made out of POM (Polyoxymethylene). All tests were done on the MTS 810 fatigue tester.

The 90 % confidence interval was calculated as described in section 3.4.2 using 'nlinfit' and 'nlpredci' in Matlab.

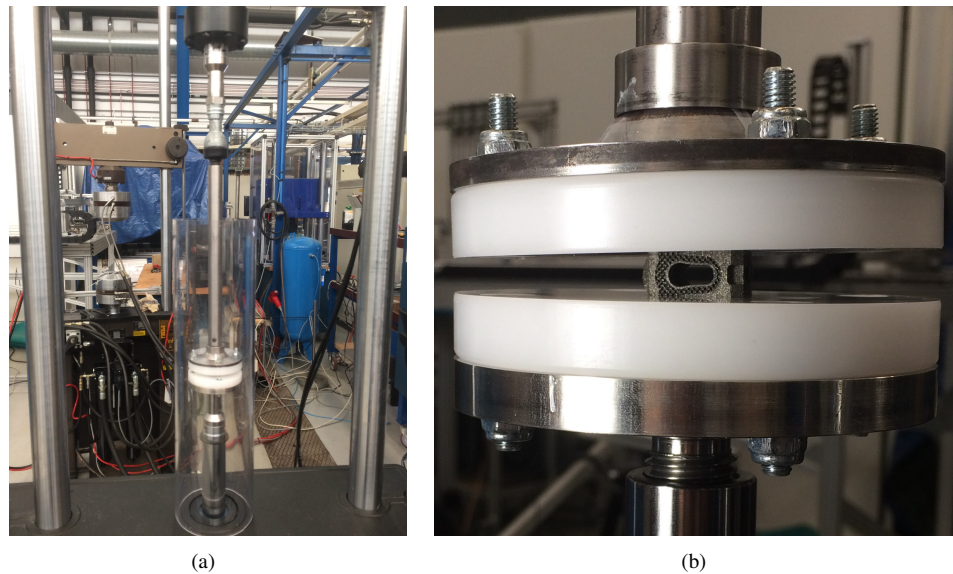


Figure 33. Figures regarding implant compression fatigue: (a) ASTM F2077 fatigue set-up ; (b) sample in compression fatigue

3.6 Wettability study

Sandblasting and chemical etching were applied to the lattice structured samples in order to improve the mechanical properties of the samples. In this section the possible side effects in terms of change in wettability behaviour will be discovered.

3.6.1 Sessile drop test

To quantify the amount of wettability which occurs due to different surface modifications, a Sessile drop test was performed whereby the contact angle of deionised water was measured. For the Sessile drop test the cylindrical samples shown in figure 21(c) were used which were subjected to the treatments described in section 3.1.3. For the wettability a Theta Lite Optical Tensiometer (figure 34(a)) was used to determine the contact angle. The contact angle was measured versus the tangent of the cylinder which the software could detect automatically. For each sample type the contact angle was measured at eight different locations on the cylinder. A droplet of 3 μ l was placed on the surface whereby the average CA was measured for 10 seconds. The average was taken from both the left and the right side of the droplet. All cylindrical samples were ultrasonically cleaned for 20 minutes with isopropanol and for 10 minutes with demi water after which they were inserted in the vacuum desiccator up to 10^{-1} mbar. After vacuum desiccator the samples were rested in regular desiccator for 12 hours.

To analyse the contact angle results, ANOVA (analyses of variance) and Tukey's test were applied. The ANOVA test uses the mean of the differences between groups and the mean of the difference within a group to calculate a ratio. If the differences between groups are large and the differences within a group are small there is a large probability that the groups are in fact different. This is quantified by the p-value and if $p < 0.05$ the groups are found to be different. Tukey's test compares the means

of two groups with an accuracy parameter determined using the standard error and the amount of samples. Hence the outcome of Tukey's test shows if there is a statistical difference between each individual group.

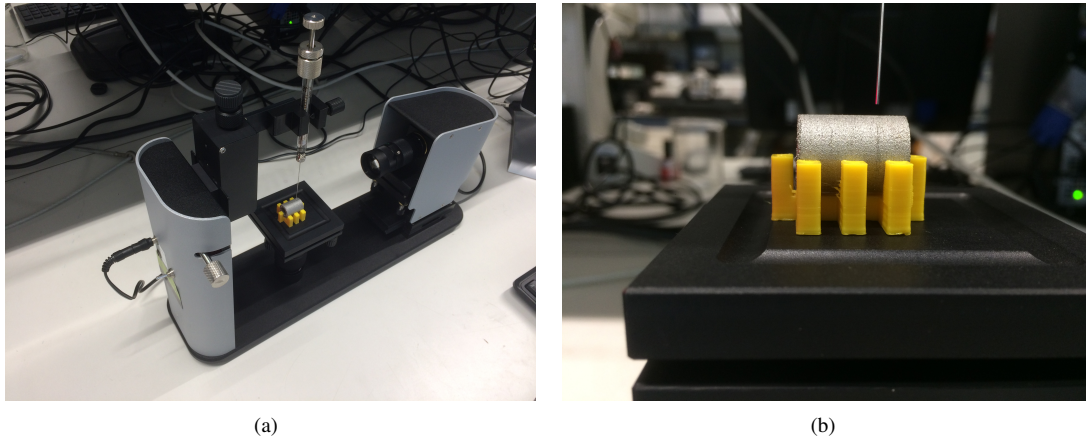


Figure 34. Figures regarding (a) optical tensiometer set-up (b) 3D printed sample holder to keep sample aligned for drop test

3.6.2 Dip test

To visualise the effect of surface modifications on wettability behaviour, a dip test was developed. With the dip test a sample is dipped into coloured water with a speed of 1.25 mm/s. After the surface of the water is breached, the movement is stopped and the sample is kept stationary for 1 minute. When contact is made with the water and if the sample is highly hydrophilic, the water will flow upwards into the lattice structure. If the sample is hydrophobic the water will not enter the sample and the contact angle with the water surface will be large. If the sample is moderately hydrophilic the water may not reach the top of the sample in 1 minute. If the sample is only hydrophilic for a small amount a contact angle will be below 90 degrees but water may not be able to move upwards due to stronger gravitation.

For this experiment a set-up was created using Arduino, Arduino software, 3D printed PLA linear actuator and a mini servo motor (figure 35). With this set-up the linear actuator can be controlled in speed and positioning. The liquid used for the test is demi water with an addition of some colouring to enhance the visibility of the effects.

The samples used for this experiment are described in section 3.1.3. All cylindrical samples were ultrasonically cleaned for 20 minutes with isopropanol and for 10 minutes with demi water after which they were inserted in a vacuum desiccator up to 10^{-1} mbar.

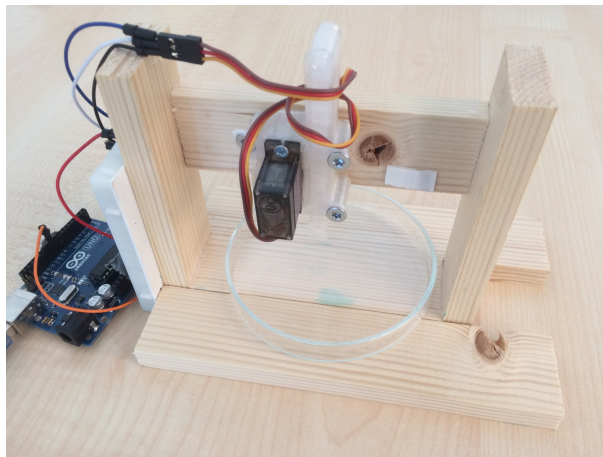


Figure 35. Set-up Dip test

4 Results

In this section the obtained experimental results will be discussed. Again the distinction is made between the cylinder mechanical testing results, the implant mechanical testing results and the wettability testing results.

4.1 Microstructural characterisation cylindrical samples

To better understand the results which will be obtained from the mechanical tests and wettability study, a characterisation of the SLM manufactured metamaterial Ti6Al4V is required.

The microstructure of the AP samples for both continuous SLM and pulsed SLM consist of fine martensitic laths (figure 36(a), 36(c)). These laths are interpreted to have the hexagonal α' martensite structure (also observed in figure 6). This structure is obtained due to the rapid cooling rate in the order 10^4 to 10^6 K/s, which occurs in the manufacturing process [41, 42]. By heat treatment the α' martensite structure is transformed to a combination of α and β grains as can be seen in figure 36(b) and figure 36(d).

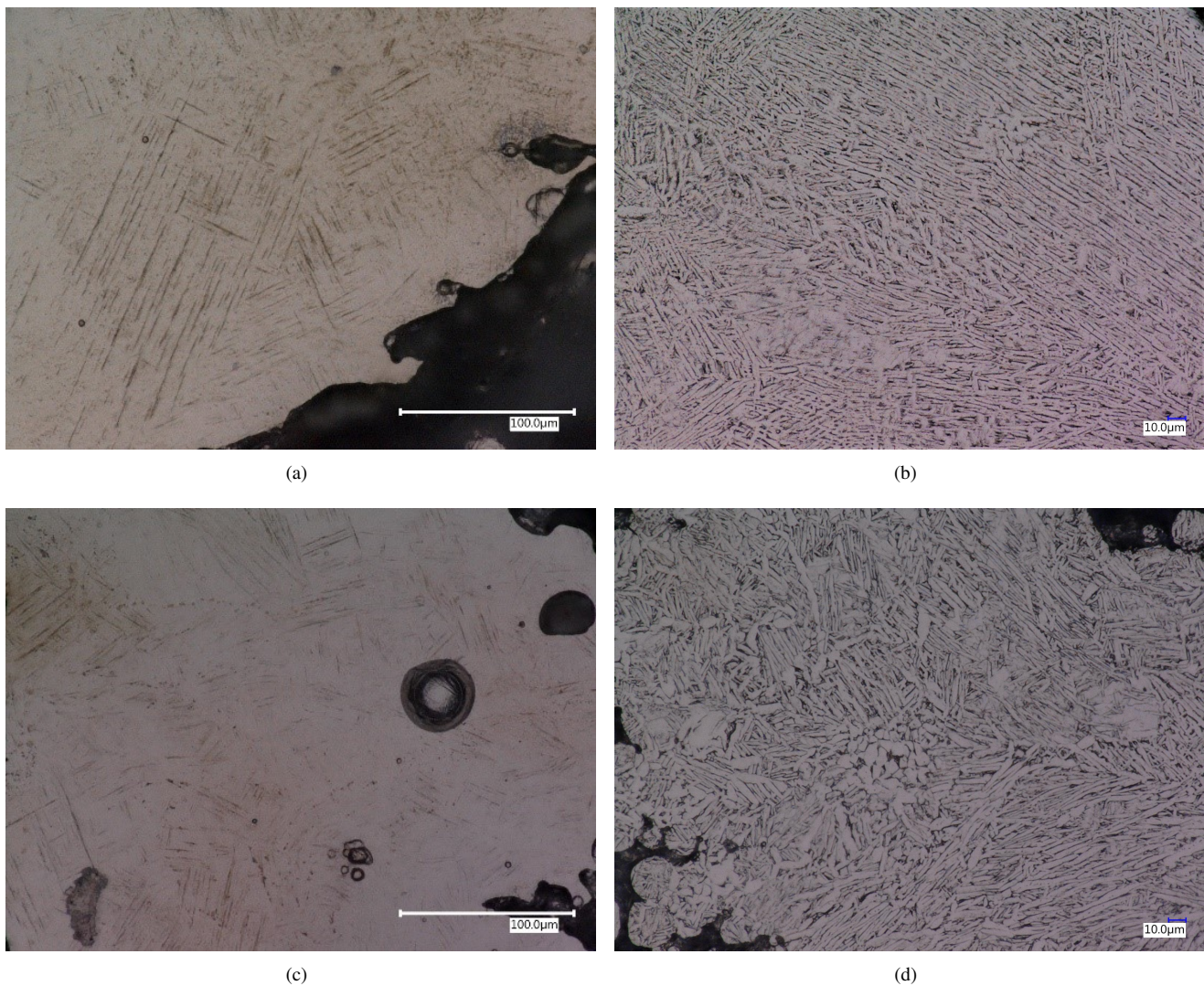


Figure 36. A set of four subfigures on the microstructure of: (a) AP Continuous SLM; (b) HIP Continuous SLM; (c) AP Pulsed SLM; and, (d) HIP Pulsed SLM.

After HIP treatment the size of the laths was found to be finer for the continuous SLM samples as compared with the pulsed

SLM samples (figure 36(b) and figure 36(d)). A measurement was performed determining the α lath width at 18 randomly picked laths for both continuous and pulsed SLM. For continuous SLM HIP the average lath width was $2.6 \pm 0.6 \mu\text{m}$, whereas for the pulsed SLM HIP samples a lath width of $4.6 \pm 0.7 \mu\text{m}$ was measured. This means the continuous SLM samples have larger grain boundary density which in turn leads to improved mechanical properties. This is in line with what is reported in literature ([4], [22]).

Figure 37(a) shows a microstructural image of a continuous SLM AP sample cut in 37.5° angle. By cutting in this angle the microstructure can be observed in the direction of the struts. In figure 37(a) it can be observed that for the continuous SLM AP samples there is a preferential grain growth in the direction of the strut which is in line with what was observed by Ravi *et al* [16]. This could potentially indicate some anisotropy at the macroscale in mechanical behaviour. For the pulsed SLM samples this preference was not observed (figure 37(b))



(a)



(b)

Figure 37. Figures regarding samples cut in 37.5° showing: (a) the preferential grain growth of continuous SLM and (b) the more random grain growth of pulsed SLM samples

EBSD was performed as described in section 3.3 to determine the preferential grain growth direction of continuous SLM. Using EBSD imaging it was confirmed that preferential grain growth of the prior β -grains in the build direction occurs for the continuous SLM method (figure 39(a)). The prior β grains form a pillar (or columnar) like shape aimed in the build direction.

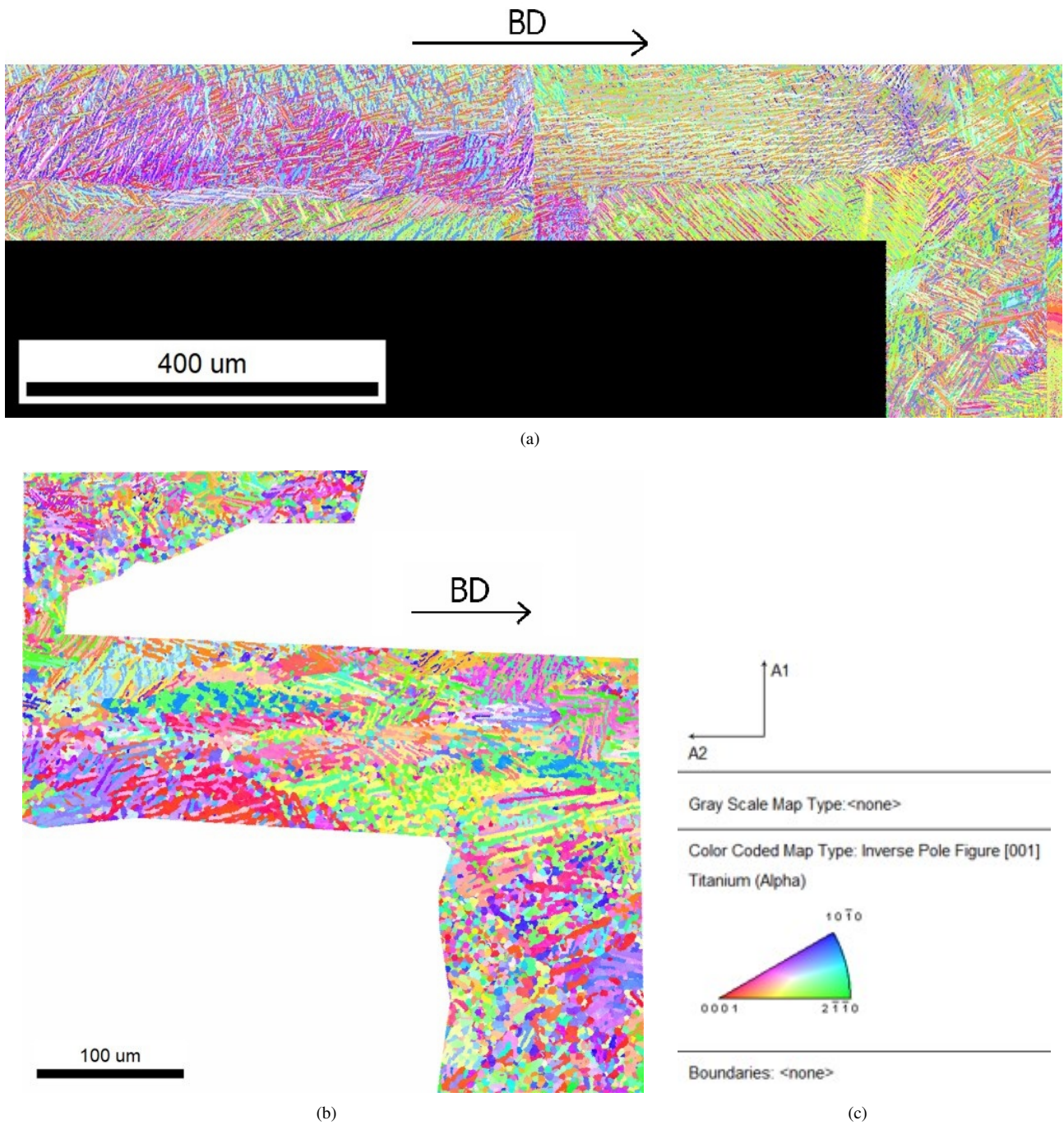
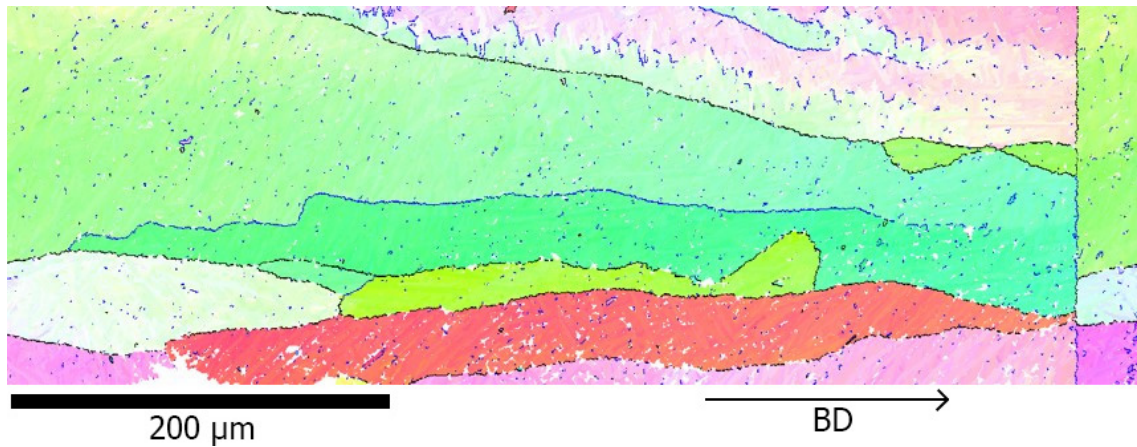


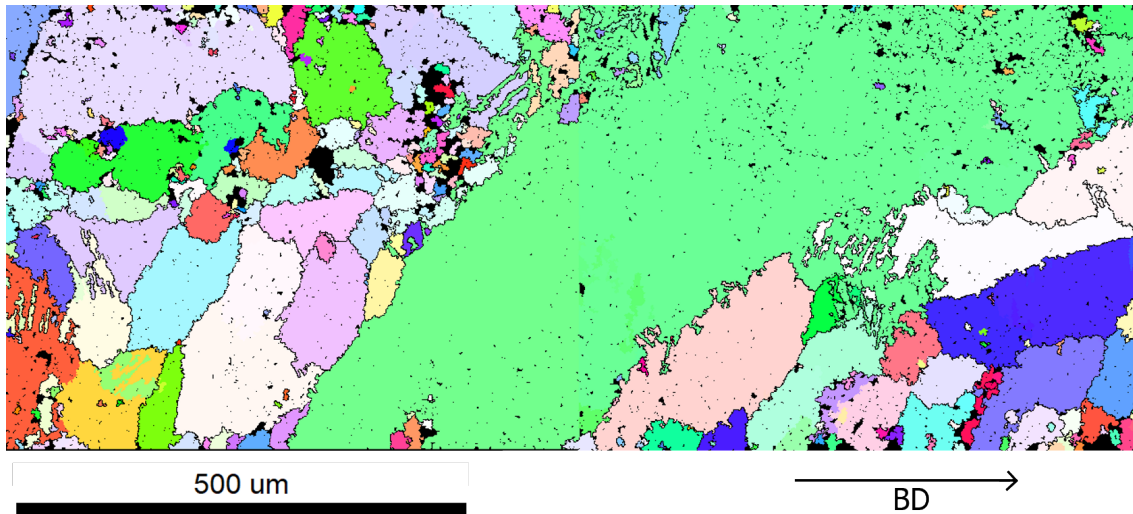
Figure 38. EBSD images of: (a) Continuous and (b) Pulsed SLM showing α' grain orientation (c) Colour coded map for Inverse Pole Figure (IPF) of Alpha Titanium

For the pulsed SLM approach no preferential grain growth direction was observed as compared to the continuous SLM approach (figure 39(b)). The grains have a more randomly oriented grain shape. This means that the pulsed SLM approach has a more isotropic structure when compared to the continuous SLM. This is in line with the what was observed in figure 37.

Furthermore, as can be seen from Figure 39, grain size for pulsed SLM seem to be larger as compared to continuous SLM, which is in line with HIP difference previous observed. A more quantify measure of the grain size for both SLM methods should be the scope of the follow up work.



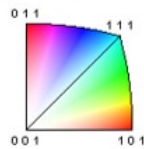
(a)



(b)

Color Coded Map Type: Inverse Pole Figure [100]

Titanium (Beta)



Boundaries: Rotation Angle

Min	Max	Fraction	Number	Length
15°	65°	0.871	109445	3.16 cm

(c)

Figure 39. Reconstruction of Beta phase in [100] IPF representation for (a) continuous SLM (b) pulsed SLM (c) Color Coded Map for Inverse Pole Figure of [100] Beta Titanium

A Struers Dura Scan Vickers hardness machine was used to measure the microhardness on the cross section of polished specimens of each sample group described in section 3.1.1. A series of 10 measurements were carried for each specimen and a load of 0.3 kgf was used. In figure 40 the results are shown. As can be seen the decrease in hardness from AP to the HIP samples indicates an increase in ductility due to the phase transformation from α' -phase to $\alpha + \beta$ -phase.

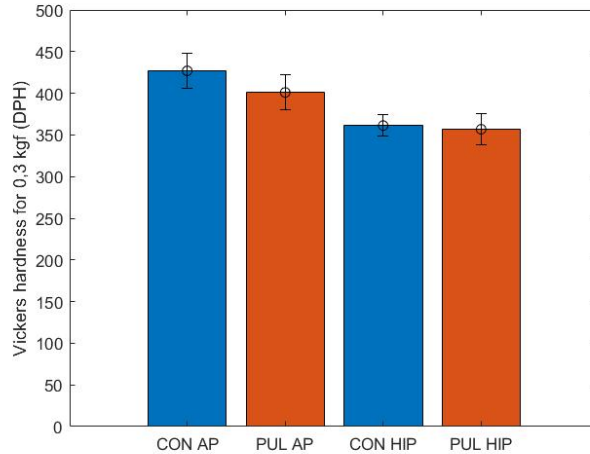


Figure 40. Effect HIP on Vickers hardness (continuous SLM (CON) vs pulsed SLM (PUL))

A Keyence VHX5000 microscope was used to measure the internal porosity of continuous and pulsed AP samples compared with continuous and pulsed HIP samples. The measurements were performed by dividing the porosity area over the total area the strut cross section.

Figure 41 shows the effect of HIP treatment on pulsed SLM samples compared with continuous SLM samples. As can be seen the effect on reduction of pulsed SLM samples is larger, which is due to the higher content of porosity in the first place.

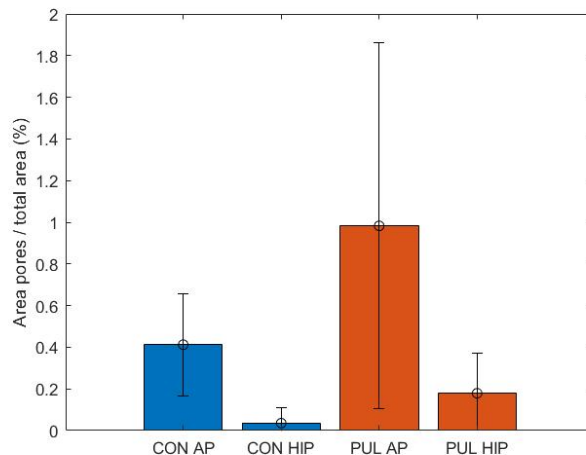


Figure 41. Effect HIP on porosity percentage for continuous SLM samples (CON) and pulsed SLM samples (PUL)

Strut thickness measurements were performed in order to determine the abrasive effect of SB and CE. For each strut the thickness was measured at six to eight different cross sections. The average thickness of each strut was then plotted as a function of distance from the surface. Figure 42 shows the difference between the continuous and the pulsed SLM samples. As The two samples were created in two different relative densities this make sense.

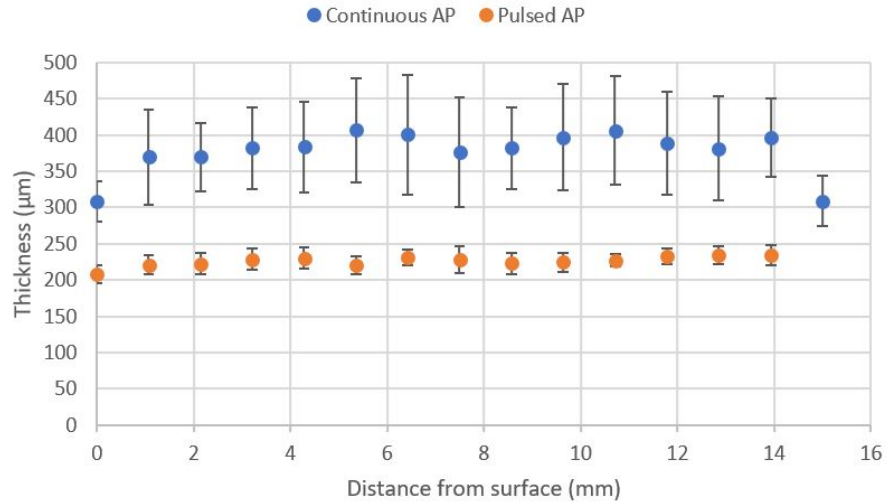


Figure 42. Comparison of the measured strut thickness for the AP continuous SLM samples and the pulsed SLM samples.

To compare the effect of sandblasting and chemical etching on the strut thickness another measurement was performed on the relevant samples (figure 43). What can mainly be seen is that this method of determining the strut thickness is not very accurate. Though in all the samples a slight increasing strut thickness is observed moving towards the centre of the samples. With sandblasting in particular the outside strut gets reduced more than compared with the inner struts.

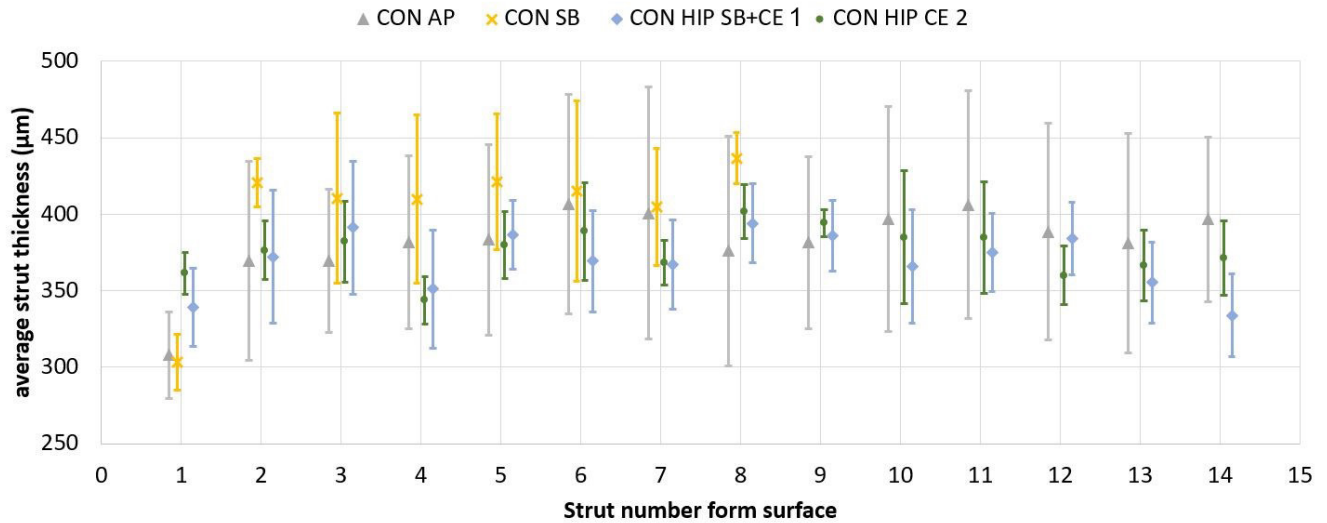


Figure 43. Comparison of measured strut thickness of the following samples: AP, AP SB, HIP CE1 and HIP SB+CE2 (For the x-axis the data points are all shifted slightly around the whole number)

The results shown in figure 43 correspond with what can be seen through the SEM (figure 44). Here it can be observed the particles stuck to the surface are all removed at the surface strut for both SB and CE, however the middle is not reached as thoroughly. The middle is reached best with the combination of sandblasting and chemical etching. This might also be because the etchant method has changed between the two groups. The etching time of one hour leaves more time for the etchant to reach the core of the sample and air has more time to move out of the lattice structure.

The average measured strut thickness was also obtained (table 5). The measurements were performed on six lines on one strut. Then the average strut size was taken over all the struts in one diagonal of the cross section.

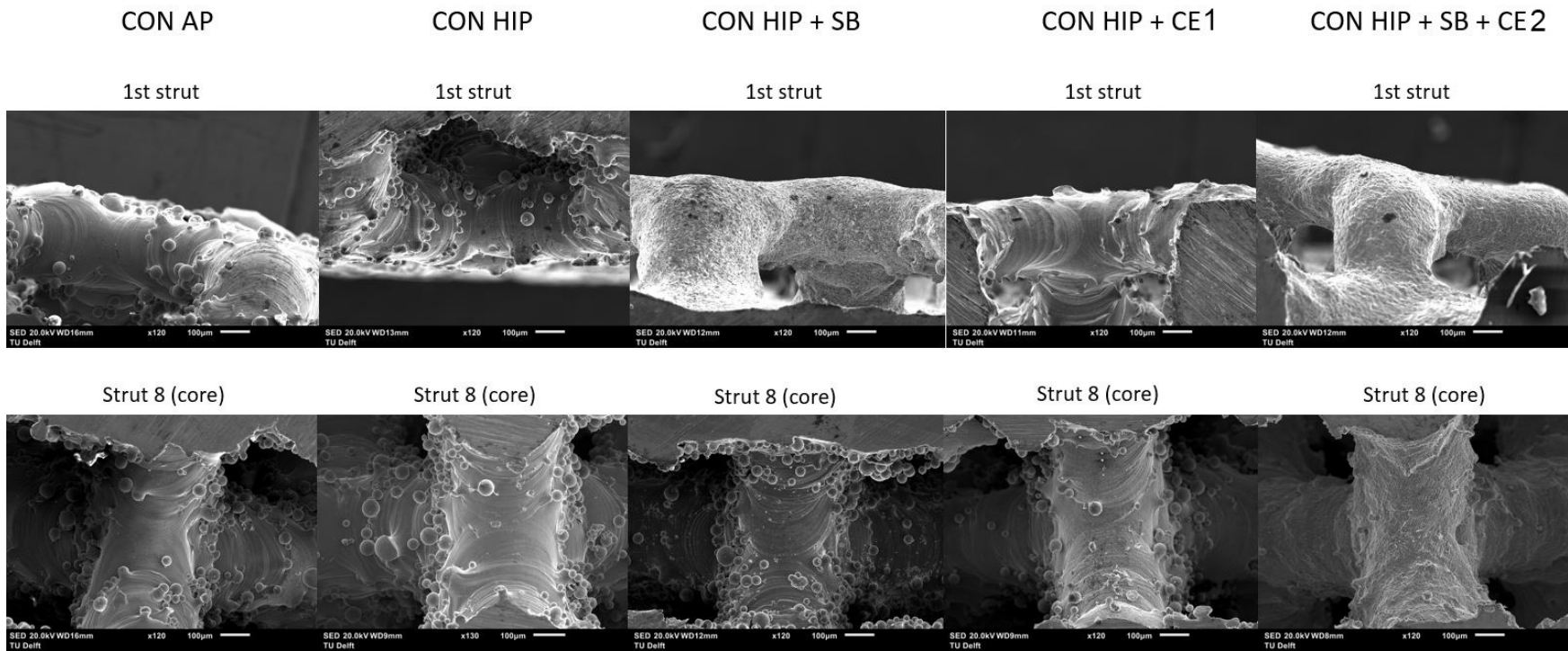


Figure 44. SEM images on the effect of surface modifications for continuous SLM samples

SEM images were taken of HIP, HIP CE1, HIP SB and HIP SBCE2 samples on the change in roughness (figure 45). These images are all taken from the continuous SLM sample batches. What can be seen is that the SB treatment highly influences the surface roughness whereas CE1 only mildly changes the surface roughness. The combined effect of SB and CE2 seems to show that the CE2 treatment does not decrease the effect of SB significantly in terms of visible surface structure.

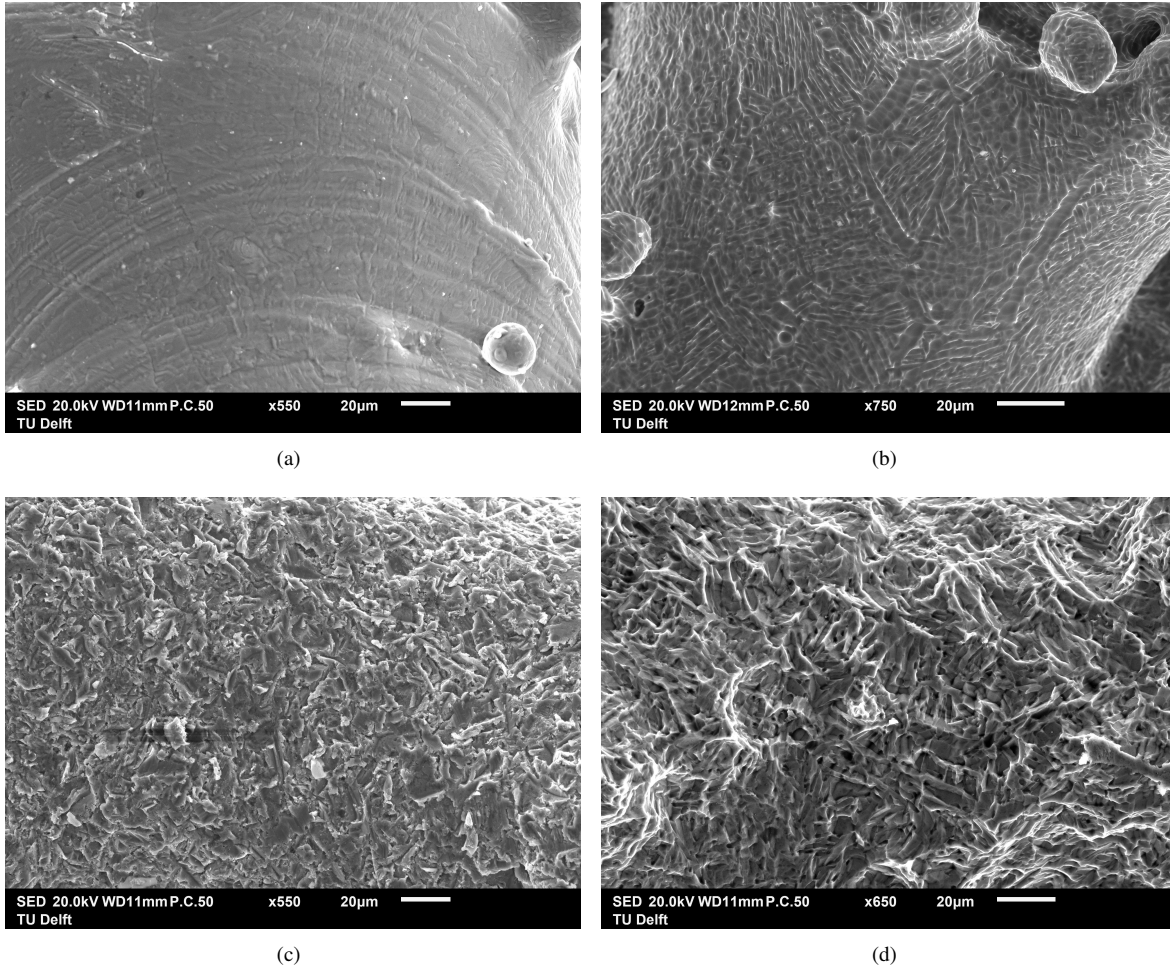


Figure 45. A set of four subfigures on (a) roughness continuous SLM HIP (b) roughness continuous SLM HIP CE1 (c) roughness continuous SLM HIP SB (d) roughness continuous SLM HIP SB+CE2

For all the sample types, the average relative density was determined using dry weighting. The relative density ρ_{rel} can be obtained using the following formula:

$$\rho_{rel} = \frac{\rho_{lat}}{\rho_{sol}} = \frac{w_{lat}}{w_{sol}} \quad (15)$$

Whereby w_{lat} and ρ_{lat} are the weight and the density of the lattice structured cylinder, respectively. w_{sol} and ρ_{sol} are the theoretical weight and density of the solid cylinder calculated using 4.43 g/cm^3 as the density for Ti6Al4V.

The results from the measurements are shown in figure 46. Herein it is clearly visible that both SB and CE reduce the relative density. Furthermore there is a large difference in relative density between the continuous and pulsed SLM samples. This is in line with what is reported in literature ([4], [22]).

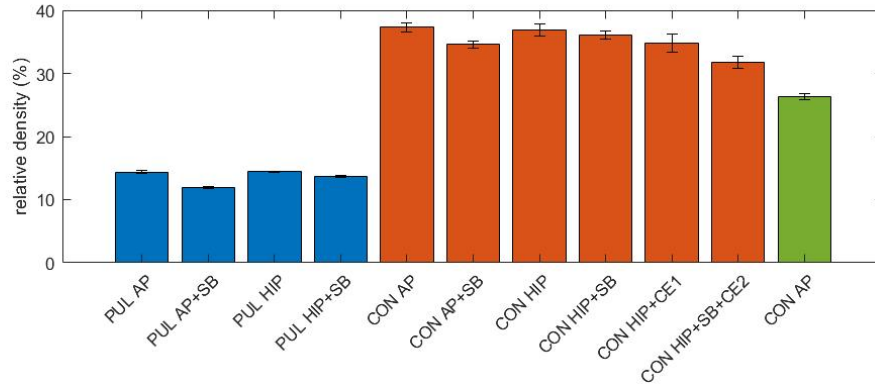


Figure 46. Effect surface modifications on the relative density of Ti6Al4V samples and herein also comparing continuous SLM samples (CON) with pulsed SLM samples (PUL)

4.2 Microstructural characterisation of spinal cage implants

In theory the characterisation of the cylindrical samples should be identical to the characterisation of the implants, however since the geometry has changed significantly some changes might be present.

The microstructure of the AP and HIPed implant samples was investigated. As can be seen in figure 47, the AP samples consist of the needle shaped α' microstructure while the HIP SB+CE samples consist of the lamellar $\alpha + \beta$ microstructure. This is in line with the previously determined microstructures of the cylindrical samples, shown in section 4.1.

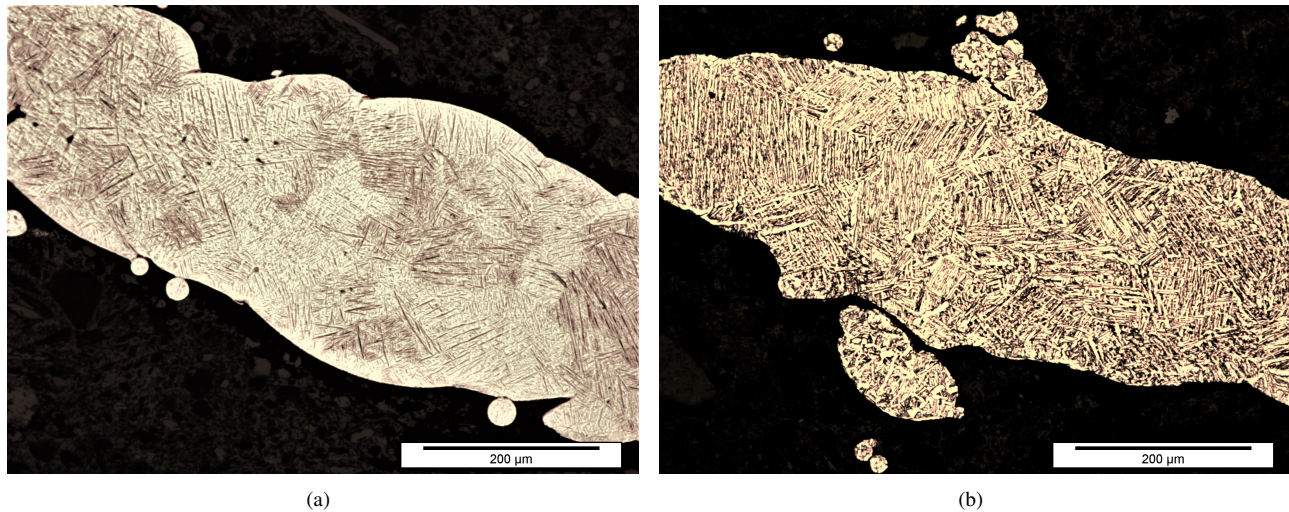


Figure 47. Figures regarding the microstructure of: (a) AP implant sample (b) HIP implant sample

The spinal cage implants were observed from the side to see the surface using the SEM. Furthermore they were cut perpendicular to the build direction to look at the struts and the effect of sandblasting.

Figure 48 shows that the effect of SB was limited to the surface of the implant sample. Only on the first 1 mm an effect of sandblasting was observed. This means that the core of the implant sample was not strengthened by the SB modification. Visually there is a clear difference in the effect of SB when comparing the effect of SB for the cylindrical samples (figure 44) with the effect on the implant samples. Furthermore no visual effect of CE is observed when comparing figure 48 with figure 45(b).

The processed implants were processed to have the products final shape and form, Therefore a polishing treatment was

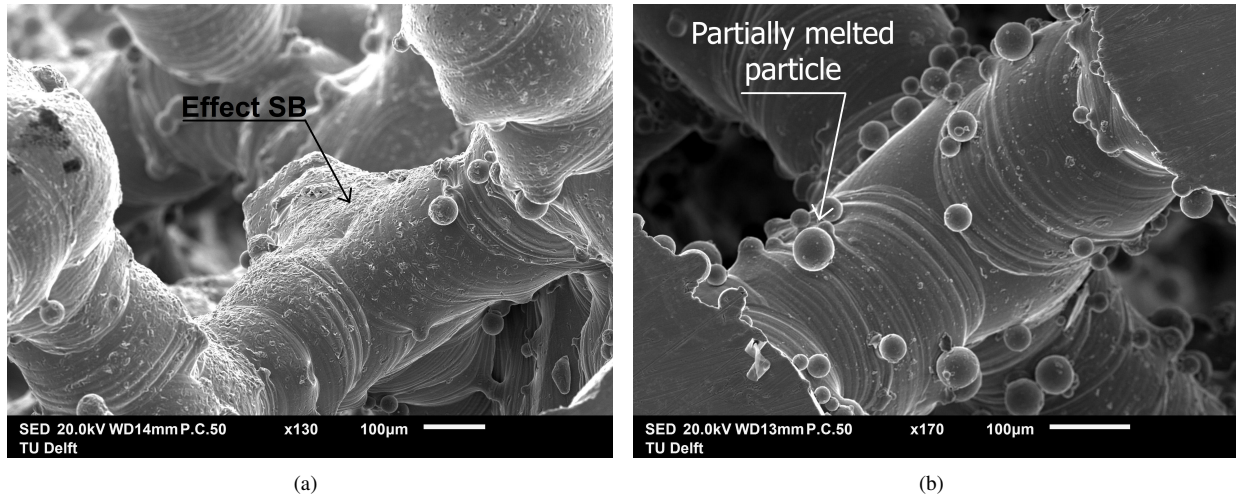


Figure 48. Figures regarding : (a) SB at the surface (b) SB at the core

applied to the head of the implant samples. SEM images were taken to see if potential damage was done on the lattice structure. As figure 49 shows, the polishing removes some material from a critical area. As the polished procedure was performed on the solid head of the implant the edge area whereby the lattice structure is attached to the solid also got polished slightly. In this area the nodes at the edge got reduced in size and occasionally removed by the polishing.

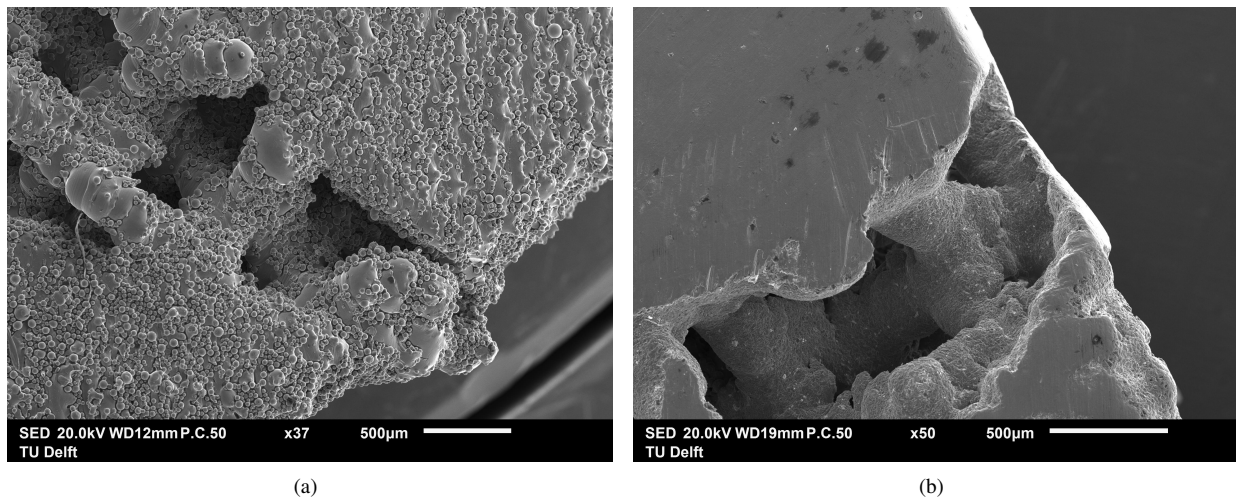


Figure 49. Figures regarding : (a) AP implant unpolished (b) HIP SBCE implant polished

To determine the relative density of the implant lattice structure, one must know the ratio in volume of solid and lattice structure of the implant. Using the CAD file in solidworks the volume of the lattice part and the solid part are determined to be 0.748 cm^3 and 0.639 cm^3 , respectively. The weight of the solid part can be calculated by using the volume and the 4.43 g/cm^3 density. This was calculated to be 3.313 g.

By subtracting the weight of the solid part from the weight of the implant the weight of the lattice part can be determined. Using the implant weight shown in table 8 the weight of the lattice structure for AP and HIP+SB+CE are 1.20 g and 0.89 g respectively. For AP and HIP+SB+CE a density of 1.60 g/cm^3 and 1.19 g/cm^3 are calculated by using the weight and the volume determined using solidworks. Using equation 15 we can divide $1.60/4.43$ and $1.19/4.43$ and get the relative densities of 0.36 and 0.27 for AP and HIP+SB+CE, respectively. This method of determining the relative density does however not take

Table 8. weight and relative density implant samples

	AP	HIP SB CE
weight (g)	3.974 ± 0.028	3.735 ± 0.060
relative density lattice	0.34	0.27

into account the effect of polishing, or any other removal of material from the solid section by SB.

4.3 Mechanical testing of cylindrical samples

In this section the results are shown for the static compression testing and the compression fatigue on the cylindrical samples from table 5. They were testing using the methods described in section 3.4.

4.3.1 Static compression properties of cylindrical samples

In table 9 an overview is given on the mechanical properties of all the involved cylindrical samples with surface modification and heat treatments. A subdivision is made between the pulsed and the continuous SLM samples.

Table 9. An overview of the compression test results for the cylindrical samples tested according to the ISO 13314 standard (CON = continuous SLM and PUL = pulsed SLM)

Sample type	Treatments and modification	Yield strength	1 st max stress	Plateau stress	Elastic gradient
		MPa	MPa	MPa	MPa
PUL	AP	18.5 ± 1.3	19.9 ± 0.9	11.7 ± 0.2	0.63 ± 0.06
	AP SB	17.3 ± 0.4	19.3 ± 0.5	10.6 ± 1.5	0.49 ± 0.04
	HIP	19.7 ± 0.8	21.3 ± 0.6	15.6 ± 0.7	0.89 ± 0.02
	HIP SB	18.3 ± 0.3	21.9 ± 0.3	16.5 ± 0.8	0.76 ± 0.02
CON $\rho_{rel} = 0.37$	AP	89.0 ± 4.4	98.3 ± 9.7	76.3 ± 2.7	2.84 ± 0.13
	AP SB	87.8 ± 3.9	91.9 ± 1.8	75.0 ± 2.6	2.57 ± 0.00
	HIP	115.2 ± 6.3	129.7 ± 9.9	100.1 ± 7.3	2.89 ± 0.83
	HIP SB	88.5 ± 6.5	121.6 ± 6.6	91.8 ± 7.2	3.16 ± 0.43
	HIP CE1	90.3 ± 5.1	109.4 ± 8.8	89.7 ± 3.8	2.30 ± 0.11
	HIP SB+CE2	86.7 ± 5.1	109.1 ± 1.5	84.6 ± 3.9	2.33 ± 0.22
CON $\rho_{rel} = 0.26$	AP	43.0 ± 3.3	69.4 ± 1.7	50.8 ± 1.6	1.01 ± 0.07

Figure 50 displays the mean compression graphs. When comparing continuous SLM samples and pulsed SLM samples in compression, the results show that overall the continuous SLM samples show much higher yield stress, elastic gradient, first maximum stress and plateau stress (figure 50(f)). However the samples in this comparison were created with a different relative density. As can already be seen by the continuous SLM sample with the lower relative density, the lesser thickness of the strut has a major influence on the static mechanical properties. It should also be noted that for the pulsed SLM samples the densification zone was not reached which is due to the larger lattice pore size whereby more distance in void must be compressed before no space is left between layers of compressed material. The effect of sandblasting for both the pulsed and continuous SLM is small, though there seems to be a slight trend towards decrease in static mechanical properties (figure 50(a) and 50(c)). This makes sense due to the reduction in strut thickness by sandblasting. The effect of HIP treatment for both pulsed and continuous SLM is significant. The mechanical strength is increased due to the phase transformation and the reduction in pores (Figure 50(b) and 50(d)). For SB after HIP treatment the effect on the pulsed SLM samples is very small and when considering the 1st max stress and the plateau stress the sandblasting even caused a small increase. For the continuous SLM samples the effect seems to be more significant, where in particular the yield strength has decreased. CE1 and the combination of CE2 and SB both have similar effects on the static mechanical properties where a decrease in yield stress and 1st max stress was observed. The regular compression test results are in line with the results reported in literature ([4], [22]).

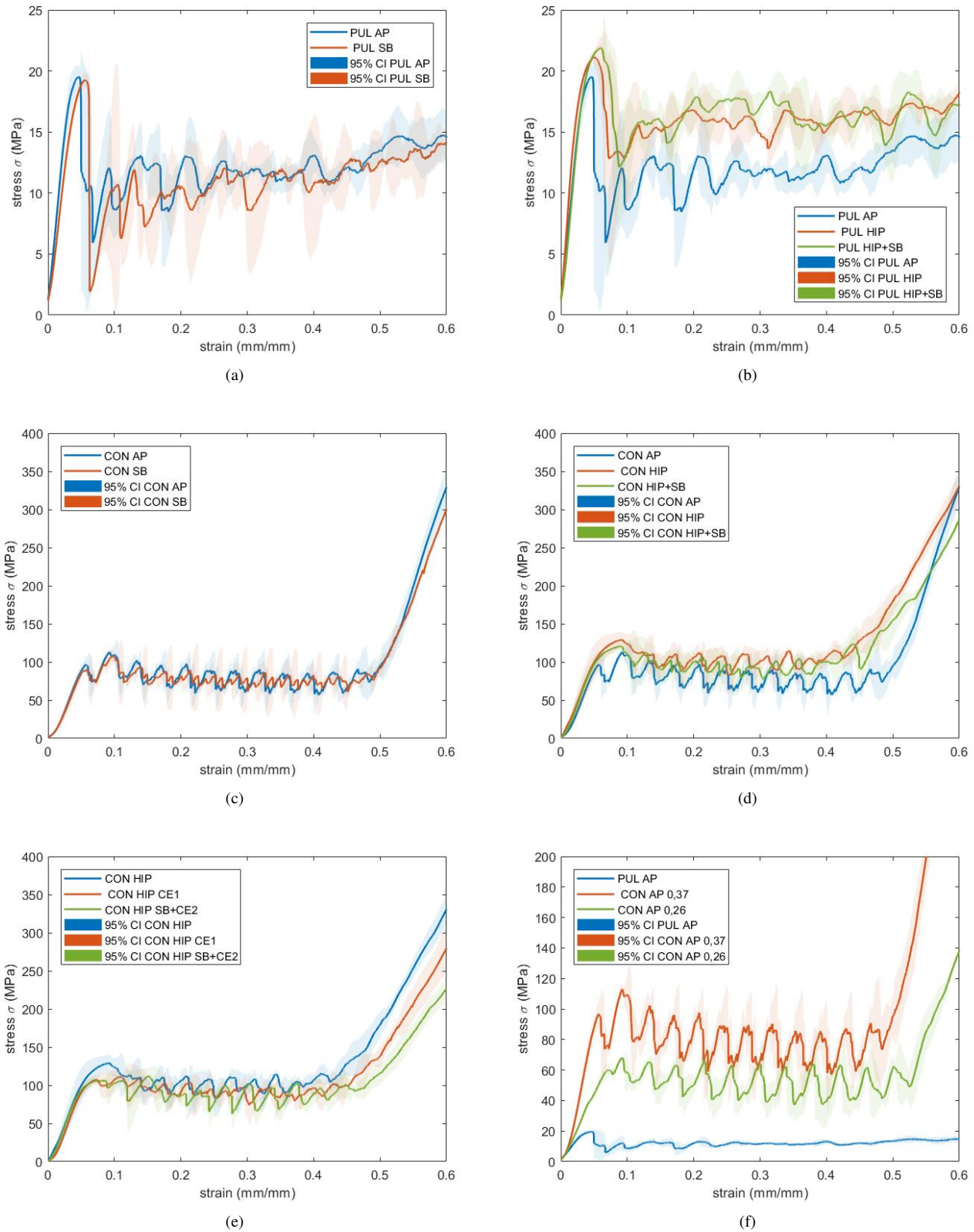


Figure 50. Mean compression graphs with 95% confidence interval of (a) comparison AP with SB on pulsed laser based SLM (PUL) (b) effect of HIP treatment in combination with SB on the static mechanical properties of pulsed laser based SLM (c) comparison AP with SB on continuous laser based SLM (CON) (d) effect of HIP treatment in combination with SB on the static mechanical properties of continuous laser based SLM (e) effect of CE1 and SB+CE1 on the static mechanical properties on continuous laser based SLM (f) reference graph comparing showing the difference in mechanical properties of the pulsed laser based samples and the continuous laser based samples

4.3.1.1 Normalisation of compression cylindrical samples

The mean compression graphs for the continuous SLM AP with 0.26 relative density, the SLM AP with 0.37 relative density and the pulsed SLM AP with 0.14 relative density were normalised based on the model proposed by Hooreweder *et al* [22] described in section 3.4.1.1 (figure 51). For the normalisation these sample groups were normalised to have a relative density of 0.30.

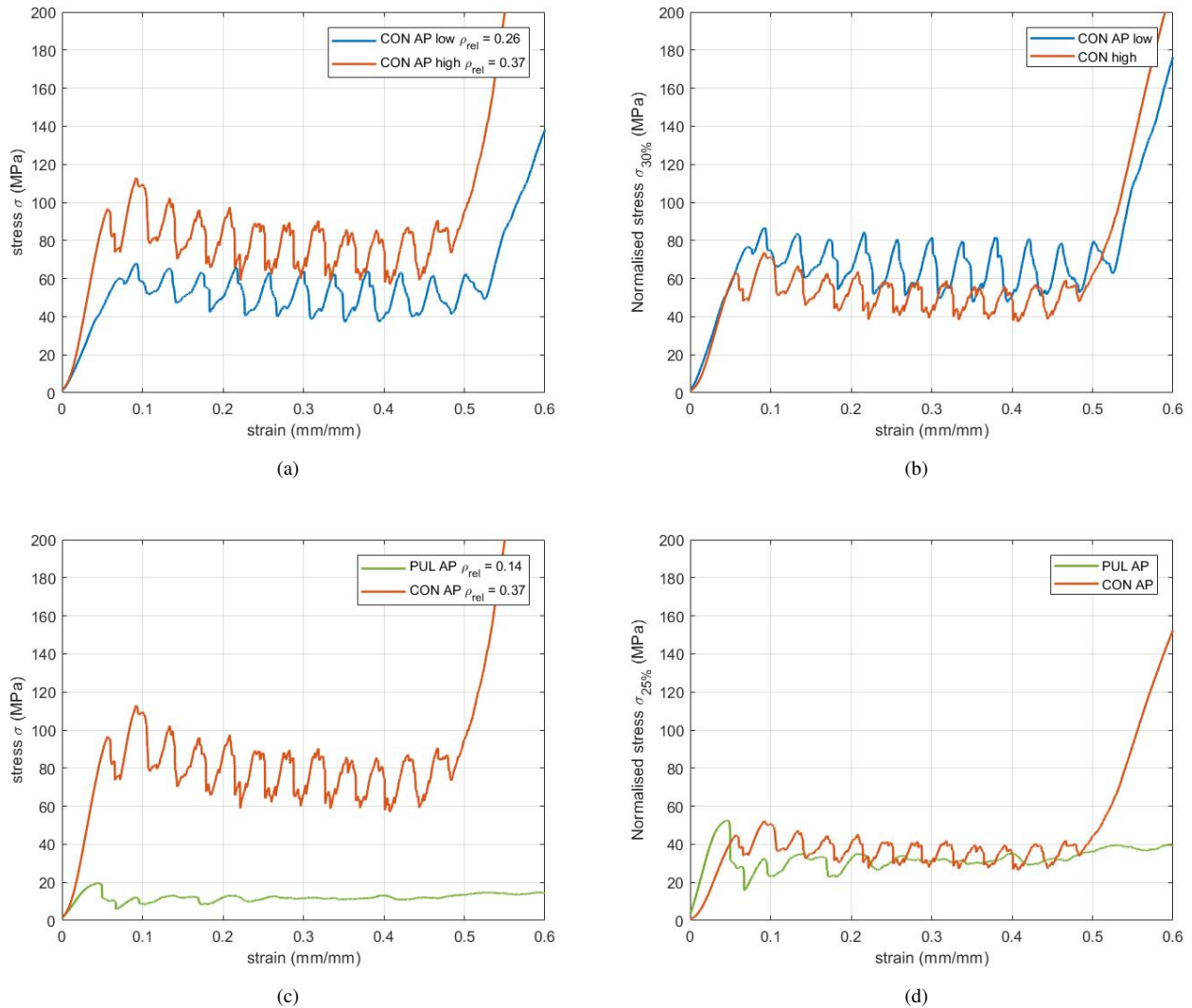


Figure 51. Figures regarding cylinder mean compression graph of AP continuous SLM samples with different relative density's (a) regular compression graphs continuous SLM (CON) 0.37 and 0.26 relative density ; (b) normalised compression continuous SLM 0.37 and 0.26 relative density (c) regular compression graphs 0.37 continuous SLM and 0.14 pulsed SLM (PUL); (d) normalised compression 0.37 continuous SLM and 0.14 pulsed SLM (PUL)

In table 10 it can be seen that the normalised yield stress and elastic gradient are normalised quite well when only comparing the continuous SLM samples. The standard deviation values in this table are the same as in table 9. The 1st max stress and the plateau stress have larger difference. When comparing the continuous SLM samples with the pulsed SLM samples it can be noted that the elastic gradient and the yield stress are significantly higher for the pulsed SLM samples. However the 1st max stress and the plateau stress are lower for the pulsed samples compared with the continuous samples.

One of the most important aspects in this normalisation is the accuracy in measuring the relative density. An inaccuracy in

Table 10. Comparison of continuous SLM AP ($\rho_{rel} = 0.37$), continuous SLM ($\rho_{rel} = 0.26$) and pulsed SLM ($\rho_{rel} = 0.14$) samples both regular and normalised

Sample type	Relative density	Yield stress MPa	1st max stress MPa	Plateau stress MPa	Elastic gradient GPa
CON AP low	0.26	43	69	51	1.01
CON AP high	0.37	89	98	76	2.84
PUL AP	0.14	19	20	12	0.63
CON AP low	0.30	53	77	65	1.28
CON AP high	0.30	62	63	50	1.37
PUL AP	0.30	67	74	44	2.08

measuring the relative density would cause difference in the normalised values. An inherent fault in measuring the relative density is the damaged surface where the samples are removed from the print bed. The removal of material on this side decreases the weight of the sample which means that a lower relative density is measured than the actual relative density. Furthermore an important parameter in normalising is the chosen common ground relative density which in the case is 0.30. It is important that this parameter is more or less in the middle of the measured relative densities, as when it is far apart from one of the measurements it will increase the elastic modulus as well as the wavering of the plateau region significantly.

The mean compression graphs of the continuous AP, AP SB, HIP, HIP CE1, HIP SBCE2 are shown in figure 52(a) and 52(c). In figure 51(b) the normalised curves with respect to strut thickness are shown for AP and AP SB. When both sample groups have the same relative density of 0.35, SB has increased the mechanical properties compared to AP. In figure 51(d) the normalised curves with respect to strut thickness are shown for AP, HIP, HIP CE1 and HIP SB CE2. When normalised to the same relative density HIP treatments improves all static mechanical properties. HIP CE1 shows no clear improvement, however the combined effect of HIP SB+CE2 improves all mechanical properties significantly.

Table 11. Comparison normal static compression results with the normalised to 0.35 relative density compression results

	Sample type	relative density	yield stress MPa	1st max stress MPa	plateau stress MPa	Elastic gradient GPa
Normal	AP	0.37	89	98	76	2.84
	AP SB	0.35	88	92	75	2.57
	HIP	0.37	115	130	100	2.89
	HIP CE1	0.35	90	109	90	2.30
	HIP SB+CE2	0.32	87	109	85	2.33
Relative density normalised	AP	0.35	84	85	67	1.85
	AP SB	0.35	90	92	77	2.02
	HIP	0.35	92	116	90	1.94
	HIP CE1	0.35	90	108	91	2.34
	HIP SB+CE2	0.35	104	128	102	2.79

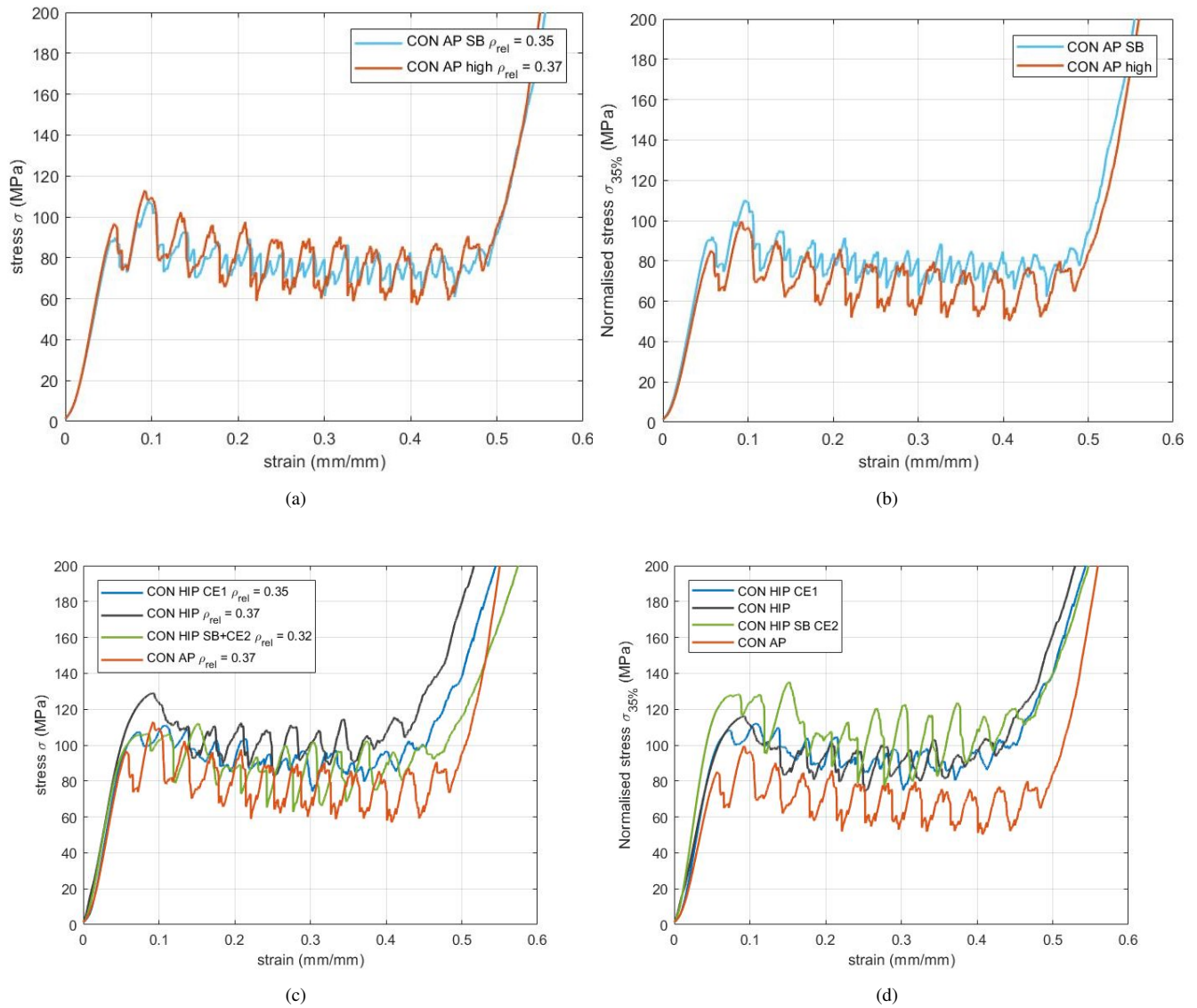


Figure 52. A set of subfigures regarding (a) mean compression graph AP and AP SB (b) mean compression graph for the relative density normalised AP and SB (c) mean compression graph AP, HIP, HIP CE1 and HIP SB+CE2 (d) mean compression graph for the relative density normalised AP, HIP, HIP CE1 and HIP SB+CE2

4.3.2 Results of compression fatigue on cylindrical samples

In this section the results are shown of the compression fatigue performed on the cylindrical samples with post process treatments described in section 3.1.1 and according to the methods described section 3.4.2.

4.3.2.1 Normal fatigue

Compression fatigue tests were performed on cylindrical Ti6Al4V metamaterial samples which were subjected to HIP, SB and CE. All fatigue results are shown in the form of an S-N curve as shown in figure 53(a). What can be noticed is the vast difference in fatigue resistance when comparing continuous with pulsed SLM samples. As mentioned before this is partially due to difference in relative density. The relative density of the pulsed SLM samples is around 0.13 and for the continuous SLM samples it is around 0.35. Overall for both the pulsed and continuous SLM sample groups the HIP treatments seems to work very well for improving the fatigue resistance. This is most likely due to the decrease in unintended porosity, the decrease in grain size and the phase transformation to a more ductile structure. Also the confidence intervals do not overlap which proves statistically that the HIP treatment improves the fatigue resistance of Ti6Al4V lattice structures (figure 53(f)). Sandblasting seems to have only a small effect on the fatigue resistance, however bear in mind that the relative density has been lowered. The added strength might be cancelled out by the lost material. Continuous SLM HIP CE1 and HIP SB+CE2 seems to influence the fatigue more, where in particular the LCF of the SB+CE2 was heavily decreased compared to the HIP sample. Compared to the HIPed samples, it can be observed that the HCF behaviour for the continuous SLM HIP CE1 was almost identical and for the continuous SLM HIP SB+CE2 it was a small decrease.

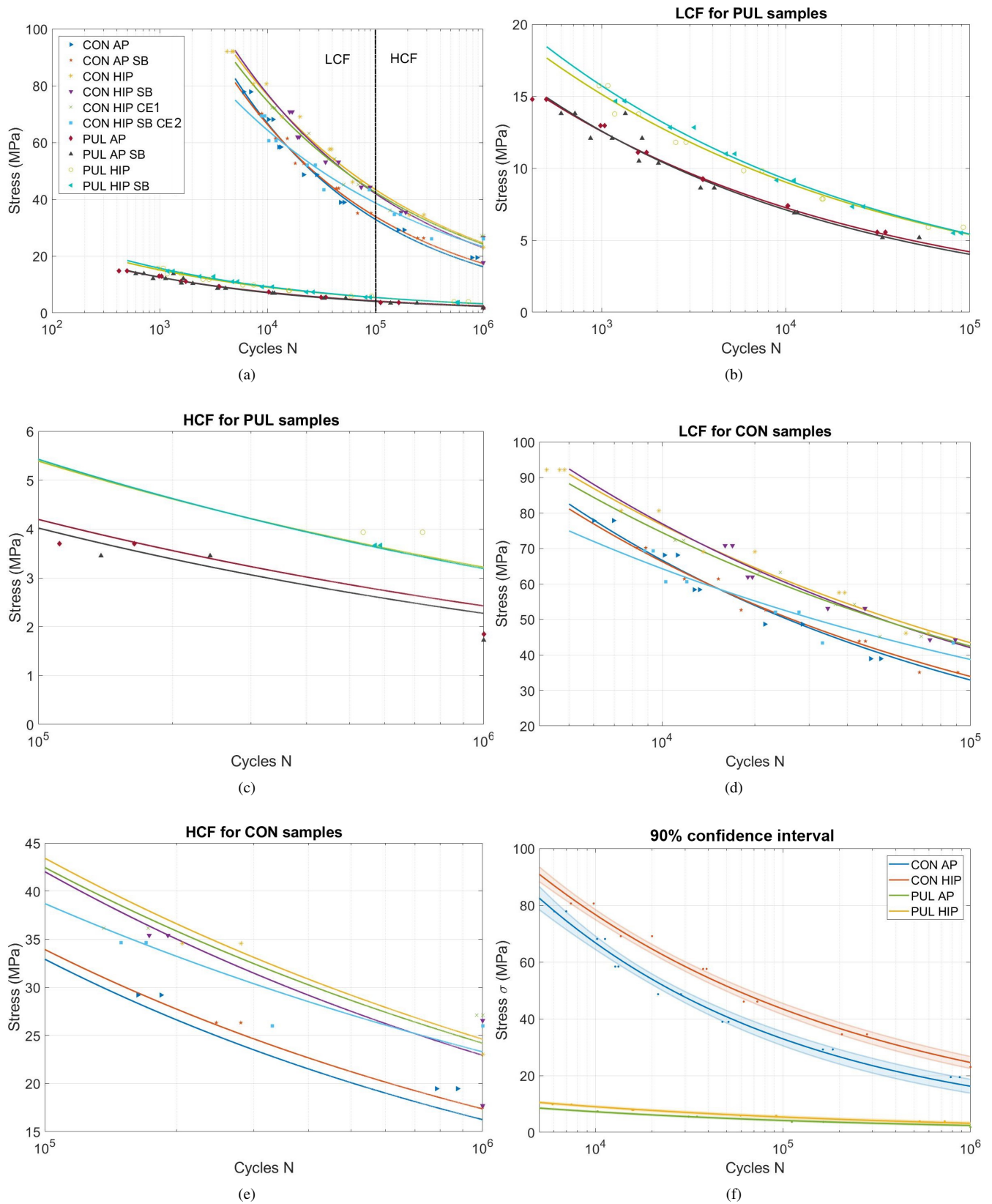


Figure 53. a set of sub figures regarding (a) All regular S-N curves (b) LCF of the pulsed laser based samples (c) HCF of the pulsed laser based samples (d) LCF of the continuous laser based samples (e) HCF of the continuous laser based samples (f) 90 % confidence interval on AP vs HIP samples

4.3.2.2 Fatigue normalised with respect to yield strength

When normalising the fatigue resistance against yield strength the ratio between a materials dynamic and static strength can be found. As the mechanical strength is highly dependent on relative density, SLM technique, heat treatment and surface modification, a comparison can be made on the effect of one parameter among the three when the others are kept constant. The relative density is however tied to the surface treatment. Furthermore two different methods of scanning were applied (continuous and pulsed SLM). The only valid comparison can be made between AP and HIP samples. On the other samples only combined parameter effect speculation can be done and indications can be deduced.

For the pulsed SLM samples the effect of HIP seems to improve the ratio between fatigue resistance and yield strength [54\(c\)](#). This probably is due to the decrease in internal porosity, the phase transformation and the increase in grain boundary density. When looking at the continuous SLM samples the HIP only seems to improve the ratio at HCF, whereas at LCF the AP sample ratio is better.

When looking at the effect of sandblasting, for the AP samples the effect is negligible. For the HIP samples on the other hand the effect is significant for both the pulsed and the continuous SLM samples. This indicates that HIP is more effective on smaller strut thickness.

The effect of HIP CE1 and HIP SB+CE2 is significant when comparing to HIP. The dual effect of SB and CE2 is however lower compared with SB and CE1 individually. Perhaps this is because the strut thickness was reduced significantly.

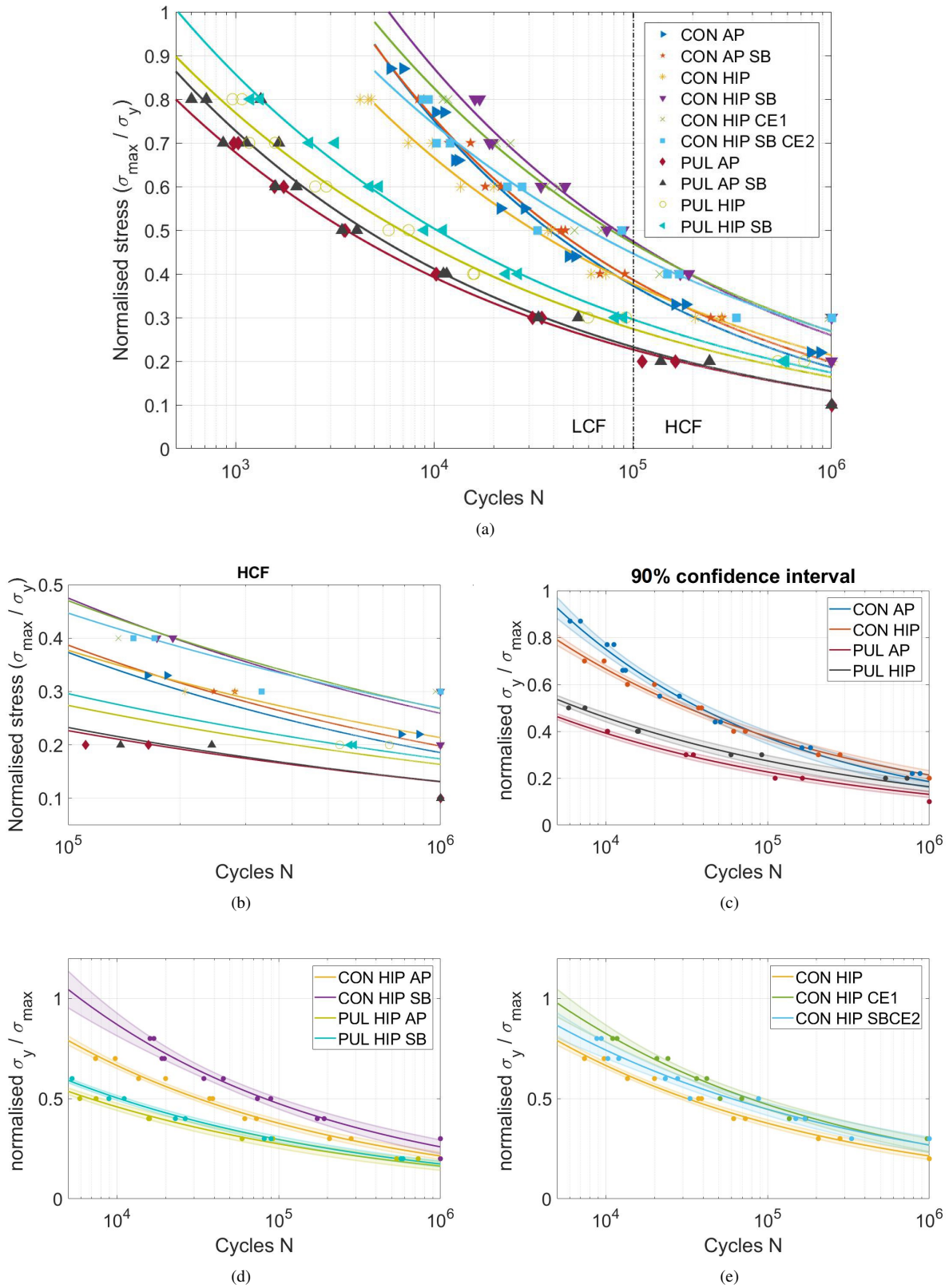


Figure 54. a set of sub figures regarding (a) all normalised fatigue results with respect to yield strength (b) HCF of all normalised fatigue results (c) 90 % confidence interval of AP and AP HIP samples. (d) 90 % confidence interval of HIP and HIP SB samples (e) 90 % confidence interval of HIP, HIP CE1 and HIP SB+CE2 samples

4.3.2.3 Fatigue normalised with strut thickness

Local stress normalisation was applied on the fatigue graphs of the continuous SLM samples (figure 56). In figure 55 the normalised to strut thickness graph can be seen for the pulsed and continuous SLM samples. Here it is clear the the pulsed samples show significantly less fatigue resistance in both LCF and HCF. However, as Kumar states [8] for pulsed SLM samples the location of failure is in between layers of spot welds, whereas the failure of continuous SLM samples is on the nodes itself. The local stress normalisation described in section 3.4.2.1 assumes that the stress concentration at the node is the crack initiation area. The local stress normalisation can therefore only be applied on the continuous SLM samples.

In theory the local stress is a material property and not a meta material property. Hence, the results shown in figure 56 show the effect of modifications on the properties of the material Ti6Al4V as if it were a solid. This means that potential loss of material due to SB and CE is accounted for in the normalisation and each sample is geometrically independent.

In this section two AP samples were tested at different relative densities and thus different strut thicknesses. If the normalisation accounted for all influencing parameters the local failure stress should be equal for both samples and therefore the graphs should be aligned. This is more or less the case, as can be seen in figure 56(c), where the CI show a clear overlap. However the alignment is not a perfect fit. An important factor is probably the measured relative density as the accuracy of this measurement influences the results greatly. Furthermore the list of factors not accounted for by this normalisation effects the measurement greatly. The results obtained by Hooreweder *et al* [22] displayed more overlapping results in fatigue normalisation.

Non the less, when normalised to local stress, a clear effect of HIP can be seen on the fatigue resistance due to the reduction in internal porosity and the phase transformation (figure 56(c)). In local stress, sandblasting improves the local fatigue resistance greatly as the continuous SLM confidence interval of AP and AP SB do not overlap (figure 56(d)). The effect of SB on HIP samples, seems to be less significant however a slight change can be observed. Finally the effect of CE1 and the effect of SB+CE2 seems to further improve the HIP samples. In particular the HIP SB+CE2 show the best properties on the local fatigue resistance.

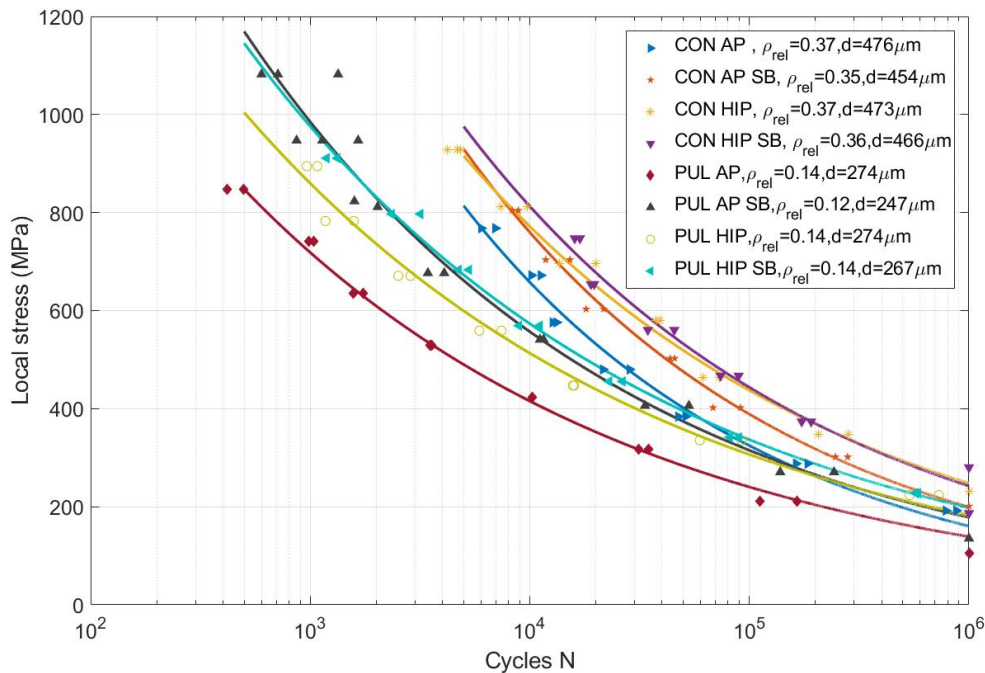


Figure 55. fatigue results normalised to local stress including PUL samples

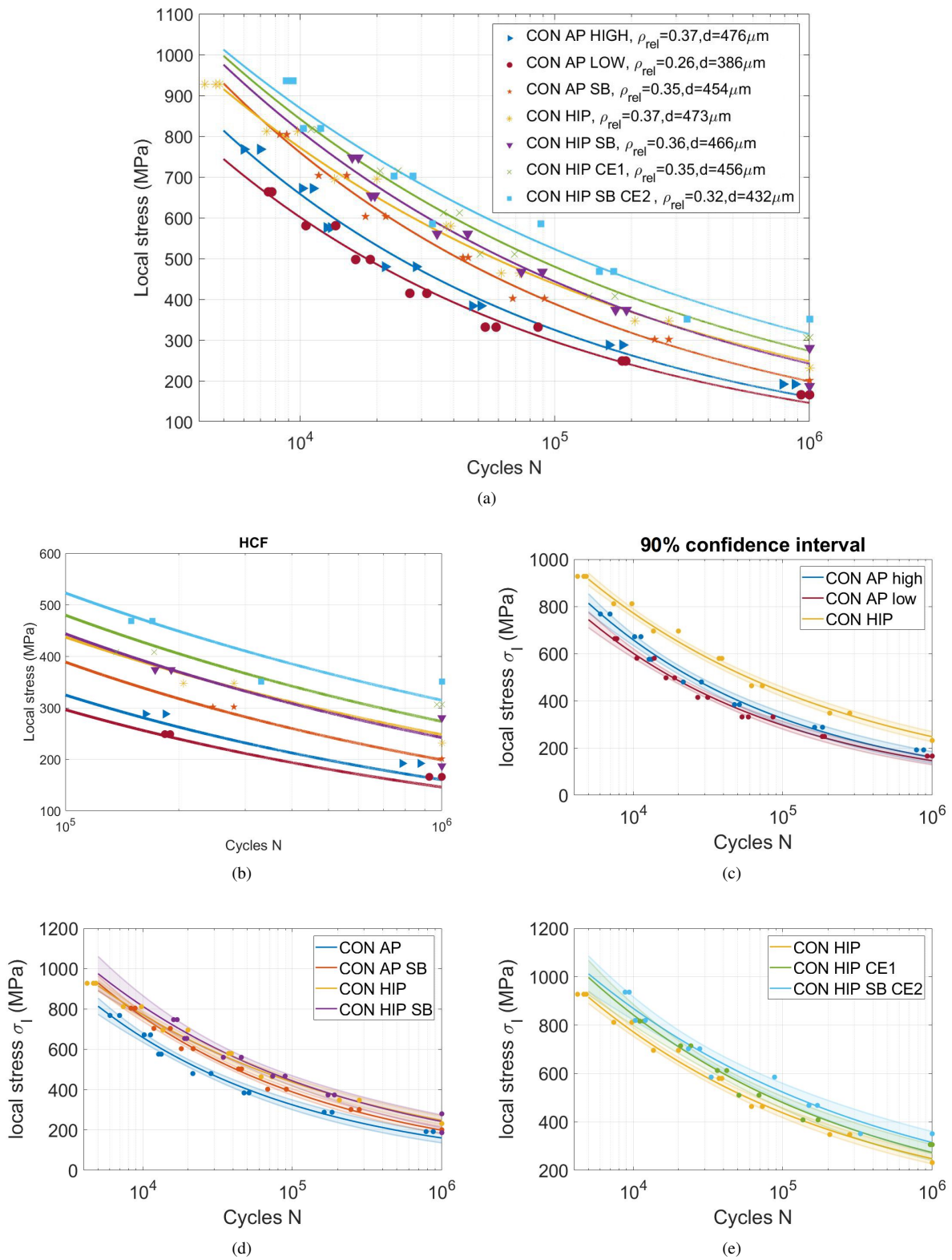


Figure 56. a set of five sub figures regarding (a) All CON curves local stress at the strut (b) HCF detail of the fatigue graphs (c) 90 % confidence interval comparing the AP 0.37 density and the 0.26 density with the HIP sample (d) 90 % confidence interval showing the local effect of SB (e) 90 % confidence interval showing the local stress effect of CE1 and HIP SB+CE2

4.4 Mechanical of testing implant

In this section the samples discussed in section 3.1.2 were tested according to the methods described in section 3.5.

4.4.1 Static compression testing of implants

A static compression test was performed according to the ASTM F2077 standard. The results of the compression test are shown in table 12. The yield force was lowered significantly whereas the first max force was slightly increased by the HIP and SB treatment. The stiffness remained very similar.

Table 12. Results of compression tests of AP and HIP SB+CE samples

Sample	yield force N	1st max force N	Stiffness N/mm
AP	17748 ± 688	18770 ± 269	57655 ± 11921
HIP SB CE	15558 ± 626	19281 ± 807	57416 ± 8822

Figure 57(a) shows the mean compression graphs with CI. As can be seen the most significant difference between HIP SB and AP is the ductility. The ductility of the processed samples is more probably due to the phase transformation during the heat treatment. The ductility is quantified by the strain up to the first max force which in this case are 0.040 and 0.051 mm/mm for AP and HIP SB+CE, respectively.

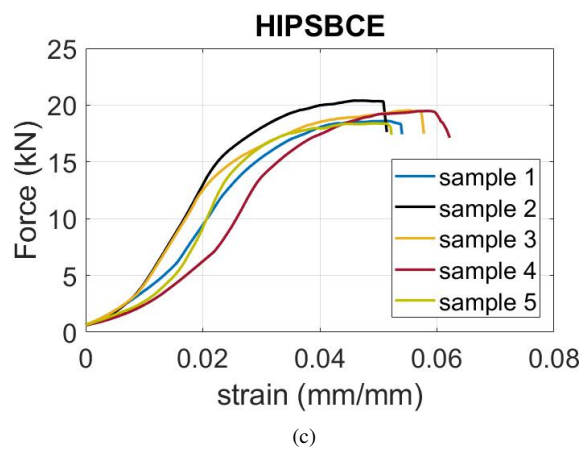
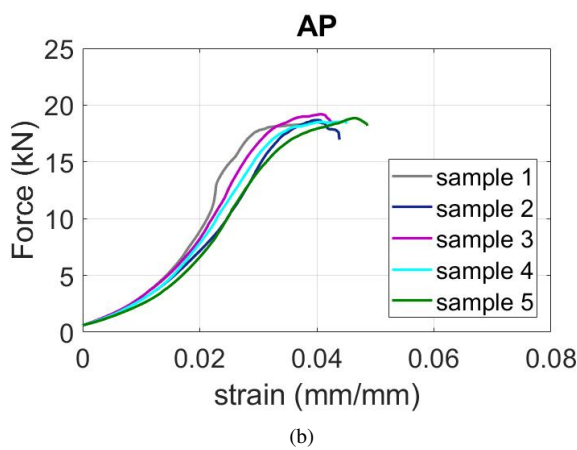
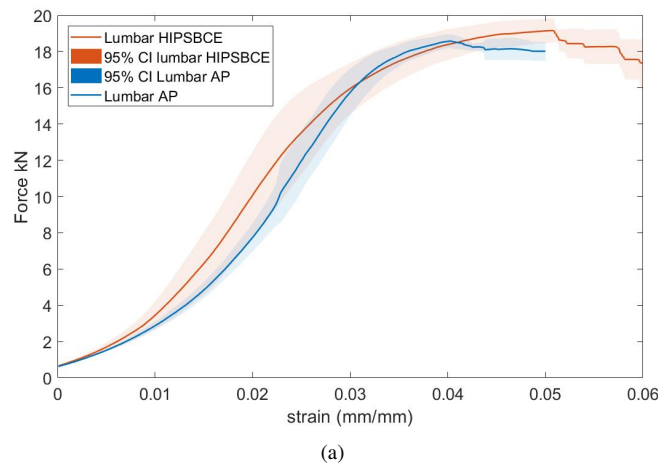


Figure 57. a set of sub figures regarding (a) Mean compression results implant testing with 95% CI (b) compression results AP lumbar implant samples (c) Results HIPSBCE lumbar implant samples

4.4.2 Fatigue testing of implants

The same samples used for the compression tests were subjected to compression fatigue testing. The normal fatigue results do not show any significant improvements with post process treatments (figure 58(c)). However, when normalised the processed samples improve significantly especially in LCF. When looking at the CI plotted in figure 58(c) and 58(d) the overlap of the regular F-N curve is very big, whereas for the normalised fatigue graph the overlap is smaller and the improvement trend seems to be more pronounced.

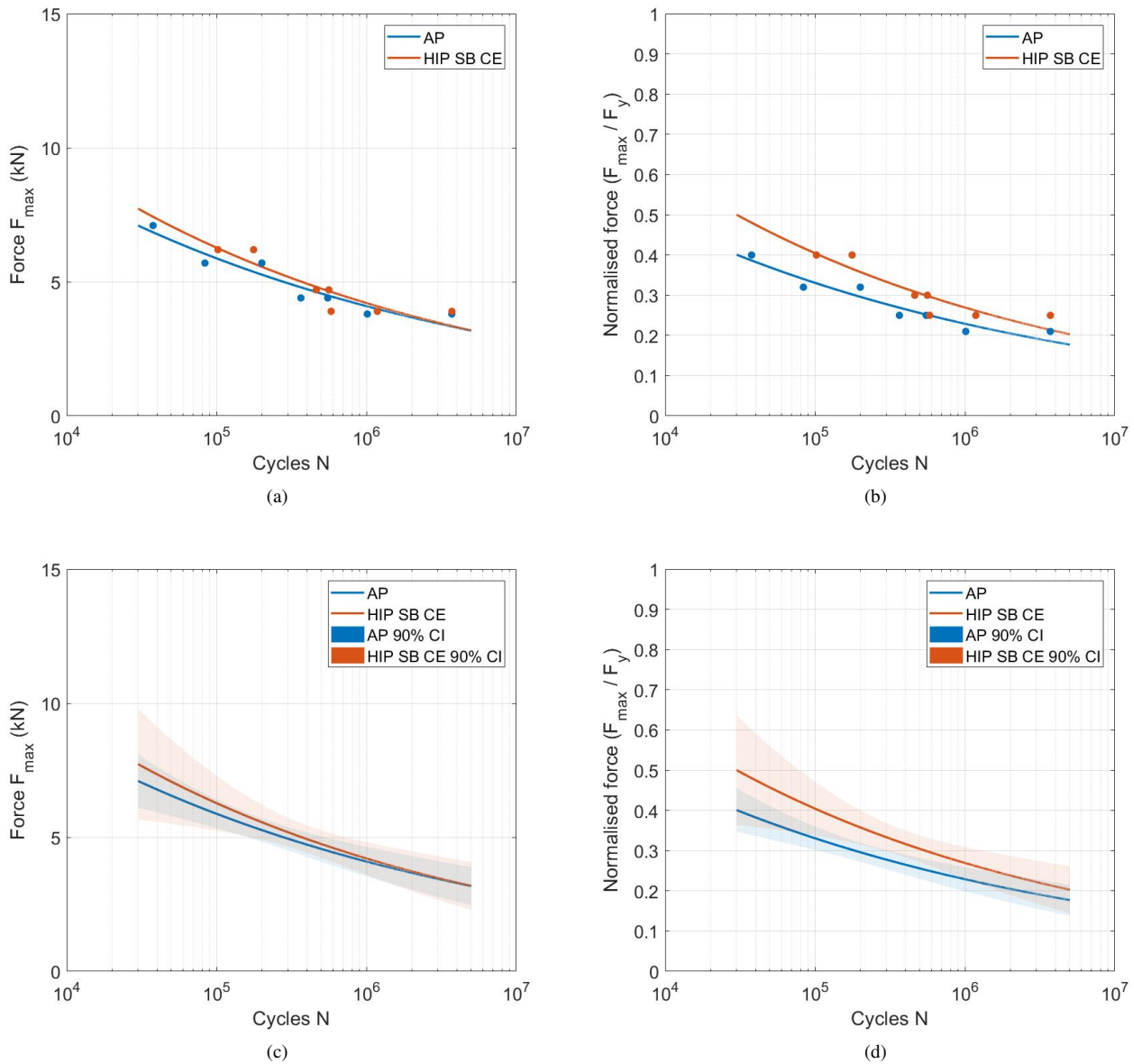


Figure 58. A set of four subfigures on the lumbar implant fatigue (a) F-N curve regular (b) F-N curve normalised to yield force (c) F-N curve regular 90 % CI (d) F-N curve normalised to yield force 90 % CI

Figure 59 shows a representative displacement-cycles curve of a HIP SB CE sample. Generally, the behaviour was very similar between the samples. The fatigue process of the samples generally initiated in the top corners of the porous section of the material, before machine displacement of 2 mm end of test displacement was reached. The top corner (indicated by fatigue zone in figure 59) porous section slowly crumbles up to the point where the solid sections become loadbearing. After, in this representative case, around 3.7 million cycles the structure collapses.

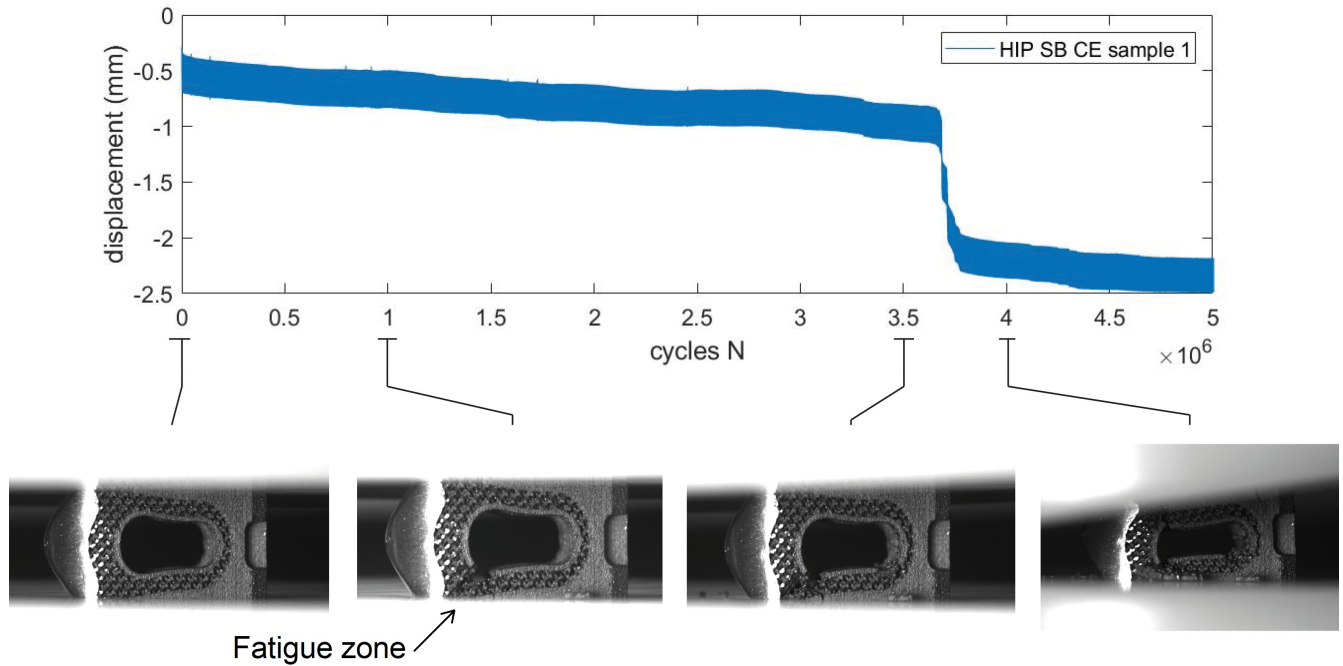


Figure 59. Failure propagation of HIP SB+CE implant representative sample with cyclic loading of 3.89 kN

4.5 Wettability study

In this section the results are shown of the wettability testing subdivided into the Dip test and the Sessile drop test. The experiments were conducted using the methods described in section 3.6 on the samples described in section 3.1.3.

4.5.1 Sessile drop test

In figure 60 the results from the Sessile drop test are shown. On the complete set of results the ANOVA (analysis of variance) was applied resulting in a p value of $2.81296 \cdot 10^{-12}$. This means that the statistical probability of all of the results belonging to the same group is very small. To further analyse if the individual groups showed any deviation, Tukey's test was applied. Tukey's test proved that the groups APCE2 and AP SB+CE2 are statistically different from any other groups (appendix C). More data points must be added to prove that the other groups have statistical differences as well. The average contact angle decreased when SB was applied, although the decrease was not immense as the standard deviations still overlap. CE1 slightly increased the contact angle and CE2 increased the contact angle by a great amount almost reaching 90 degrees. Furthermore CE2 shows the largest amount of deviation. The combined effect of SB and CE1 does not change the contact angle significantly, however the scatter was very low. The effect of SBCE2 is again intermediate between CE2 and SB. Figure 61 displays the contact angle of the various treatment whereby a random measurement point was taken. The results are within the range of the variance of 40° to 80° , as reported by Hierro-Oliva *et al* [37]. Hierro-Oliva *et al* [37] reported a stable contact angle of approximately 80 degree for AP Ti6Al4V. However the results were on wrought samples and not on a curved surface.

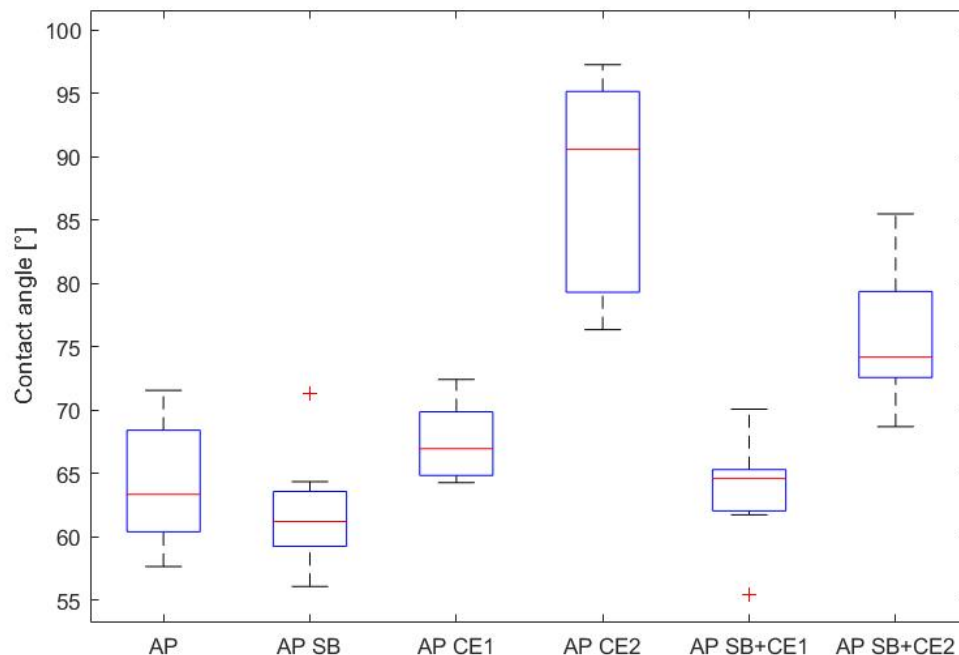


Figure 60. Contact angle measurement boxplot with mean (red line) SD (black lines), confidence interval (blue lines) and outliers (+)

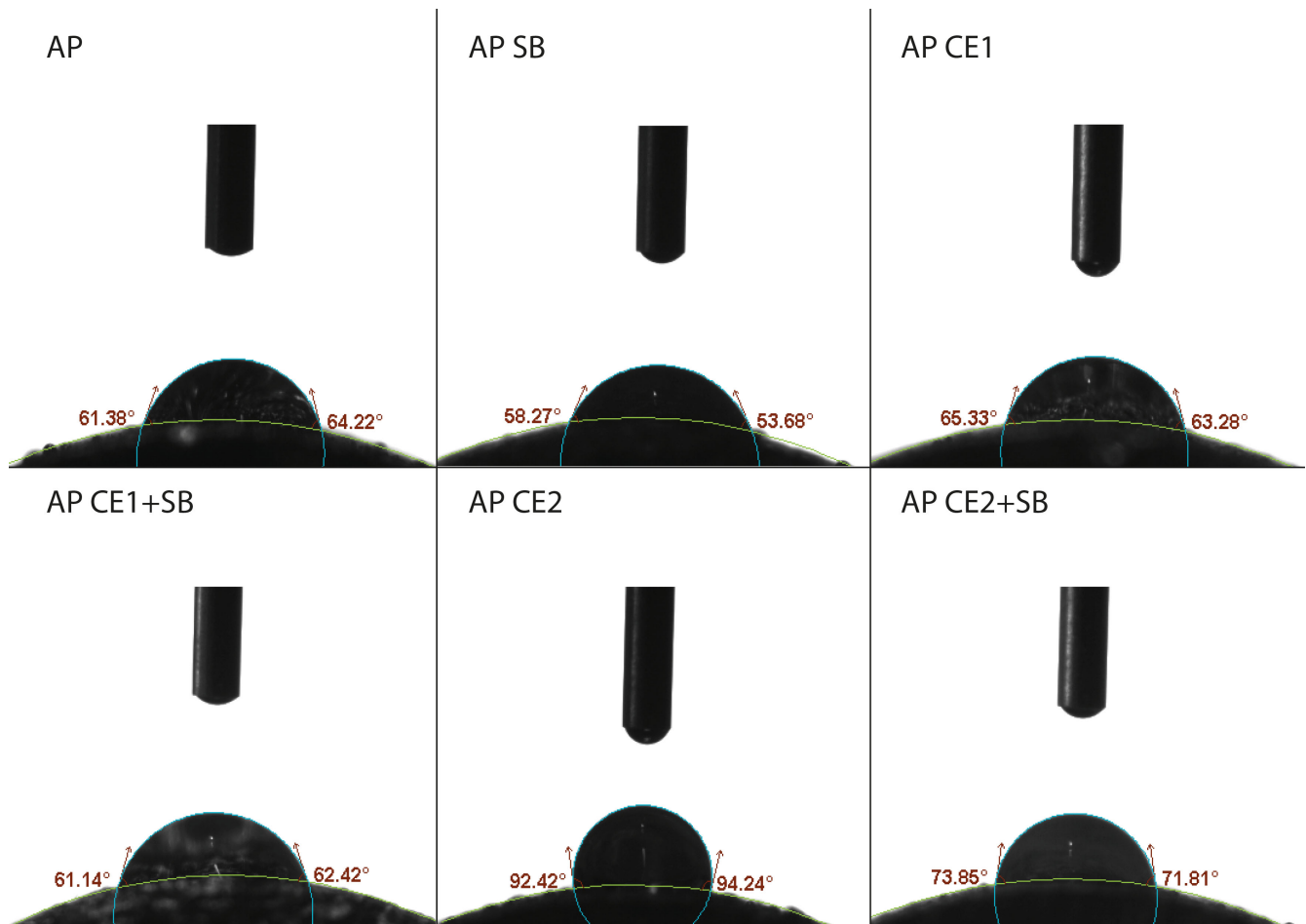


Figure 61. visual representatives of contact angle measurements, as provided by the contact angle measurements

4.5.2 Dip test

Lattice cylindrical samples were dipped in coloured water to determine if the effect of surface treatment applied on the solid cylindrical samples is representative of the effect of the surface treatment applied on the lattice cylindrical samples. Figure 62 shows the cylindrical samples after 1 min submersion in the coloured water. The effect of SB seems to increase the contact angle as the coloured water moves upwards into the cylinder suggesting a more hydrophilic surface was created. This makes sense as the SB increases roughness which increases surface area and as Ti6Al4V attracts water an increase in surface area would mean more attraction to water. Both CE1 and CE2 seem to slightly reject the coloured water. This suggests that the surface has become more hydrophobic. The only possibility for a surface to go from hydrophilic to hydrophobic is that the surface composition has changed. It was observed that for CE2 corrosion occurred on that surface during etching which could be the reason for the change in wettability behaviour. For the CE1 sample there was no corrosion visible, however an EDS (Energy-dispersive X-ray spectroscopy) analyses could be performed to show a possible change in composition. The combined effects from SBCE1 and SBCE2 seems to have an intermediate state between SB and AP. This makes sense since SB would decrease the contact angle and CE would increase the contact angle.

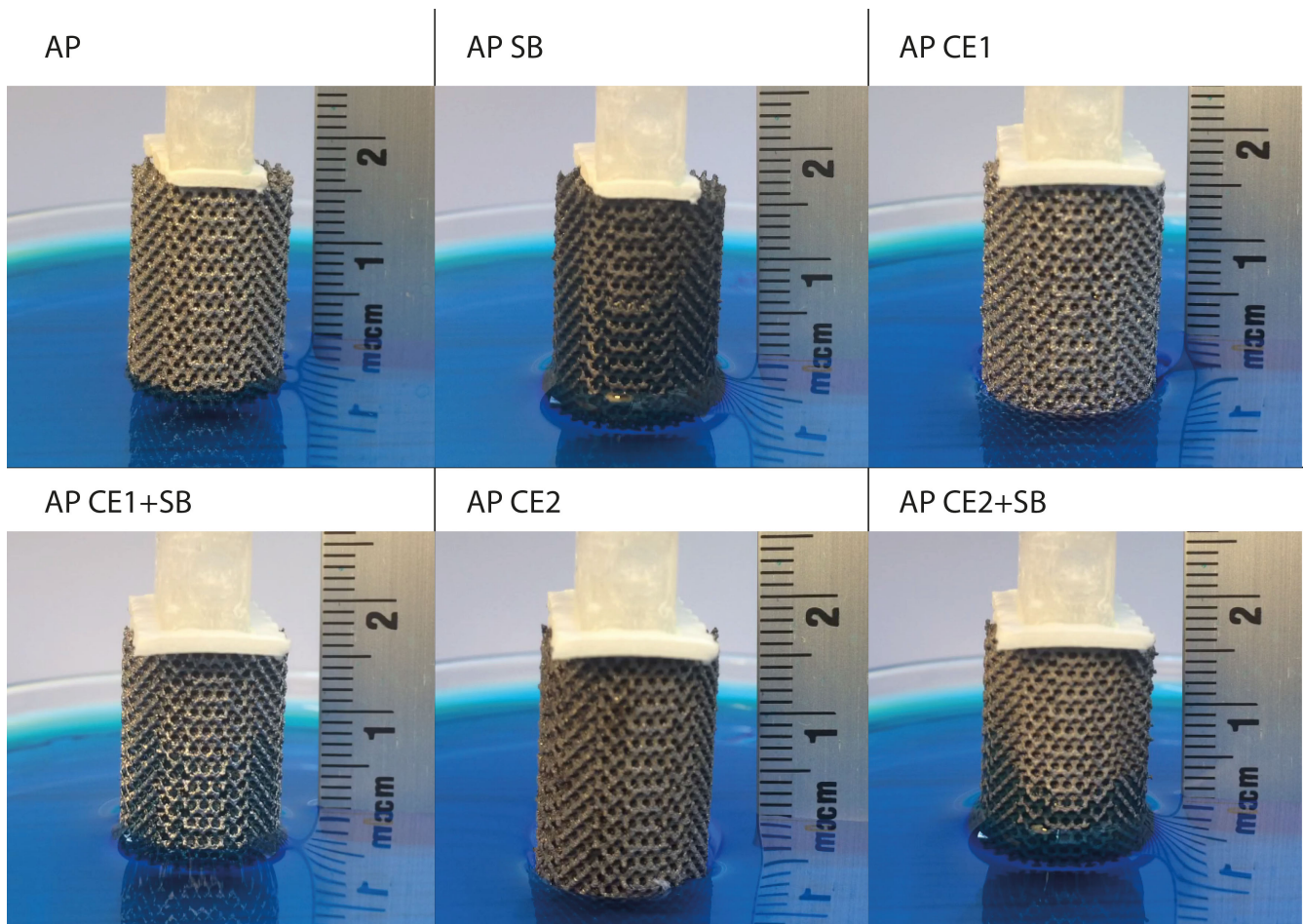


Figure 62. Results Dip test wettability

5 Discussion

5.1 Behaviour of cylindrical Ti6Al4V samples

5.1.1 Microstructural comparison between continuous and pulsed SLM

In the current research cylindrical samples of Ti6Al4V metamaterial manufactured by SLM were subjected to the HIP heat treatment and the surface modification of SB and CE. Furthermore two scanning methods of continuous and pulsed SLM (figure 63) were compared with and without surface modifications.

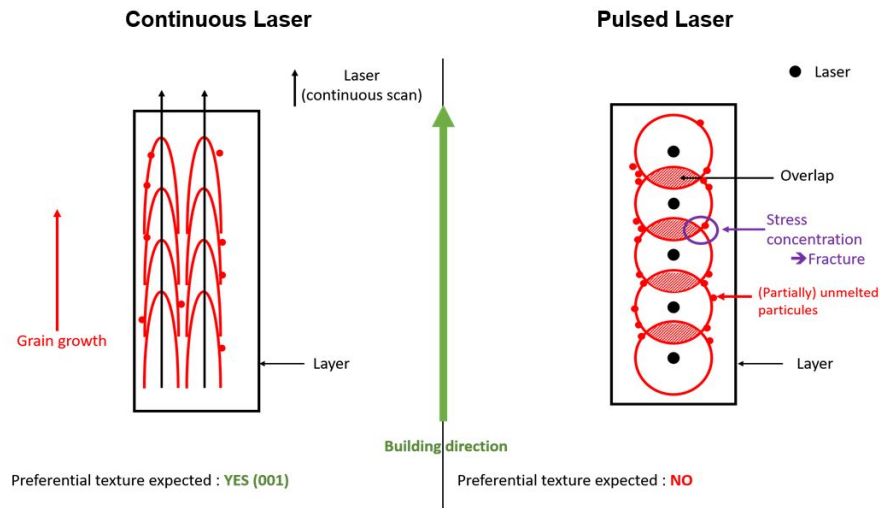


Figure 63. Schematic comparison of the continuous and pulsed SLM methods

Grain boundaries prohibit dislocation movement, which means that when there are more grain boundaries (hence smaller grains) it increases the tensile strength. Furthermore grain boundaries act as crack growth barriers. Therefore for continuous SLM samples with smaller grains both static and dynamic mechanical properties are expected to benefit more from the effect of grain boundaries.

By studying optical micrographs a difference in the grain growth preferential orientation was observed between continuous and pulsed SLM (figure 37). This was further confirmed by the EBSD images (figure 38 and 39). This comparison reveals that pulsed sample has a greater variation of grain sizes and no preferential orientation of the columnar grains in contrast to continuous SLM. The shape of the prior β grains for continuous SLM was pillar (also known as columnar) shaped in the build direction. A follow-up study can be performed on the difference in texture and grain size for both SLM scanning methods.

By studying of optical micrographs of etched samples it was observed that a possible difference in grain growth direction was observed between continuous and pulsed SLM (figure 37). This was further confirmed by the EBSD images (figure 38 and 39). This comparison reveals that pulsed sample has a greater variation of grain sizes and no preferential orientation of the columnar grains in contrast to continuous SLM. The shape of the prior β grains for continuous SLM was pillar shaped in the build direction. A followup study can be performed on the difference in texture within grains for both scanning methods.

The disparity in microstructure between pulsed and continuous SLM can be attributed to the difference in heat generation and subsequent cooling (figure 63). The pulsed laser generates heat in a circular area surrounding the spot being illuminated creating a melt pool. After the end of the illumination the heated area quickly cools down at rates of 10^4 to 10^6 K/s [41, 42], possibly solidifying before the next point is illuminated. Hence discrete melt pools are created and extinguished. In contrast, the continuous laser energy input remains constant as it scans, leading to the formation of a melt pool which follows the laser, solidifying continuously. The difference in the solidification behaviour leads to the difference in number and distribution of the columnar grains in the build direction.

5.1.2 Comparison of mechanical behaviour between continuous and pulsed SLM

When looking at the actual (not normalised) results from static mechanical testing it is difficult to conclude if continuous or pulsed SLM provides stronger mechanical properties as both sample groups have different relative densities. However when looking at the normalised results of the static compression tests to 0.30 relative density it appears that the mechanical properties of both techniques are different. The yield strength for 0.30 normalised continuous and pulsed SLM are 53 and 67 MPa, respectively. The only significant differences are: i) the elastic gradient, which is 1.28 GPa for continuous and 2.08 GPa for pulsed SLM and ii) the plateau stress which is 65 MPa for continuous and 44 MPa for pulsed SLM. The first max stress is almost identical. As previously mentioned this calculation is highly dependent on the accuracy of determining the relative density of the samples. At the end of the SLM print process the samples are usually removed manually from the support structure. In this procedure the bottom flat surface gets damaged as some nodes at the bottom ends break off (figure 64). The absence of material at these locations may cause minor variations in relative density. The second inaccuracy is that the use of 4.43 g/cm^3 density from the solid wrought Ti6Al4V, which might deviate for the SLM manufactured Ti6Al4V (subject to confirmation in the follow up study). For example internal pores induced by the SLM manufacturing process are not accounted for in the above specified reference density.

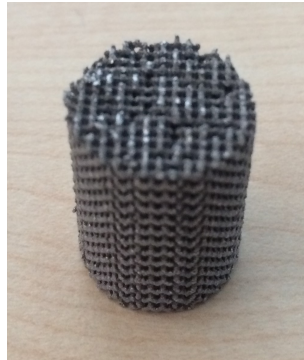


Figure 64. Damaged surface due to removal from print bed

In fatigue the continuous and the pulsed SLM samples were normalised against their own yield strength. This means that the ratio between own yield strength and fatigue resistance can be compared. Continuous SLM samples show substantially better fatigue properties. It was observed that the continuous SLM samples can remain intact longer, relative to pulsed SLM, at higher stresses for both LCF and HCF (figure 54). Overall the results suggest that samples manufactured with continuous SLM are superior to pulsed SLM. It should also be noted, that in the normalisation used herein the accuracy of the determined yield strength is of high importance. The scatter in the determined yield strength results (Table 9) was not high and hence results could be considered accurate, though as the yield strength was determined by 3 samples, the accuracy could be improved further by adding more samples. Looking at normalised fatigue results, it should be noted the method of local stress normalisation might not be accurate for pulsed SLM. As can be seen in Figure 65, the location of max local stress and thus failure, differs for continuous and pulsed SLM, which is related to the fundamental difference in the nature of the two processes (see figure 63) In the model used herein (based on calculation model of Hooreweder *et al* [22]) the stress concentration is calculated to be at the nodes (or struts interconnections), whereas for the pulsed SLM the failure location is in between built layers or weld beads. Hence, for the pulsed SLM samples the normalised to strut thickness used in the current study does not agree with the failure locations observed in figure 65. In pulsed SLM due to the rapid cooling time, the previous layer is decreased in temperature and solidified when the next layer is to be melted [17]. The previous layer is then only partially remelted when the next layer is pulsed. Therefore at the edge of the new layer an inlet can be observed which acts as a stress concentration area [8].

Non the less in figure 55 the normalised to local stress results of the pulsed samples are shown. As the failure of pulsed samples is in between the layer, the stress concentration was higher in this location. This means that the actual local stress is expected to be lower than what is displayed in the figure 55. Hence, it is expected that continuous SLM is more fatigue resistant

when normalised to strut thickness.

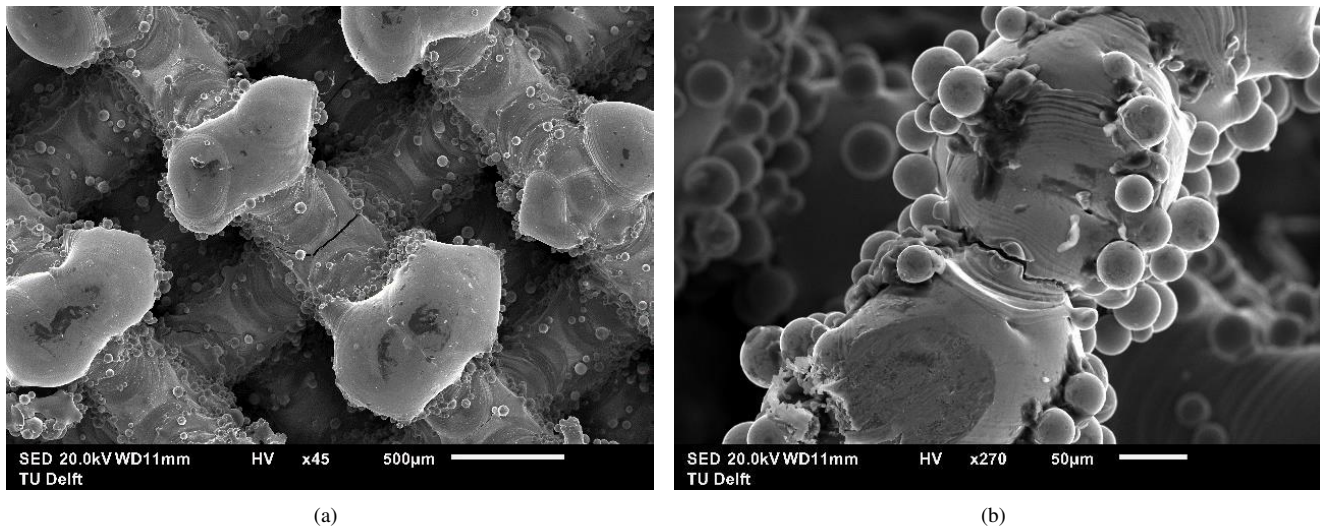


Figure 65. Figures regarding : (a) Crack location for continuous SLM at the node (b) Crack location pulsed SLM between built layers [8]

5.1.3 The effects of post process treatments

5.1.3.1 Hot Isostatic Pressing (HIP)

The effect of HIP treatment show that the internal porosity was substantially reduced, for example in the case of continuous SLM samples the reduction was 91 %. Hence nearly fully dense (99.9 %) Ti6Al4V metamaterial can be obtained following HIP treatment. Furthermore the HIP treatment transformed the Ti6Al4V from the brittle α' martensitic phase to a combination of $\alpha+\beta$ grains. A decrease the Vickers hardness was measured for the HIP treated samples, suggesting an increase in ductility. According to the results from mechanical testing it is shown that HIP treatment significantly increases all static mechanical properties: (i) yield strength was increased from 89 MPa up to 115 MPa; (ii) the Young's modulus was increased from 2.84 up to 2.89 GP; (iii) the strain up to the 1st max stress was increased from 0.057 up to 0.093 mm/mm (for continuous SLM). Hence one of the main factors in improving the static mechanical properties can be considered the phase transformation. In compression fatigue, the HIP treatment was also found to have a very significant effect. In all fatigue graphs both regular and normalised it can be observed that HIP treatment improves the fatigue resistance (figure 53, 54 and 56).

5.1.3.2 Surface Treatments

Using the SEM images it was shown that the effect of sand blasting (SB) significantly reduces the amount of partially melted particles stuck to the surface. Furthermore it was shown that SB reduces the relative density. It should however be noted that SB effect in not fully homogeneous throughout the cross section of the cylindrical samples, as the core is less effected than the areas closer to the surface.

The static mechanical properties are not changed significantly by SB, although the material is reduced in weight by approximately 0.03 relative density and this was not accounted for. The work of Ahmadi *et al* [5] shows that the relative density has a significant effect on the mechanical properties (figure 5). When a HIP treatments was applied prior to the SB the yield strength is lowered significantly, as are all mechanical properties. This could further be related to the reduction in relative density following surface treatment.

However, when normalised to the same relative density as is shown in figure 52, sand blasting has a significant effect as it improves all static mechanical properties. This suggest that indeed the surface sand blasting is beneficial for static properties,

even though it reduced the density (reduces the struts thickness). The HIP samples, normalised to the same relative density as AP samples also showed significantly improved mechanical properties. In particular the first max stress was increased from 85 to 116 MPa and the plateau stress where increased from 67 to 90 MPa. The HIP CE1 sample group showed no increase in static mechanical properties. However the normalisation for the HIP SB+CE2 group showed the best overall mechanical properties when normalised to the same relative density.

In terms of fatigue resistance for AP samples, both in regular and yield strength normalised S-N curves (figure 53 and 54), the effect of SB is not significant. However in local stress S-N curve the result show an increase in fatigue resistance (figure 56). This suggest that SB does work on the local stress fatigue level and that if the relative density were to be equal to the relative density of an AP sample a change could be observed in the regular fatigue graphs as well.

For the HIP+SB samples the opposite is true. SB has pronounced effects on the fatigue resistance in normal fatigue and in relative to its yield strength, however normalised to its relative density the fatigue resistance is not significantly improved. This indicates that the materials transformation from the brittle α' -phase to the more ductile $\alpha + \beta$ -phase, effects the interaction with abrasive Al_2O_3 particles. Perhaps the response of the more brittle material to blast particles is to crumble, whereas the more ductile material compresses more inwards. Hence X-ray diffraction could be applied to measure the residual surface stress after SB for both AP and HIP samples.

Overall it can be concluded that sand blasting on AP and HIP samples increases the fatigue resistance and decreases the static mechanical properties but also decreases the relative density. As mentioned before with the normalisation to relative density, it is very important to determine the relative density accurately whereby the damaged surface was not taken into account.

Chemical etching in general was found to reduce the amount of partially melted particles stuck to the surface in a similar fashion as sand blasting does, which is also shown in the relative density measurements (figure 46). Furthermore CE removes the residual Al_2O_3 particles coming from SB, as is shown in appendix B with an EDS analysis. It also be noted, the a combination of HIP+CE1 negatively effects the static mechanical properties more than HIP+SB, as the residual stresses at the surface are not induced and more material removal is observed. For example, the yield strength is lowered from 115 MPa for HIP only to 87 MPa for HIP SB+CE2. In fatigue, chemical etching does not improve the fatigue resistance in the regular graph as it is not accounted for relative density. Normalised to the yield strength the effect of etching on the fatigue resistance in significant. This suggests that the removal of particles (and thus local points of stress concentrations) successfully improved the fatigue resistance. Finally normalised to its relative density an increase in fatigue resistance at the local level was observed. Treatment of SB+CE2 showed an almost complete removal of particles stuck to the surface in the SEM images (figure 44), which is beneficial for cell ingrowth and osteointegration. Even though the combined effect of HIP+SB+CE2 weakened the static mechanical properties, the normalised fatigue (to its yield strength) showed an increase. Finally in the normalisation to the local stress this particular treatment (HIP+SB+CE2) seems to be superior from all investigated herein groups, as it can withstand fatigue well while featuring great reduction in the relative density. Thus, if all samples had the exact same relative density the HIP+SB+CE2 post process treatment would be the best.

When looking at the shape of the struts after SB or CE treatment it can be noticed that near the node they are thicker than at the centre of the strut. As all struts are critically loaded in bending it is mechanically very favourable for the strut to have this post process induced concave shape. Hence, weight it reduced by removing material at locations that are not the most critical.

5.1.4 Normalisation methods of dynamic properties of lattice Ti6Al4V

Normalisation to yield strength and normalisation to strut thickness (designated here as local stress approach) have been applied on the compression fatigue results. To check the validity of the yield strength normalisation and the local stress normalisation two AP sample groups were tested at different relative densities of 0.26 and 0.37 (figure 66).

For local stress normalisation if these S-N curves align, it would verify the validity of these results. As can be seen in figure 66(b), the curves align relatively well and the confidence interval overlap. When comparing the current results to the results of Hooreweder *et al* [22], it can be noticed that the AP samples align better in the work of Hooreweder *et al* [22]. A possible

explanation for this increased deviation in fatigue results is that a larger gap in relative density was used for the current research (current results gap: 0.11, Hooreweder results gap: 0.03). Hereby the effect of all the factors which were not taken into account magnify. The second possibility would be that the relative density was not measured fully accurately due to the damaged top surface reported in figure 64.

For the yield strength normalisation an alignment of the two curves means that the ratio in yield strength to fatigue resistance is constant for each relative density level. As can be seen in figure 66(a) the curves align well. It should however be noted that the accuracy of this normalisation is highly dependent on the accuracy of determining the yield strength.

The results from figure 66 indicate that both methods are valid for normalisation of fatigue results. To further confirm the more sample groups must be tested at different relative density.

Finally, another combined normalisation approach can be proposed for the follow up investigation. With the local stress normalisation, essentially the material properties are calculated instead of the more mechanics related metamaterial properties. If the metamaterial yield strength is computed in this normalisation it should be possible to calculate the Ti6Al4V solid yield strength. This value could then be used to normalise the local stress fatigue values with the material yield strength. The outcome of this double normalised fatigue graph would then be the pure Ti6Al4V solid material ratio between yield strength and fatigue resistance. Doing this new type of normalisation (scope of a follow up study) for all materials would result in another method of comparison between different heat treatments and surface modifications.

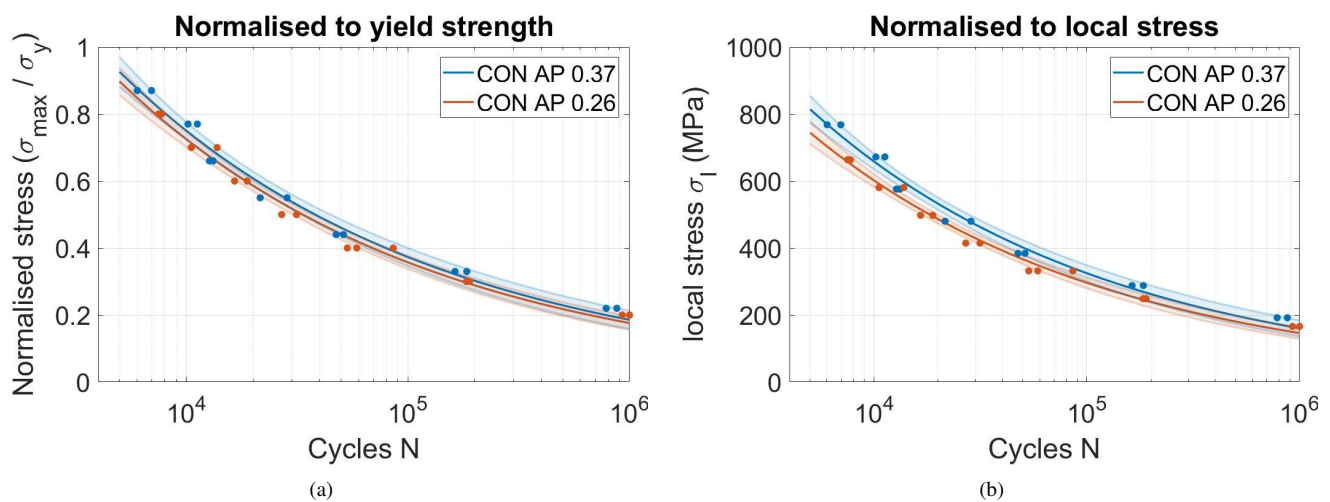


Figure 66. Comparison of the effectiveness of normalisation for : (a) yield strength normalisation (b) local stress normalisation

5.2 Mechanical behaviour of spinal cage implants

5.2.1 Mechanical properties

Static and dynamic compression tests were performed according to the ASTM F2077 standard on Ti6Al4V spinal cage implants manufactured by SLM.

The main differences in static mechanical properties between the AP and the HIP+SB+CE samples are: (i) the change in yield force from 17748 N for AP to 15558 N for HIP+SB+CE and (ii) the displacement up to 1st max force from 0.040 to 0.051 mm/mm. The decrease in yield force is likely caused by to the addition of polishing and sandblasting of the imlant. The combination of both effects might have cancelled out the positive effect of HIP treatment. The increase in 1st max displacement is probably due to the increase in ductility (result of phase transformations previously discussed) induced by the HIP treatment.

In regular fatigue the HIP+SB+CE was slightly higher although the confidence intervals overlapped. The HIP+SB+CE samples do however have a lower relative density. In normalised fatigue (to its own yield force) the effect of HIP+SB+CE is

more significant as the confidence intervals overlap much less. Ahmadi *et al* [4] showed that sandblasting induces compressive surface stresses. Figure 48 shows that sand blasting did not reach the core of the implant. It is likely that in the core SB instead acts as crack initiation location, as it does not uniformly treats the surface.

It should also be noted that the end of test criteria at 2 mm displacement used in implant testing is debatable. The ASTM F2077 [40] describes the end of test limit as permanent deformation whereby the implant is no longer effective or able to resist force or maintain attachment adequately. As is shown in figure 59 and 67, the lattice structure is already experiencing the critical fatigue crack growth and crumbling significantly earlier than the 2 mm displacement. Furthermore by assessing the samples after the fatigue tests it could be noticed that in the critical area the lattice structure was completely destroyed, suggesting that the solid part of the sample became completely load bearing. An argument could be made that the crumbling should already be considered as critical failure for the reason as it would be unfavourable to have it in the human body (hence actual application of the tested implants).

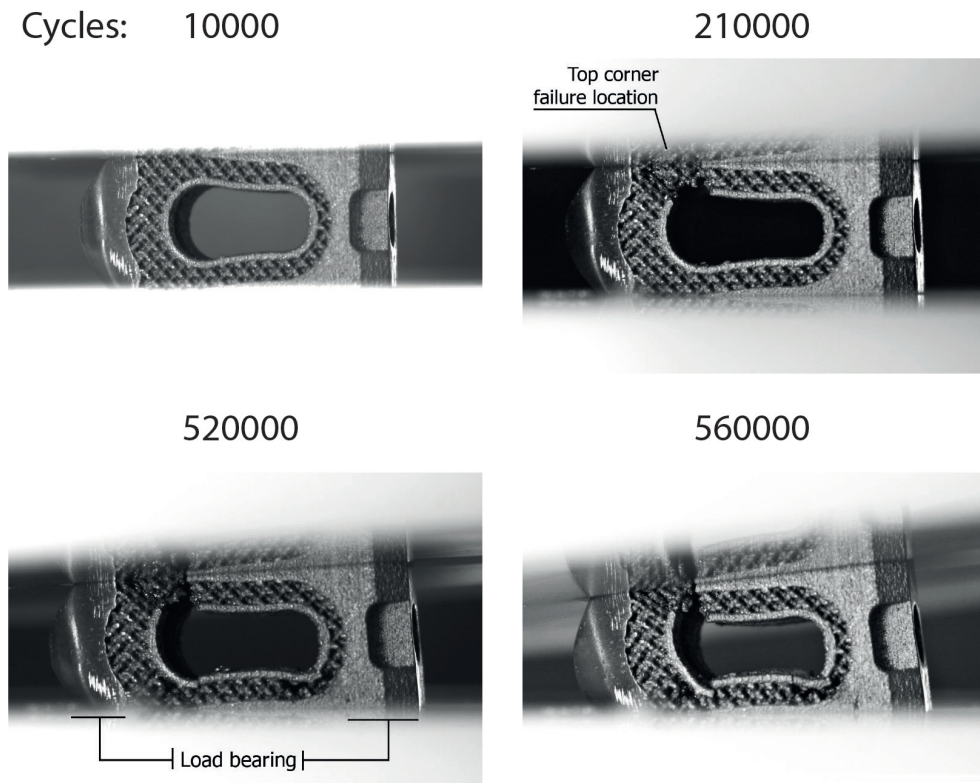


Figure 67. Representative HIP SB+CE implant sample for indication failure locations loaded at 4,7 kN

5.2.2 Design assessment

In this section the design of the lumbar (spinal cage) implant will be discussed, regardless of the surface or heat treatments. In static compression the weak spot of the lumbar cage implant design was found to be the threaded hole (figure 68). As a result of material removal this particular cross section becomes the most affected (thus with the least amount of material). Hence as the stress is calculated by dividing the force over the area, the smallest cross section area will always feel the highest stress. Perhaps the size of the bolt could be lowered to improve compression strength.

In fatigue testing the critical area was always found to be located at the top corner of the porous structure, as is shown in figure 67. It is thus could be recommended to increase the strength in this particular area. However the strength must not be increased to a degree that stress shielding is occurring. Perhaps a follow up study could be done on the compression stiffness of a solid cage and the effectiveness of the porous section could be proven with regards to reducing to stress shielding effect.

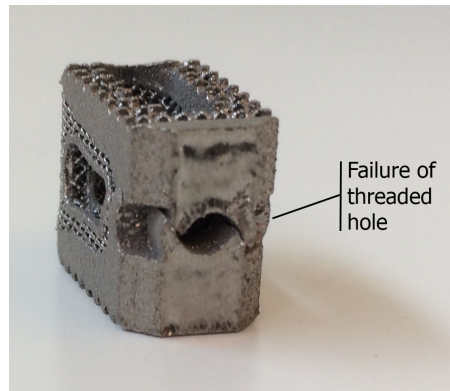


Figure 68. The compressed cage failing location

When considering the fatigue of the lumbar cages, it was observed that the POM (Polyoxymethylene) plates always tilted after only a few cycles, whereas it was rather perfectly aligned in the beginning of the test. As is shown in figure 69 the back has no remaining teeth imprints in place whereas the teeth sink into the POM material, hence after only a few cycles the plate will start to tilt. Hence an improvement in design of both implants and POM could be made to allow teeth sinking and thus uniform sample and POM plates alignment at this section.

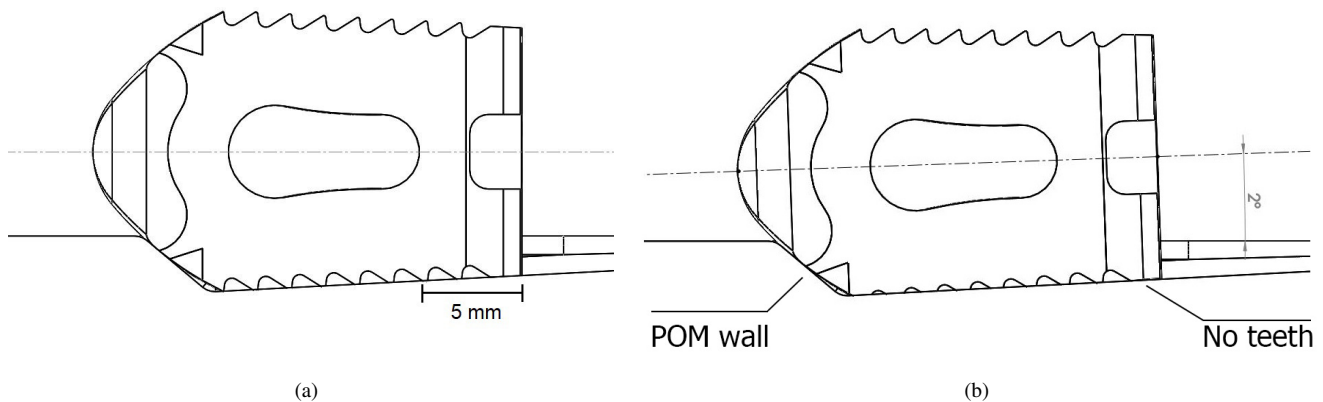


Figure 69. Figures regarding (a) implant to POM block interface before load is applied (b) implant to POM block interface after load is applied and subsidence occurred.

5.2.3 Accuracy of testing

The ASTM F2077 is a rather complicated test and a lot of improvements could be suggested to increase its accuracy:

- For the compression testing it was chosen to work with cross head extensometers (hence displacement of the entire setup), which is likely not fully accurate. An even more accurate measurement could be made using Digital Image Correlation (DIC), which is capable of measurement local displacement on the tested sample.
- The tests were performed on a 250 kN load cell which reduced the accuracy quite a bit as the forces reached in this research are in the range of 15-20 kN. Using a 30 kN load cell would give more accurate results.
- In compression fatigue there is a very large scatter in data points. One possible cause is the misalignment for each sample. The pocket inside the POM blocks did not have the perfect fitting width. A second cause could be the tilt of the plates. For each sample in the beginning of the fatigue test the POM plates would slightly tilt 69(b). The probable cause of this

is the absence of teeth at the end of the sample. This could enlarge the miss-alignment error of the sample. As a different in placement would also lead to a difference in tilt of the POM plate. However the difference in alignment can only be very small as the set-up was designed to aim the force directly at the centre of the sample using the length of the pushrod. As has been shown in figure 31, a miss-alignment would only change the angle by a small amount.

Another possible cause could be the surface shape of both the AP sample and the HIP+SB+CE implants. For AP implants, random strut was observed sticking out near the critical area. At the first compression a great portion of the load is taken by these struts, which could potentially cause a defect in this location. For the HIP+SB+CE implants, surface was manually polished, thus reducing above mentioned in AP implants inhomogeneity. This could also mean that by human error some samples might have been damaged critically.

- Some samples were stopped halfway through the fatigue tests because the machine gave an error message due to overheating. One could argue that this does not affect the sample, but still it is an irregularity that has to be reported.
- A final improvement in accuracy could be made in the design of the POM blocks. It was initially chosen to cage in the sample in four plane directions as it could not vibrate out of centre due to the POM block holding it in place. However this does not perfectly simulate the actual situation. Some test could be done to try out if the test could also be performed with a POM block more accurately resembling the vertebra surface. Furthermore, in particular the POM wall (figure 69(b)) at the front side of the implant could be eliminated as it significantly changes the stress situation. Some load is now also subjected to the head of the implant which otherwise would only be on the teeth surface.

5.3 Wettability

5.3.1 General observations

In general when looking at the Dip testing the trend seem to be that sand blasting treatment improves wettability and both chemical etching treatments decrease wettability. The contact angle measurements show the same trend, however to a much lesser significant degree. With Tukey's test it was proven that AP+CE2 and AP+SB+CE2 are statistically different and that for this case sandblasting prior to chemical etching effectively decreases the contact angle from 88° to 76°. A trend can be observed that this is the case for all SB samples as the measured mean is always lower than it is for the non-sandblasted equivalent. For the AP and the AP+SB sample the contact angle mean decreases from 64° to 62°. This is however not in line with the observation made by strnad *et al* [36]. Here it was observed that SB increased the contact angle substantially. Perhaps this is due the difference in abrasive particle size: 250 - 300 μm used by strnad *et al* [36], compared to the 50 μm used in the current work. Larger particle size results in large impacts on the surface and hence larger micro peaks and valleys are created. An increase in contact angle therefore suggests that in their research the droplets experienced the Cassie-Baxter state, where oxygen is trapped inside the mirco valleys of the surface decreasing the contact area. Whereas in the current research the 50 mm SB particles resulted in the Wenzel state. To statistically prove this decrease more data points must be added to the research.

The treatment of CE2 increased the contact angle by the most significant amount as it increased the contact angle from 64° to 88°. What is furthermore interesting about this increase in contact angle is that at parts the contact angle went over the 90° suggesting a change from hydrophilic behaviour to hydrophobic behaviour. A change as such can only indicate that the surface composition has changed. Therefore the increase is possibly caused by the corrosion observed on the surface of the CE2 sample. Tukey's test showed that difference was proven between CE2 and AP samples. For CE1 an increase in contact angle was observed as well, however the change was less significant compared with CE2. Tukey's test showed that currently no difference could be proven between CE1 and AP, however more data points can be added to verify the observed trend.

The effect of chemical etching treatment, in particular of CE2, seems to increase the contact angle and is therefore potentially worse for cell adhesion and curing time of the implant surgical procedure. Sand blasting was found to decrease the contact angle and in particularly it decreases the negative effects of chemical etching. Hence SB is beneficial for cell adhesion.

It should be noted that the effect of HIP was not taken into account in the current study. However some studies show that the HIP could also have an effect on the wettability [43]. This study implies that the change in atom arrangement in the bulk

would affect the attraction at the surface through the passivation layer. A more likely effect of heat treatment is that it would induce corrosion on the surface or that it would increase the passivation layer thickness. These effects are however erasable by both sandblasting and chemical etching.

It should also be mentioned that the passivation layer was not accounted for in the current study. As soon as Ti6Al4V comes into contact with air it forms a protective passivation layer. The way and duration of the initial air contact determines the thickness of the passivation layer. After SB treatment and chemical etching, the passivation layer has to heal and in the case of chemical etching other corrosion occurred on the surface as well. Hence a study could be performed on the effect of the thickness and nature of the passivation layer.

An improvement in the accuracy could be made through optimisation of the cleaning protocol. In literature [37] the best accuracy was achieved via the addition of the ultrasonic cleaning and using the desiccator, furthermore a drying oven was used to control the passivation. This is something that could be tested in the follow up study. As the passivation would decrease the scatter and the oven drying would improve to what the desiccator also does. Controlled passivation is however a step which then in industry must be applied to the just printed parts.

5.3.2 Comparison dip with contact angle

When comparing the dip test and the Sessile drop testing, it can be noticed that the increase of hydrophilic behaviour due to sandblasting might have been less significant (due to the indication of the contact angle measurements). When comparing the solid and lattice samples the first significant difference is that the liquid used for both tests was not identical as colouring had to be applied to the dip test liquid as the visibility effect had to be increased. Furthermore demi water was used whereas for the wettability deionised water was used.

The second difference is that the solid samples which were subjected to the same treatments do not in fact have an identical surface. The metamaterials simply have more free surface. It could be that a slight change in contact angle enables it to go up into the sample.

6 Conclusions

Throughout the research the focus was towards the primary objective to investigate the biomechanical properties of additively manufactured Ti6Al4V metamaterials and implants as a functions of various post-processing treatment and additive manufacturing parameters. This research was divided into six research questions aimed to achieve the primary objective.

1. **What is the microstructural and mechanical difference between continuous and pulsed SLM Ti6Al4V metamaterial?**

As-processed, both continuous and pulsed SLM consist of the martensitic α' -phase. For the continuous SLM method the grains align with the build direction whereas for the pulsed SLM method the grains are oriented more randomly, hence Pulsed SLM has a more isotropic nature. When HIP is applied the microstructure transforms to the $(\alpha + \beta)$ -phase for both scanning methods. For the continuous SLM method, the $(\alpha + \beta)$ -phase after HIP treatment consists of smaller grains compared to the pulsed SLM method, which means a higher grain boundary density and therefore increased yield strength and fatigue resistance. In dynamic compression testing the continuous SLM method is inferior over the pulsed SLM method. It was shown that for the continuous SLM method the fatigue resistance relative to its yield strength was substantially higher than for the pulsed SLM method. This is partially due to the higher grain boundary density and the difference in defect generation between continuous and pulsed SLM.

2. **How does the hot isostatic pressing (HIP) effect the properties of Ti6Al4V lattice structures?**

HIP treatment changes the as-processed α' microstructure to a preferred mixed of $\alpha + \beta$. Furthermore, HIP was found to substantially reduce unintended process-induced internal porosity (ranging from 0.6 to 2 %), resulting in 99.9 % dense material. In terms of mechanical response HIP increases ductility, yield stress, first maximum stress and plateau stress of the SLMed materials. In fatigue the reduction in porosity and the phase transformation increases the fatigue resistance both in LCF and HCF.

3. **Can surface modifications in terms of sand blasting (SB) and chemical etching (CE) be optimized and what is their effect of the mechanical properties of SLMed lattice Ti6Al4V?**

Sand blasting induces compressive surface residual stress and removes partially melted particles attached to the surface, hereby reducing possible areas of stress concentrations. Even though sand blasting expectedly does not give any effect of the static properties, it does contribute to the improvement of the dynamic properties. Sand blasting was found most affective in combination with HIP and continuous laser SLM. Chemical etching was found to fully remove partially melted particles on the surface however it has a limited effect in the sample core. The combined effect of HIP and CE1 showed an increase in fatigue resistance similar to HIP SB. The triple effect of HIP+SB+CE2 removes the most particles stuck to the surface and it also reaches the core of the cylindrical samples. The triple effect was found most effective surface modification as it significantly increases fatigue resistance. It should also be noted, that HIP+SB+CE removes all remaining sand blasting debris, while inducing preferred for osseointegration micro scale roughness.

4. **Can static and dynamic mechanical data of various groups of Ti6Al4V metamaterials be normalised with respect to the yield strength and the local stress?**

Normalisation with respect to yield stress showed that the most effect post process treatments were the HIP SB and HIP CE1. Even though this method does not account for strut thickness, it shows a ratio between a materials yield strength and its fatigue resistance, which is an interesting parameter for application of the material. Normalisation with respect to local stress was found to represent most accurately the dynamic data of continuous SLM. Normalisation with respect to local stress showed the most effective way of post process treatments is HIP SB+CE2. It should be noted that some improvement could be made for data normalisation, as will be discussed in recommendation section. The current local stress normalisation method was found less effective for the pulsed SLM as these samples show failure location in beads

overlaps, which is different with the normalisation assumption of failure location within the struts interconnection (as is the case with continuous SLM).

5. Can the developed herein post processing be upscaled to the actual implants and what would the mechanical response of such implants be?

The most effective for cylindrical lattice samples post-process treatment of HIP+SB+CE was applied on full scale spinal cage implants. The static mechanical response showed a decrease in the yield force and increase in the ductility of the implant. In static mechanical testing the failure location was found within the threaded hole which represents the lowest cross sectional area in the implant's design. The dynamical response of implants was improved after the application of HIP+SB+CE post treatment. Thus developed herein post process procedure was successfully upscaled. There were however critical failure locations identified in the top section of the porous part of the implant, indicating the procedure could be more effective with improved/modified implant design.

6. What is the effect of the surface modifications on the wettability behaviour?

Sand blasting surface treatment was found to decrease most the contact angle and hence can be considered as the most beneficial for cell adhesion and osseointegration. Both chemical etching methods used in this study showed to be less effective in decreasing the contact angle. This is likely due to different elemental composition of the surface resulting from corrosion products. The effect of SB prior to both CE methods was found to decrease the contact angle and is a good method of reducing the negative CE effect on the cell adhesion and osseointegration.

7 Recommendations

Mechanical testing of cylindrical samples

- Cylindrical sample mechanical testing could be fully completed by adding a group of APCE1 and or APCE2. It should however be noted that these treatment will not affect process-induced porosity and hence likely will not give a substantial effect.
- The order in which SB CE and HIP are applied could also affect the resulting mechanical properties. For example in the current research CE is applied after SB. The induced residual surface stresses from the SB could potentially be erased by the latter CE treatment. An X-ray diffraction study could be performed to determine the residual stresses of SB and SB CE samples to see if this is the case.
- As the model described by Hooreweder et al [12] (used here as local stress normalisation) did not perfectly fit the current research it is advised that a critical look is taken at the current method of determining the relative density. Perhaps an improvement can be made in cutting off the damaged top section or using Electro Discharge Machining for removal of SLM parts. For pulsed SLM a modified model can be established to determine the stress concentration at the weld beads.
- The current research indicated that SB is more effective on improving HIP samples than it is on improving AP samples. Perhaps a comparison could be made and it could be investigated why this is the case.
- The surface modification of electro polishing could be looked into as another alternative to treat the surface of the lattice structured Ti6Al4V samples.

Mechanical testing of spinal cage implants

- As the current research showed limited improvement by the post process treatments perhaps the effect of SB on the implant can be analysed better. Due to the complex geometry the SB was not applied uniformly on the implants. It could be the case that instead of inducing residual surface stress on the complete surface, the impacts of the SB particles created a surface defect. This defect could act as a stress concentration location and crack initiation could occur here. In this regard CE might be a better option to surface modify actual implants as it could possibly cover the surface better and more evenly than the SB treatment.
- The applied implant's polishing modifications could be investigated more profoundly as there is an indication it might affect the outcome of the mechanical testing.
- The current compression fatigue data of the spinal cage implants has a large scatter and it is only tested in the HCF region. Perhaps more data points can be added to increase the accuracy of the results. The scatter is quite large as well and perhaps a method can be found to reduce the scatter.

Wettability

- As mentioned before the amount of data point could be increased to prove that the mean of all groups are statistically different from each other.
- In literature it was mentioned that heat treatments effect the contact angle as well. Therefore HIP samples could be added to the current set of data in the wettability research.
- A follow up in vitro study could be performed to assess the actual effects of the cell adhesion for the SB, CE1 and CE2 surfaces.
- In the current study the cylindrical samples were processed the way they would be for implant usage. This way the effect of passivation is not taken into account. A follow-up study could be performed to see if controlled passivation might affect the wettability behaviour.

References

1. S. Ahmadi, R. Hedayati, R. A. K. Jain, Y. Li, S. Leeflang, and A. Zadpoor, "Effects of laser processing parameters on the mechanical properties, topology, and microstructure of additively manufactured porous metallic biomaterials: A vector-based approach," *Materials & Design*, vol. 134, pp. 234–243, 2017.
2. S. Ahmadi, R. Hedayati, Y. Li, K. Lietaert, N. Tümer, A. Fatemi, C. Rans, B. Pouran, H. Weinans, and A. Zadpoor, "Fatigue performance of additively manufactured meta-biomaterials: The effects of topology and material type," *Acta biomaterialia*, vol. 65, pp. 292–304, 2018.
3. M. Brandt, "The role of lasers in additive manufacturing," *Laser Additive Manufacturing: Materials, Design, Technologies, and Applications*, p. 1, 2016.
4. S. Ahmadi, R. Kumar, E. Borisov, R. Petrov, S. Leeflang, Y. Li, N. Tümer, R. Huizenga, C. Ayas, A. Zadpoor, and V. Popovich, "From microstructural design to surface engineering: A tailored approach for improving fatigue life of additively manufactured meta-biomaterials," *Acta biomaterialia*, vol. 83, pp. 153–166, 2018.
5. S. M. Ahmadi, S. A. Yavari, R. Wauthle, B. Pouran, J. Schrooten, H. Weinans, and A. A. Zadpoor, "Additively manufactured open-cell porous biomaterials made from six different space-filling unit cells: The mechanical and morphological properties," *Materials*, vol. 8, no. 4, pp. 1871–1896, 2015.
6. H. Shipley, D. McDonnell, M. Culleton, R. Lupoi, G. O'Donnell, and D. Trimble, "Optimisation of process parameters to address fundamental challenges during selective laser melting of ti-6al-4v: A review," *International Journal of Machine Tools and Manufacture*, vol. 128, pp. 1–20, 2018.
7. J.-P. Kruth, P. Mercelis, J. Van Vaerenbergh, L. Froyen, and M. Rombouts, "Binding mechanisms in selective laser sintering and selective laser melting," *Rapid prototyping journal*, vol. 11, no. 1, pp. 26–36, 2005.
8. R. Jain Kumar Ashok Kumar, "Influence of post-processing on ti6al4v lattice structures produced by selective laser melting," Master's thesis, Delft University of Technology, 2017.
9. D. Agius, K. Kourousis, and C. Wallbrink, "A review of the as-built slm ti-6al-4v mechanical properties towards achieving fatigue resistant designs," *Metals*, vol. 8, no. 1, p. 75, 2018.
10. C. Elias, J. Lima, R. Valiev, and M. Meyers, "Biomedical applications of titanium and its alloys," *Jom*, vol. 60, no. 3, pp. 46–49, 2008.
11. R. Pederson, "Microstructure and phase transformation of ti-6al-4v," Ph.D. dissertation, Luleå tekniska universitet, 2002.
12. I. Standard, "Iso 13314: 2011 (e)(2011) mechanical testing of metals—ductility testing—compression test for porous and cellular metals," *Ref Number ISO*, vol. 13314, no. 13314, pp. 1–7, 2011.
13. S. Ahmadi, R. A. K. Jain, A. Zadpoor, C. Ayas, and V. Popovich, "Effects of heat treatment on microstructure and mechanical behaviour of additive manufactured porous ti6al4v," in *IOP Conference Series: Materials Science and Engineering*, vol. 293, no. 1. IOP Publishing, 2017, p. 012009.
14. G. Kasperovich and J. Hausmann, "Improvement of fatigue resistance and ductility of tial6v4 processed by selective laser melting," *Journal of Materials Processing Technology*, vol. 220, pp. 202–214, 2015.
15. A. R. Nassar and E. W. Reutzel, "Additive manufacturing of ti-6al-4v using a pulsed laser beam," *Metallurgical and Materials Transactions A*, vol. 46, no. 6, pp. 2781–2789, 2015.
16. G. Ravi, C. Qiu, and M. M. Attallah, "Microstructural control in a ti-based alloy by changing laser processing mode and power during direct laser deposition," *Materials Letters*, vol. 179, pp. 104–108, 2016.
17. S. Li, H. Xiao, K. Liu, W. Xiao, Y. Li, X. Han, J. Mazumder, and L. Song, "Melt-pool motion, temperature variation and dendritic morphology of inconel 718 during pulsed-and continuous-wave laser additive manufacturing: A comparative study," *Materials & Design*, vol. 119, pp. 351–360, 2017.

18. N. Loh and K. Sia, "An overview of hot isostatic pressing," *Journal of Materials Processing Technology*, vol. 30, no. 1, pp. 45–65, 1992.
19. Y. Murakami and M. Endo, "Effects of defects, inclusions and inhomogeneities on fatigue strength," *International journal of fatigue*, vol. 16, no. 3, pp. 163–182, 1994.
20. Y. Zhang, J. Li, and S. Che, "Electropolishing mechanism of ti-6al-4v alloy fabricated by selective laser melting," *International journal of electrochemical science*, vol. 13, no. 5, pp. 4792–4807, 2018.
21. G. Pyka, A. Burakowski, G. Kerckhofs, M. Moesen, S. Van Bael, J. Schrooten, and M. Wevers, "Surface modification of ti6al4v open porous structures produced by additive manufacturing," *Advanced Engineering Materials*, vol. 14, no. 6, pp. 363–370, 2012.
22. B. Van Hooreweder, Y. Apers, K. Lietaert, and J.-P. Kruth, "Improving the fatigue performance of porous metallic biomaterials produced by selective laser melting," *Acta biomaterialia*, vol. 47, pp. 193–202, 2017.
23. Y. Liu, H. Wang, S. Li, S. Wang, W. Wang, W. Hou, Y. Hao, R. Yang, and L. Zhang, "Compressive and fatigue behavior of beta-type titanium porous structures fabricated by electron beam melting," *Acta Materialia*, vol. 126, pp. 58–66, 2017.
24. S. A. Yavari, R. Wauthlé, J. van der Stok, A. Riemslog, M. Janssen, M. Mulier, J.-P. Kruth, J. Schrooten, H. Weinans, and A. A. Zadpoor, "Fatigue behavior of porous biomaterials manufactured using selective laser melting," *Materials Science and Engineering: C*, vol. 33, no. 8, pp. 4849–4858, 2013.
25. S. A. Yavari, S. Ahmadi, R. Wauthle, B. Pouran, J. Schrooten, H. Weinans, and A. Zadpoor, "Relationship between unit cell type and porosity and the fatigue behavior of selective laser melted meta-biomaterials," *Journal of the mechanical behavior of biomedical materials*, vol. 43, pp. 91–100, 2015.
26. M. Jäger, H. P. Jennissen, F. Dittrich, A. Fischer, and H. L. Köhling, "Antimicrobial and osseointegration properties of nanostructured titanium orthopaedic implants," *Materials*, vol. 10, no. 11, p. 1302, 2017.
27. F. Namavar and R. F. Sabirianov, "Why is titanium biocompatible?" conference poster, 2012.
28. J. W. Kuiper, R. T. Willink, D. J. F. Moojen, M. P. van den Bekerom, and S. Colen, "Treatment of acute periprosthetic infections with prosthesis retention: review of current concepts," *World journal of orthopedics*, vol. 5, no. 5, p. 667, 2014.
29. S. Pal, "Mechanical properties of biological materials," in *Design of Artificial Human Joints & Organs*. Springer, 2014, pp. 23–40.
30. F. Rupp, R. A. Gittens, L. Scheideler, A. Marmur, B. D. Boyan, Z. Schwartz, and J. Geis-Gerstorfer, "A review on the wettability of dental implant surfaces i: theoretical and experimental aspects," *Acta biomaterialia*, vol. 10, no. 7, pp. 2894–2906, 2014.
31. Y. Yuan and T. R. Lee, "Contact angle and wetting properties," in *Surface science techniques*. Springer, 2013, pp. 3–34.
32. A. Cassie and S. Baxter, "Wettability of porous surfaces," *Transactions of the Faraday society*, vol. 40, pp. 546–551, 1944.
33. H. Gu, C. Wang, S. Gong, Y. Mei, H. Li, and W. Ma, "Investigation on contact angle measurement methods and wettability transition of porous surfaces," *Surface and Coatings Technology*, vol. 292, pp. 72–77, 2016.
34. C. Zhang, W. Zhou, Q. Wang, H. Wang, Y. Tang, and K. Hui, "Comparison of static contact angle of various metal foams and porous copper fiber sintered sheet," *Applied Surface Science*, vol. 276, pp. 377–382, 2013.
35. M. Guilizzoni, "Drop shape visualization and contact angle measurement on curved surfaces," *Journal of colloid and interface science*, vol. 364, no. 1, pp. 230–236, 2011.
36. G. Strnad, N. Chirila, C. Petrovan, and O. Russu, "Contact angle measurement on medical implant titanium based biomaterials," *Procedia Technology*, vol. 22, pp. 946–953, 2016.

37. M. Hierro-Oliva, A. M. Gallardo-Moreno, A. Rodríguez-Cano, J. M. Bruque, and M. L. González-Martín, "Experimental approach towards the water contact angle value on the biomaterial alloy ti6al4v," *Annales UMCS, Chemia*, vol. 70, no. 1, pp. 1–13, 2015.
38. S. Van Bael, Y. C. Chai, S. Truscetto, M. Moesen, G. Kerckhofs, H. Van Oosterwyck, J.-P. Kruth, and J. Schrooten, "The effect of pore geometry on the in vitro biological behavior of human periosteum-derived cells seeded on selective laser-melted ti6al4v bone scaffolds," *Acta biomaterialia*, vol. 8, no. 7, pp. 2824–2834, 2012.
39. E. Friis, P. Arnold, and V. Goel, "Mechanical testing of cervical, thoracolumbar, and lumbar spine implants," in *Mechanical Testing of Orthopaedic Implants*. Elsevier, 2017, pp. 161–180.
40. A. Standard, "Astm f2077 - 18 test methods for intervertebral body fusion devices," *Ref Number ASTM*, vol. F2077, no. F2077, pp. 1–10, 2018.
41. W. E. Frazier, "Metal additive manufacturing: a review," *Journal of Materials Engineering and Performance*, vol. 23, no. 6, pp. 1917–1928, 2014.
42. M. Masoomi, S. M. Thompson, and N. Shamsaei, "Laser powder bed fusion of ti-6al-4v parts: Thermal modeling and mechanical implications," *International Journal of Machine Tools and Manufacture*, vol. 118, pp. 73–90, 2017.
43. M. Wang, Y. Wu, S. Lu, T. Chen, Y. Zhao, H. Chen, and Z. Tang, "Fabrication and characterization of selective laser melting printed ti-6al-4v alloys subjected to heat treatment for customized implants design," *Progress in Natural Science: Materials International*, vol. 26, no. 6, pp. 671–677, 2016.

Appendices

A SB optimisation

Table 13. Table of the sandblasting parameters used to optimise the SB procedure (all samples were subjected to a rotation speed 20 RPM)

	Pulsed SLM	Continuous SLM
180 μm powder	3 bar – 90 s	3 bar – 90 s
	4.5 bar – 90 s	3 bar – 180s 4.5 bar – 90 s
50 μm powder	3 bar – 90 s	3 bar – 90 s
	4.5 bar – 90 s	4.5 bar – 90 s 6.5 bar – 10 min
12 μm powder	-	4.5 bar – 90 s

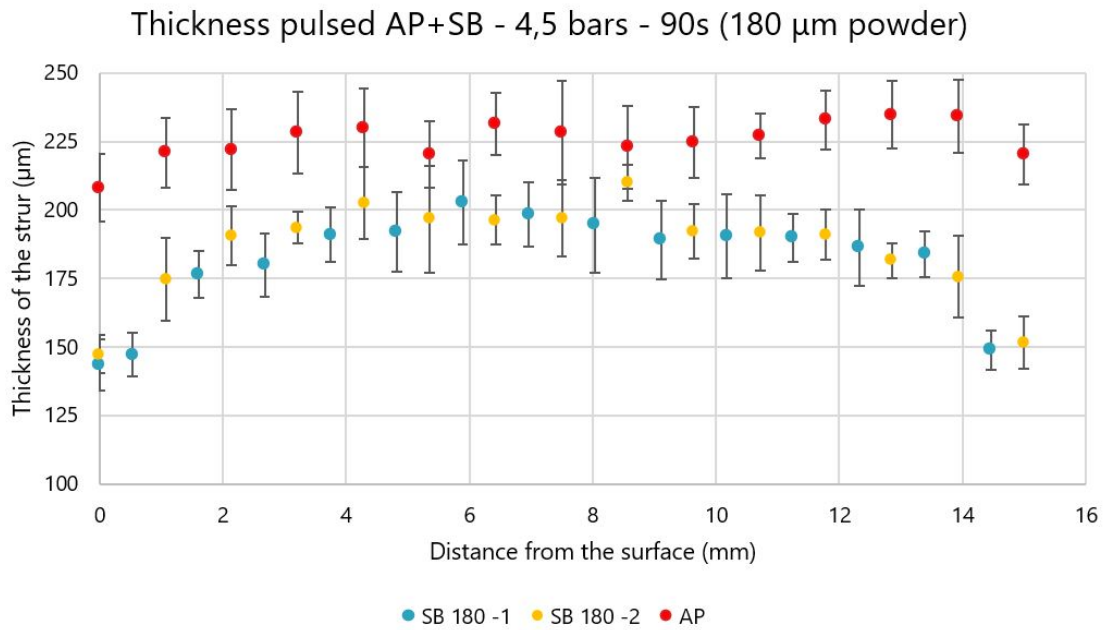


Figure 70. Strut thickness measurement of pulsed AP+SB 4.5 bars 90 seconds with 180 μm powder compared with pulsed AP

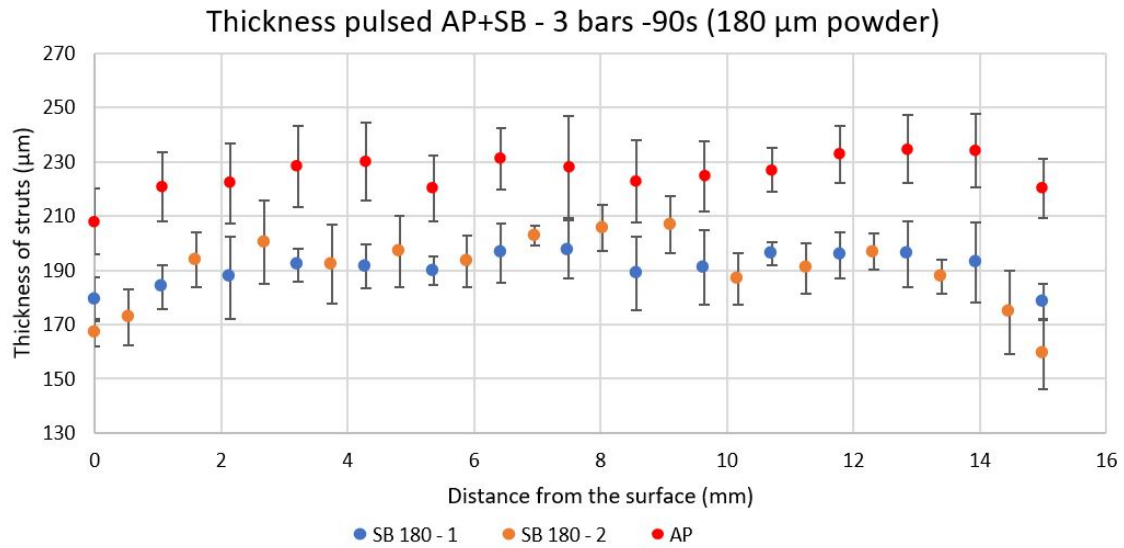


Figure 71. Struts thickness measurement of pulsed AP+SB 3 bars 90 seconds with 180 μm powder compared with pulsed AP

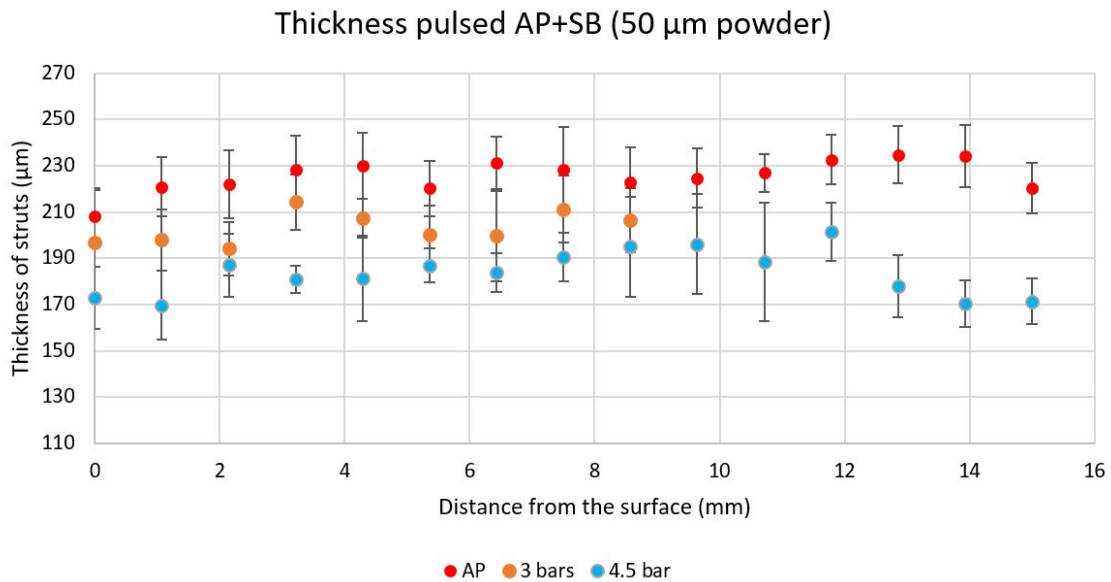


Figure 72. Struts thickness measurement of Pulsed AP+SB 4.5 bars and 3 bars 90 seconds with 50 μm powder compared with pulsed AP

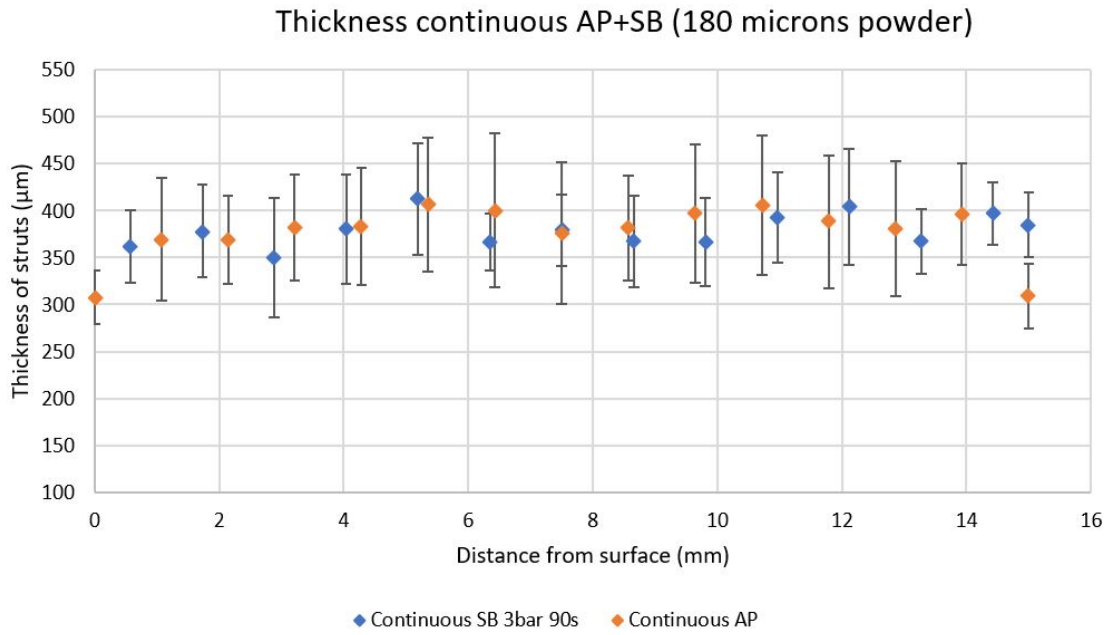


Figure 73. Strut thickness measurement of continuous AP+SB 3 bars 90 seconds with 180 μm powder compared with continuous AP

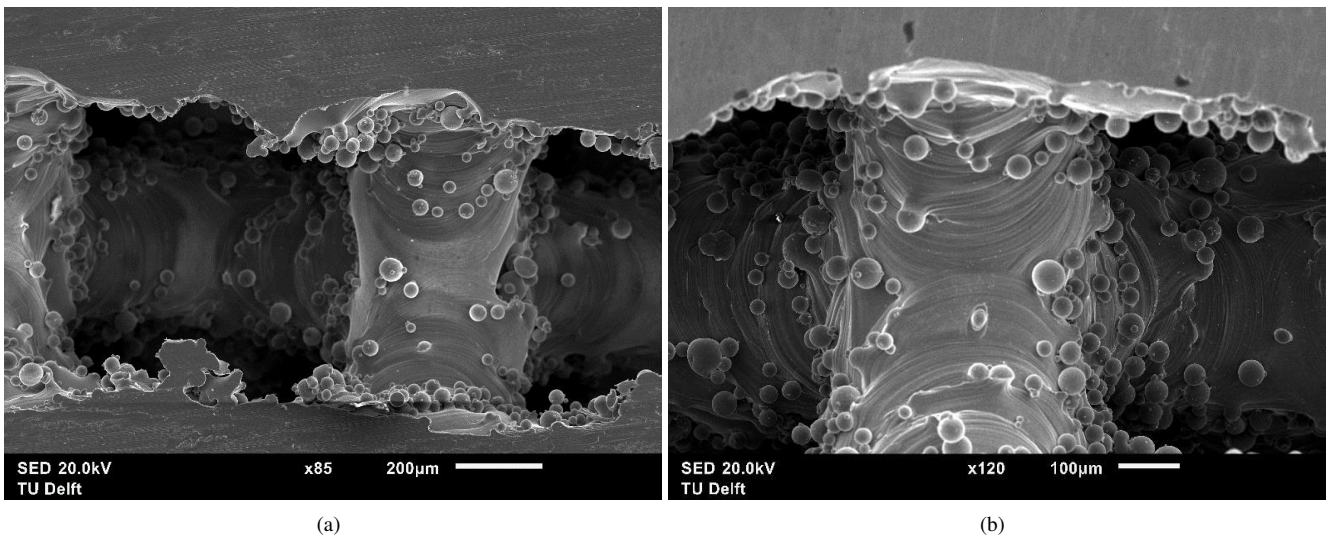
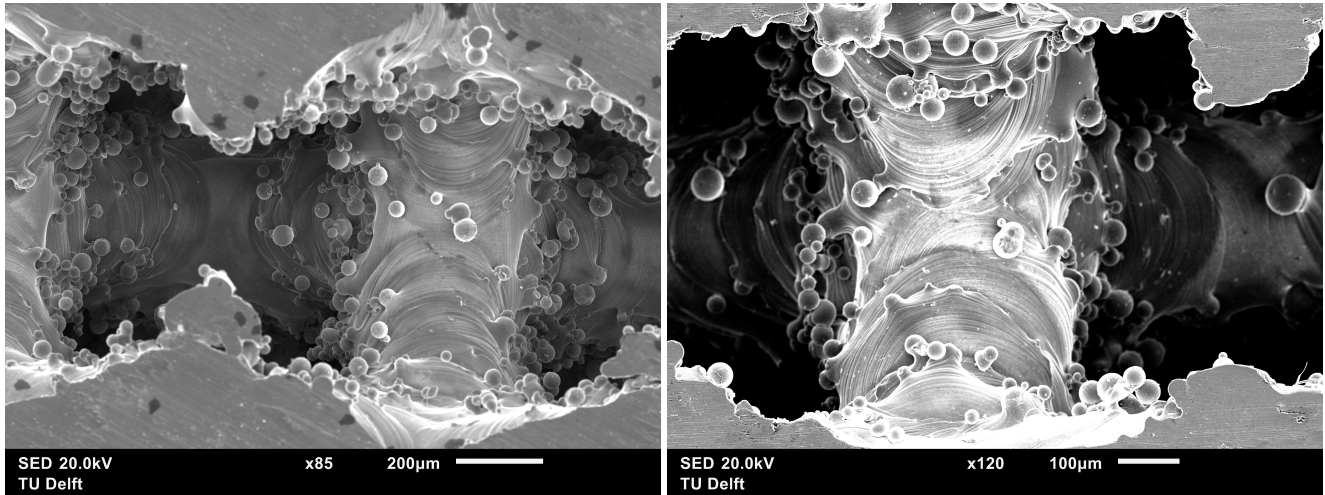
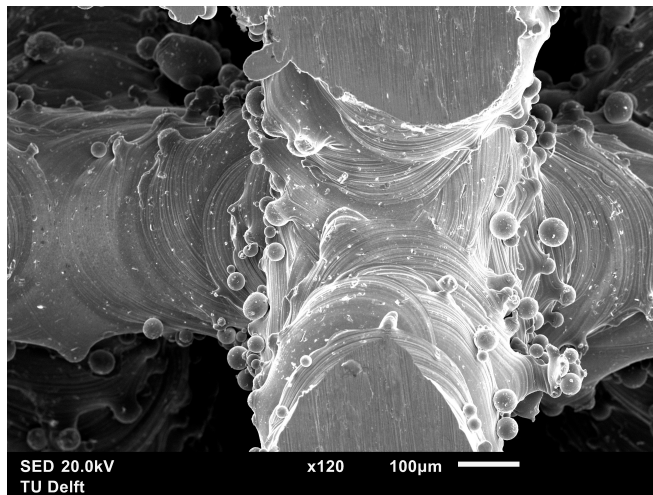


Figure 74. Figures regarding (a) the core of continuous AP+SB sample (3 bars 90s 180 microns powder) (b) and the core of continuous AP+SB 4.5 bars 90s 12 microns



(a)

(b)



(c)

Figure 75. Figures regarding (a) Continuous AP (b) Continuous AP + SB 3 bars 90s 50 microns (c) Continuous AP + SB 4.5 bars 90s 50 microns

B EDS results of SB after CE

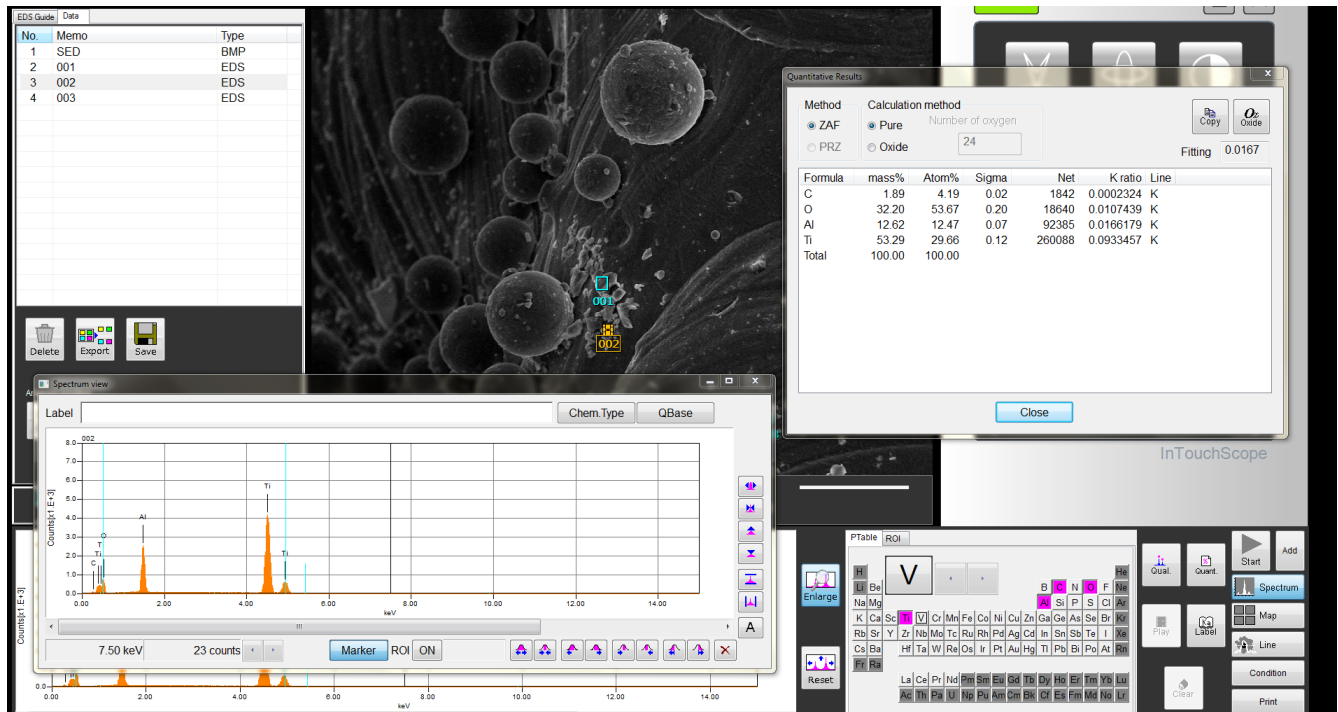


Figure 76. EDS results obtained for continuous HIP SB samples at the core of the cylinder

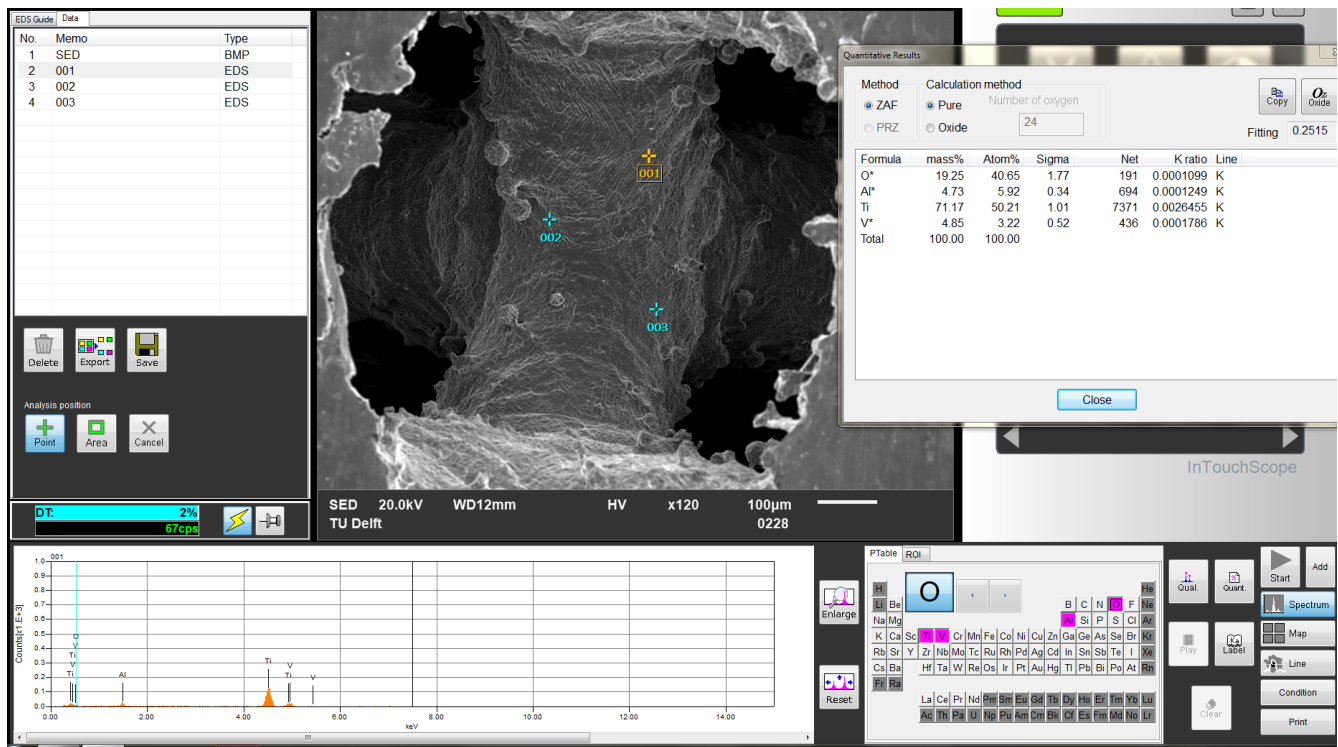


Figure 77. EDS results obtained for continuous HIP SB+CE samples at the core of the cylinder

C Statistics of Sessile drop results

Table 14. ANOVA statics table Sessile drop results

Source	SS	df	MS	F	Prob>F
Columns	4002,78	5	800.556	27.65	2.8129×10^{-12}
error	1216.19	42	28.957		
total	5218.97	47			

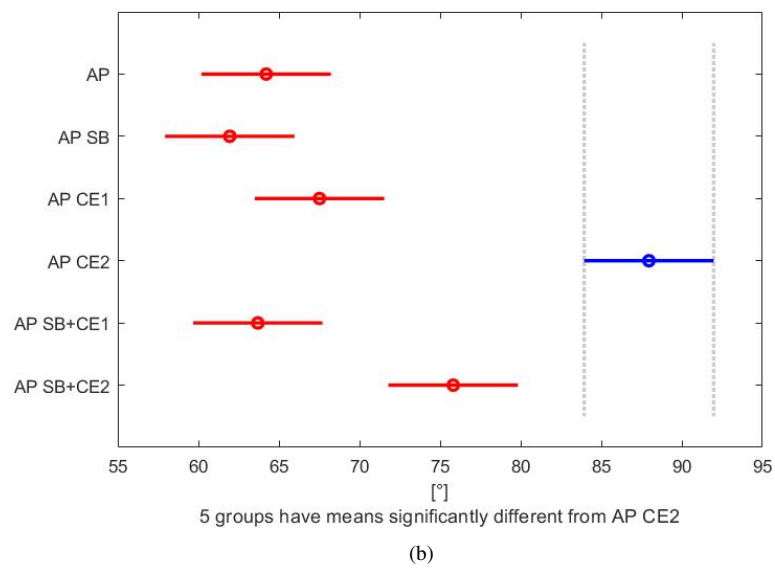
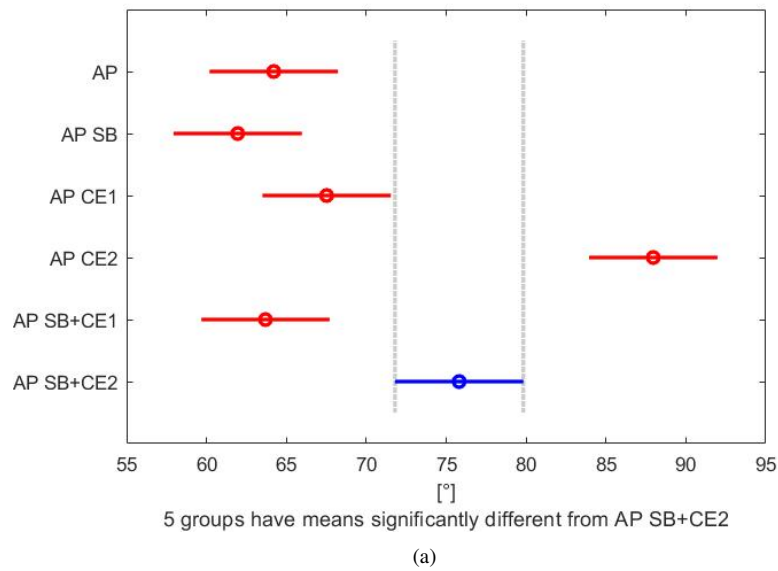


Figure 78. Figures regarding Tukey's test (a) for AP SB CE2 (b) and for AP CE2